Master thesis in Aerospace Engineering

Politecnico di Torino

Aerodynamic Characterization of Deployable Recovery Concepts for Orbital Rocket Stages

Supervisor

Prof. Domenic D'AMBROSIO

Prof. S. FASOULAS

MSc. S. FÖRSTE

Candidate

Filippo Renato ROLETTO

20th March 2026

Proof of Authorship

I hereby declare that this thesis is my own work and effort and follows the regulations related to good scientific practice of the University of Stuttgart in its latest form. All sources cited or quoted are indicated and acknowledged by means of a comprehensive list of references. I acknowledge the use of Claude to rephrase self-written texts.

Stuttgart, 20.03.2026

Filippo Renato Roletto

Abstract

The growing accumulation of orbital debris in Low Earth Orbit poses an increasing threat to the long-term sustainability of space operations. In response to tightening international regulations and environmental concerns associated with uncontrolled atmospheric re-entry, the Design not to Demise (Dn2D) philosophy has emerged as a viable alternative to traditional destructive disposal strategies. This thesis presents an aerodynamic characterization of deployable recovery concepts for orbital rocket stages, with focus on the Upper Liquid Propulsion Module (ULPM) of the Ariane 6 launch vehicle. The study investigates the aerodynamic behavior of a Deployable Aerodynamic Stabilizer (DAS), a panel passive stabilization system, across the transional and near-continuum flow regimes encountered during atmospheric re-entry. Numerical simulations are performed using the PICLas framework, employing both the Direct Simulation Monte Carlo (DSMC) and the Bhatnagar–Gross–Krook (BGK) methods to resolve the flow field. A parametric analysis was conducted over multiple DAS opening angles (30° to 70°), center-of-gravity positions, fin lengths, and angles of attack. Aerodynamic coefficients, including drag, lift, and pitching moment, were extracted and used to assess static stability across configurations. Additionally, the feasibility of forced spin stabilization as a complementary technique was evaluated. The findings contribute to the definition of geometric design requirements for passively stable re-entry of large cylindrical rocket stages, supporting the development of cost-effective and environmentally responsible orbital recovery systems.

Acknowledgements

Table of Contents

List of Tables

List of Figures

Glossary

AoA

Angle of Attack

BGK

Bhatnagar–Gross–Krook

CAD

Computational Aided Design

CFD

Computational Fluid Dynamics

CoG

Center of Gravity

CoP

Center of Pressure

D4D

Design for Demise

DAS

Deployable Aerodynamic Stabilizer

Dn2D

Design not to Demise

DOF

Degree of Freedom

DSMC

Direct Simulation Monte Carlo

EDL

Entry, Descent and Landing

EOL

End of Life

ESA

European Space Agency

ESBGK

Ellipsoidal Statistical Bhatnagar–Gross–Krook

FPA

Flight Path Angle

GEO

Geostationary Earth Orbit

IRS

Institute of Space Systems

Kn

Knudsen Number

LEO

Low Earth Orbit

MCS

Mean COllision Separation

MFP

Mean Free Path

NASA

National Aeronautics and Space Administration

RCS

Reaction control system

RPM

Revolutions Per Minute

STRAT

System Engineering Trajectory and Aerothermal Analysis Tool

TMAC

Tangential momentum accommodation coefficient

TPS

Thermal Protection System

ULPM

Upper Liquid Propulsion Module

Chapter 1

Introduction

In recent years, orbital expansion has entered a new phase in which sustainability and vehicle reusability have gained increasing attention within the space sector. According to the European Space Agency (ESA)'s Space Environment Report 2025, approximately 40,000 tracked objects larger than 10 cm are currently in Earth orbit [1], of which just about 11,000 are active payloads [2]. Launch cadence and mass deployments have accelerated in recent years, and constellation and small-satellite programmes continue to drive a sharp increase in the number of objects placed in LEO. Current environment models estimate on the order of 1.2×10^6 objects with diameters greater than or equal to 1 cm and tens of thousands of objects with diameters greater than or equal to 10 cm, underscoring that tracked objects represent only a fraction of the hazardous population. Since 2019, the expected casualty risk from re-entry has trended upward and tracked objects with masses exceeding 500 kg are observed to re-enter the atmosphere on a near-weekly basis [3]. Therefore, while early spaceflight was primarily driven by the ambition to explore new frontiers, contemporary engineering must now confront the physical legacy of that ambition: a crowded orbital landscape [4], particularly in Low Earth Orbit (LEO), which increases collision probabilities and elevates the risk of cascading debris events that threaten the continuation of future missions. Historical debris-generating collisions have already demonstrated the severity of this effect, and ESA projections indicate that non-compliance with mitigation measures could double the number of objects larger than 10 cm within a few decades [5]. Such a development could render entire orbital regions unusable, jeopardizing future missions and, in the most severe scenario, deny access to space for centuries. In response to these concerns, the concept of Design for Demise (D4D) has been explored as one possible approach to re-entry risk mitigation, aiming to maximize the destruction of a vehicle during uncontrolled atmospheric re-entry in order to reduce the probability of ground casualties below the threshold of 10^{-4} imposed by international standards [6]. However, D4D remains a field of active and ongoing

research rather than a universally adopted practice: its implementation is driven by individual operators and is not globally enforced, with some actors not consistently performing active de-orbit or designing for demise on large objects. Moreover, the approach presents growing limitations in practice. On the one hand, it is estimated that between 5% and 40% of the mass of large structures, such as upper rocket stages, may nevertheless survive thermal loads and reach the surface with hazardous kinetic energy. On the other hand, the massive vaporization of aluminium alloys and carbon-fibre-reinforced polymers (CFRP) injects into the stratosphere tonnes of nanoparticulate aluminium oxide (Al2O3), soot, and nitrogen oxides (NO_x) [7, 8, 9]. These species can alter the Earth's radiative balance and catalyze chemical reactions that deplete the ozone layer, potentially undermining the gains achieved under the Montreal Protocol.

These limitations have stimulated interest in an alternative approach: Design not to Demise (Dn2D). While this remains an emerging and sporadically explored area of research rather than an established field, the underlying principle represents a significant conceptual shift. Rather than engineering a vehicle for destruction during re-entry, Dn2D aims to enable structural survivability, with the primary goal of eliminating the mass vaporization responsible for injecting harmful species such as aluminium oxide, soot, and nitrogen oxides into the stratosphere. As a secondary benefit, a structurally intact vehicle may also open the possibility of recovering and partially reusing critical subsystems such as propulsion units and avionics. Characterizing the aerothermodynamic environment of a re-entering vehicle is a fundamental challenge regardless of the disposal strategy adopted, as the accurate prediction of thermal and mechanical loads is challenging across the full range of encountered flow regimes. In the Dn2D context, an additional requirement emerges: ensuring that the vehicle maintains a controlled and stable attitude throughout re-entry, so that active attitude control systems can be avoided. The identification of approaches that enable this is the subject of current research. A novel concept currently being investigated at the IRS is the passive aerodynamic stabilization of an upper stage using integratable deployable elements. Within this context, the present thesis focuses on the aerodynamic characterization of a simplified CAD model of the Upper Liquid Propulsion Module (ULPM) of Ariane 6, an elongated cylindrical configuration for which previous studies have identified intrinsic stability issues. The objective of the research is to develop a stability map that defines the geometric requirements necessary to ensure a passively stable attitude during atmospheric re-entry, thereby helping to ensure that access to space remains safe and consistent with the global environmental-protection objectives established by international treaties.

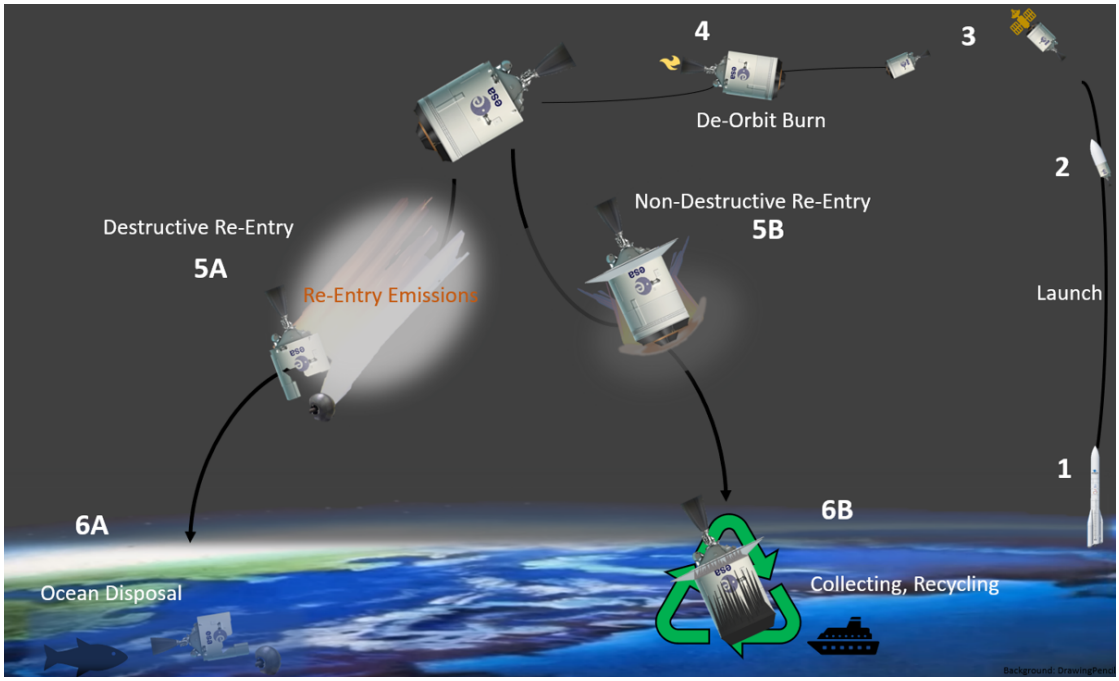

Figure 1.1: Visual comparison of ULPM re-entry trajectory for D4D (left side, ending in "Ocean Disposal") and Dnot2D approaches (on the right, ending with "Collecting, Recycling")[10]

This work is structured as follows. Chapter 2 reviews the state of the art on aerodynamic approaches for atmospheric re-entry and recovery, comparing D4D and Dn2D strategies and defining the project's specific objectives. Chapter 3 presents the theoretical foundations of aerothermodynamics, covering shock-layer physics, flow regimes from continuum to transitional and free molecular, and the principles of static and dynamic stability, including the forced-spin stabilization technique. Chapter 4 describes the numerical methodology and the simulation workflow, detailing the PICLas framework, the employed DSMC and BGK solvers, the CAD-based configuration of the ULPM upper stage, and the Matlab toolchain developed for data post-processing and analysis. Chapter 5 presents the simulation setup and the parametric configurations investigated. Chapter 6 reports and discusses the numerical results, comparing geometries and atmospheric entry conditions to identify optimal configurations. Finally, Chapter 7 summarizes the conclusions and outlines prospective developments for orbital-stage recovery and controlled re-entry.

Chapter 2

State of the Art of atmospheric re-entry

Atmospheric re-entry constitutes the transition of a space vehicle from orbital motion to atmospheric flight, spanning a wide range of flow regimes from hypersonic to supersonic and, eventually, subsonic conditions [11]. During this process, the vehicle must dissipate the large amount of kinetic energy accumulated in orbit through interactions with the Earth's atmosphere. For objects returning from Low Earth Orbit (LEO), entry velocities are typically on the order of 7.5-8.0 km/s, resulting in extreme aerodynamic heating and mechanical loads during the early, high-enthalpy phase of re-entry [11]. These conditions impose stringent requirements on vehicle design, particularly with respect to structural integrity, thermal protection, and static and dynamic stability. The success of an Entry, Descent, and Landing (EDL) sequence is therefore closely linked to the aerodynamic configuration of the re-entry system [11]. Aerodynamic design influences not only the magnitude and distribution of thermal and mechanical loads, but also the ability of the vehicle to maintain a favorable attitude with respect to the incoming flow. Aerodynamic features primarily act as enabling elements. While they do not eliminate the need for robust thermal protection systems, they can significantly shape the flow field, influence peak heating rates, and control the vehicle's orientation throughout descent. Beyond vehicle-level considerations, atmospheric re-entry plays a central role in end-of-life (EOL) management strategies for space systems. Orbital debris mitigation efforts are primarily aimed at reducing collision risks and ensuring the long-term sustainability of space operations [12]. However, the re-entry phase introduces an additional and distinct safety dimension: surviving structural components of large objects, such as upper rocket stages, may carry sufficient kinetic energy to pose a hazard to infrastructure, people, and the environment [7]. The aerodynamic behavior of a vehicle during re-entry, including its deceleration profile and breakup or

survivability characteristics, hence becomes a key factor in assessing and mitigating both orbital and terrestrial risk.

2.1 Parameters and Energy Management

An uncontrolled destructive re-entry typically follows natural orbital decay, during which objects are subjected to severe aerothermal and mechanical loads that may lead to structural break-up and destruction [7, 11]. However, complete demise is not always guaranteed: surviving debris can reach the Earth's surface with significant impact energy, and uncertainties in trajectory modelling and dispersion of surviving components complicate the prediction of impact footprints [7]. A key parameter in this context is the ballistic coefficient β, defined as:

$$\beta = \frac{m}{C_D S_{\text{ref}}}, \tag{2.1}$$

where m is the mass, C_D the drag coefficient, and S_{ref} the aerodynamic reference area. This parameter governs the altitude at which significant deceleration begins and therefore influences the heating environment experienced by the vehicle. Lower values of β shift energy dissipation toward higher, less dense atmospheric layers, which tends to reduce peak convective heating near the stagnation point. This benefit, however, comes with a trade-off: reducing β extends the descent duration and may increase the total integrated heat flux absorbed by the structure. This compromise must therefore be carefully evaluated during the design phase [11]. Beyond the ballistic coefficient, the lift-to-drag ratio L/D governs the vehicle's capacity for cross-range maneuvers and its control authority over the re-entry corridor. Values of L/D close to zero define quasi-ballistic re-entry regimes, whereas positive values of this ratio allow more flexible modulation of the descent profile, enabling attenuation of peak deceleration loads and improving landing precision [11]. Thermal loads at the stagnation point are strongly influenced by the nose radius R. In the hypersonic regime, the maximum convective heat flux at the stagnation point scales approximately as:

$$\dot{q}_{\text{stag}} \sim \frac{1}{\sqrt{R}}. \tag{2.2}$$

Blunter geometries generate detached bow shocks with thicker shock layers, reducing the fraction of convective energy transferred to the surface and mitigating local heating peaks [11]. Finally, structural integrity throughout the descent is primarily dictated by the maximum dynamic pressure:

$$q_{\infty,\max} = \tfrac{1}{2}\,\rho\, v^2, \tag{2.3}$$

which represents the peak aerodynamic load encountered during re-entry and defines key structural requirements for both the vehicle and its thermal protection system (TPS). Exceeding this limit may induce elastic instabilities such as buckling or structural failure of load-bearing components. Accurate prediction of $q_{\infty,\max}$ is hence essential to ensure vehicle survivability throughout the re-entry phase [11].

2.2 Disposal Strategies

To mitigate the risks associated with uncontrolled re-entries, the aerospace sector is evaluating approaches with markedly different levels of maturity. Design for Demise (D4D) remains the primary framework adopted by most operators for reducing ground casualty risk, while nascent concepts collectively referred to as Design not to Demise (Dn2D) are beginning to emerge, focused on structural survival to reduce environmental impact and enable recovery[13].

2.2.1 Design for Demise (D4D)

The Design for Demise approach originates from the need to mitigate the risk of human casualties resulting from uncontrolled re-entries. International standards established by NASA and ESA impose a maximum acceptable casualty probability of 1 in 10 000 per re-entry event. The primary goal of D4D is to ensure that the spacecraft fragments and fully vaporizes during atmospheric re-entry, hence minimising the number, mass, and size of surviving fragments that reach the ground [14]. Techniques implemented within the D4D paradigm operate at multiple levels of system design. A common strategy is the substitution of critical materials. Components traditionally manufactured from titanium or stainless steel, such as propellant tanks or reaction-wheel balance masses, are re-engineered using aluminium alloys or other low melting-point materials. Architectural modifications are also adopted, including the use of break-out patches on external panels and demisable joints, designed to promote early intrusion of hypersonic flow into the fuselage and accelerate the destruction of internal subsystems. However, recent experiments have demonstrated that certain items, particularly large titanium tanks, remain extremely challenging to fully demise even under complete aerothermal exposure, highlighting the limitations of this approach [15].

A related but distinct strategy is Design for Containment (D4C), which can be regarded as a limiting case within the D4D philosophy. Rather than maximising demise, D4C aims to reduce the number of impacting fragments by keeping critical components structurally contained during re-entry, so that they land as a single fragment, potentially more energetic, hence reducing the probability of collision with an individual compared to a scenario involving multiple dispersed fragments

[16]. In doing so, D4C locally enforces structural integrity during re-entry, a characteristic that shares a partial conceptual parallel with the Dn2D paradigm discussed below.

Beyond the ground casualty risk, destructive re-entries generate atmospheric emissions whose significance is the subject of ongoing research. During ablation, aluminium alloys react with atomic oxygen to form aluminium oxide (Al_2O_3) nanoparticles, which can remain suspended in the stratosphere for years and act as catalysts for heterogeneous chemical reactions that deplete stratospheric ozone [17]. The aluminium oxide compounds generated by the entire population of satellites reentering in 2022 are estimated at approximately 17 metric tons, corresponding to a 29.5% increase over the background level produced by natural meteor ablation, a threshold that could be rivalled by the anthropogenic flux from megaconstellation growth by 2040 [17, 18]. The full magnitude and long-term consequences of these effects, however, remain uncertain and are an active area of investigation [17, 18]. The Design not to Demise approach is proposed to address these problems by avoiding fragmentation and enabling intact vehicle re-entry, thereby aiming to prevent the release of ablation products into the upper atmosphere.

2.2.2 Design not to Demise (Dn2D)

Design not to Demise is not yet an established design philosophy but it rather represents an emerging research direction focused on structural survivability during atmospheric re-entry, with the primary goal of limiting material ablation and the associated injection of harmful species into the upper atmosphere. As secondary benefits, a surviving vehicle may open the possibility of partial recovery, recycling of materials, or controlled surface disposal [19, 13]. The present work investigates the applicability of deployable aerodynamic elements as an enabling technology for a Design not to Demise approach, targeting two primary functions: reducing aerothermal loads to levels compatible with structural integrity, and establishing an aerodynamically stable geometry capable of passively maintaining a controlled attitude throughout the re-entry trajectory, thereby confining peak heating to thermally protected surfaces. In the context of upper stage re-entry, controlled deorbit is already performed routinely by several operators as a baseline EOL strategy. SpaceX performs controlled deorbit burns of the Falcon 9 second stage following payload deployment, targeting uninhabited ocean regions [20]. Similarly, the Ariane 6 upper stage is designed with a restartable Vinci engine specifically to enable a controlled deorbit burn at the end of its mission, ensuring compliance with debris mitigation requirements [21].

Among the technologies investigated as potential enablers for controlled re-entry and structural survivability, deployable aerodynamic decelerators have received considerable attention in the recent literature. By remaining stowed during ascent and deploying prior to re-entry, these systems circumvent the fairing diameter constraint that limits the size of conventional rigid heat shields, and offer the potential to significantly reduce the ballistic coefficient of large stages without requiring major structural redesign. It is noted that the present work focuses exclusively on rigid deployable elements; the following overview is therefore intended as a broader contextualisation of the deployable re-entry technology landscape, rather than a direct description of the approach adopted here.
The HIAD (Hypersonic Inflatable Aerodynamic Decelerator) technology, developed by NASA and successfully demonstrated during the LOFTID mission in 2022, employs an inflatable structure of concentric pressurised tori covered by a multilayer Flexible Thermal Protection System (FTPS). Following the LOFTID demonstration, ULA has identified the technology as a candidate for recovering the engine bay of the Vulcan Centaur first stage, leveraging the drag area achievable with inflatable systems to enable controlled descent and hardware reuse [22]. In the European context, the EFESTO project (H2020, 2019–2022) and its follow-on EFESTO-2 (Horizon Europe) have pursued the development of inflatable heat shield technology at progressively higher TRL, targeting both Earth re-entry and Mars exploration applications, with a reference mission concept based on the recovery of the Vega AVUM upper stage [23].

Rigid deployable systems offer an alternative to inflatable concepts by achieving large aerodynamic surfaces without the complexity associated with pressurised structures. It is noted that a subset of rigid deployable concepts, such as the umbrella-like ADEPT configuration, still employs flexible thermal protection materials stretched over a mechanical framework, and therefore shares certain TPS characteristics with inflatable systems. The ADEPT (Adaptable Deployable Entry and Placement Technology), developed by NASA, deploys using a framework of carbon ribs that tension a 3D-woven carbon fabric, relying on mechanical actuators rather than pressurised gas [24]. However, for large-scale applications such as upper stages, the mass of the mechanical joints and rib structure can represent a significant penalty compared to inflatable concepts.
Among rigid deployable concepts, panel-based configurations currently represent the highest-TRL class, with heritage traceable to control surfaces such as the Space Shuttle body flap. In these systems, flat or curved rigid panels are hinged to the aft body of the stage and deployed outward prior to re-entry, acting simultaneously as aerodynamic decelerators and passive stabilizers. The function and aerodynamic behaviour of such a Deployable Aerodynamic Stabilizer (DAS) in the context of upper stage re-entry is described in detail in Section **??** [25].

Deployable concepts are particularly attractive for large expendable stages because they can be stowed during ascent and deployed prior to re-entry, requiring no fundamental redesign of the existing vehicle architecture. This integrability is the central motivation for the DAS concept investigated in the present thesis, which is introduced in the following section.

2.2.3 Reference Configuration

The present study is based on a simplified CAD model derived from the geometry of the Upper Liquid Propulsion Module (ULPM) of the Ariane 6 launcher. The model retains the key geometric features of the actual stage, the blunted conical nose, the main cylindrical body, and the aft-mounted deployable stabilizer, while abstracting away structural details not relevant to the aerodynamic analysis. The actual ULPM is shown in Figure **??** for reference. The cryogenic upper stage comprises the following main structural elements: the two propellant tanks for liquid hydrogen (LH2) and liquid oxygen (LOX), the inter-tank structure (ITS), the VINCI engine, the VINCI thrust frame (ViTF), and the avionic support structure (AvSS). The two tanks are connected through the ITS, and the VINCI engine introduces the structural loads into the stage via the ViTF. The thrust frame features a cone-shaped architecture and integrates the on-board electronics, fluidics, the auxiliary power unit (APU), and pressurised gas tanks containing helium. The avionic system, which encompasses the navigation system and on-board computers, is housed within the AvSS between the two propellant tanks. On top of the ULPM, the launch vehicle adapter (LVA) provides the mechanical and electrical interface with the payload, and is further connected to the fairing and the dual launch structure (DLS). The module has a dry mass of approximately $m_{\text{dry}} \approx 6\,\text{t}$, a maximum diameter of approximately 5.4 m, and a total height of approximately 12 m, of which 5.9 m are occupied by the propulsion section.

Given the preliminary nature of the study, a methodology based on approximate analysis and simplified geometry has been adopted. This approach enables the derivation of initial estimates of aerodynamic coefficients and stability characteristics already during the conceptual design phase. The simplified CAD model developed for this purpose is presented in Figure 2.2.

The geometry is subdivided into three distinct aerodynamic sections, as illustrated in Figure 2.2: the nose, the cylindrical body, and the Deployable Aerodynamic Stabilizer (DAS).

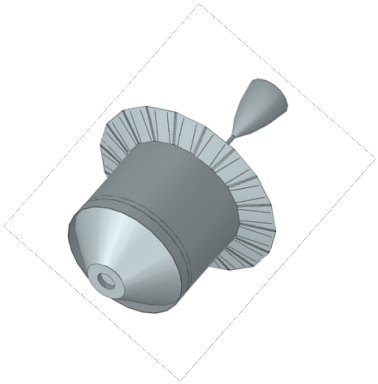

Figure 2.1: 3D model

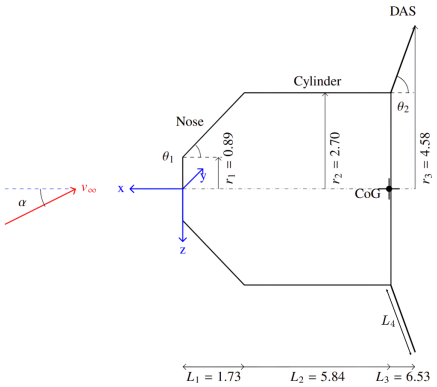

Figure 2.2: 2D projection of CAD model [26]

The DAS is characterised by a conical geometry with half-angle θ_2 and base radius $r_3 = 4.58\,\text{m}$, deployed over a length $L_3 = 6.53\,\text{m}$, and represents the primary aerodynamic stabilizer of the system. The reference frame is centred at the nose tip, with the x-axis aligned with the longitudinal axis pointing rearward and the z-axis directed downward. The center of gravity (CoG) is located along the longitudinal axis within the cylindrical section; its axial position is varied parametrically in the stability analysis presented in Chapter 6. The freestream velocity V_∞ approaches the vehicle at an angle of attack α with respect to the longitudinal axis.

2.3 Thesis Objective

The present thesis investigates the aerodynamic stability of a simplified CAD model of the Ariane 6 ULPM equipped with a passive Deployable Aerodynamic Stabilizer (DAS) during atmospheric re-entry. The primary objective is to construct a stability map across the transitional and near-continuum flow regimes by systematically varying the DAS opening angle, panel length, angle of attack, and center-of-gravity position, identifying which geometric configurations ensure passively stable flight throughout the descent trajectory. High-fidelity numerical simulations using the PICLas framework with DSMC and BGK solvers are employed to resolve the flow field across all relevant regimes. The results are intended to lay a foundation for future design decisions on passive aerodynamic re-entry solutions for large expendable stages.

Chapter 3

Theoretical foundations

This chapter presents the fundamental principles underlying the aerodynamic and aerothermal behaviour experienced by a vehicle during atmospheric re-entry, followed by a review of the equations governing flight motion and an introduction to forced rotation as a spin-based attitude stabilization technique.

3.1 Atmospherical Model

The atmosphere, through its intrinsic physical properties, defines the undisturbed flow field experienced by re-entry vehicle. These flow conditions govern both the aerodynamic forces and moments acting on the vehicle, as well as the complex aerothermal phenomena arising during high-speed flight. Consequently, a rigorous and precise characterization of atmospheric data is indispensable for the design, guidance, and control of vehicles in atmospheric re-entry. In the present study, air is adopted as the reference working gas. Nevertheless, atmospheric entry in extraterrestrial environments, which likewise occurs at hypersonic velocities, involves atmospheres composed of chemically and thermodynamically distinct gas mixtures, often exhibiting highly non-ideal or exotic behavior. In certain instances, such as the landing of the Huygens probe on Titan, the precise composition and thermophysical properties of the atmosphere remain incompletely characterized, introducing considerable uncertainties into the aerodynamic and thermal design of vehicles intended for atmospheric entry of the planet[27]. For terrestrial entries, air is commonly modelled as a binary mixture of molecular nitrogen and oxygen (neglecting argon for most aerothermodynamic considerations), with molar fractions approximately $X_{\mathrm{N}_2} \simeq 0.79$ and $X_{\mathrm{O}_2} \simeq 0.21$. This corresponds to a dry-air mean molar mass of about $M_{\mathrm{air}} \approx 28.85$ g mol^{-1} when argon is omitted (standard dry-air value including argon is ≈ 28.97 g mol^{-1})[28].

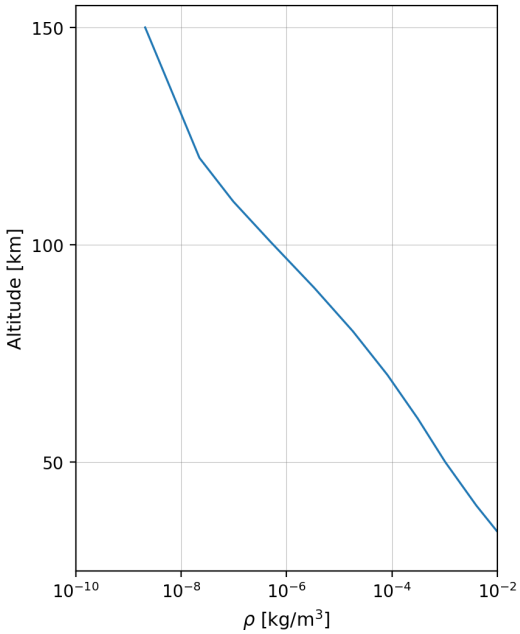

Figure 3.1: (a) Density at different altitudes

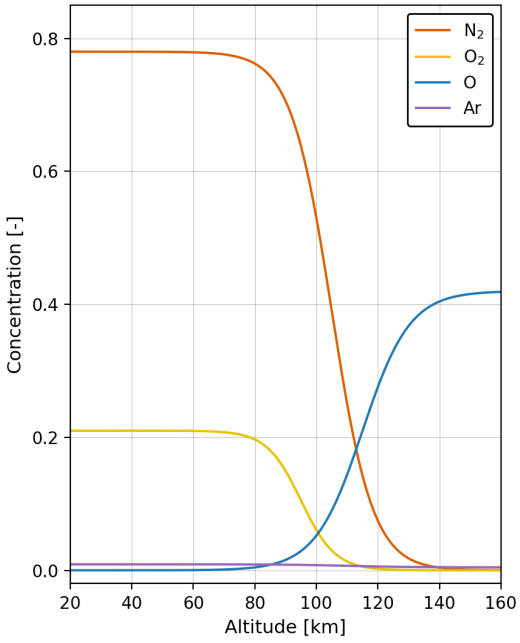

Figure 3.2: (b) Concentration at different altitudes

However, under the extreme thermodynamic conditions typical of hypersonic reentry, air can no longer be treated as an inert gas with constant properties. The large amount of kinetic energy converted into heat triggers vibrational excitation, molecular dissociation and, at higher velocities, ionization of the atmospheric constituents. These transformations radically alter the thermophysical and transport properties of the flow, making it necessary to adopt advanced gas-dynamic (thermochemical) models capable of capturing chemical equilibrium and non-equilibrium effects.

3.2 Fundamental aspect of Asmospheric Re-entry

The transition between different flight regimes is not merely a monotonic increase of speed but a progressive change in the dominant physical processes that govern the interaction between a solid body and the surrounding fluid. The key parameter used to define the transition regarding the velocity regime is the Mach number (M), a dimensionless quantity expressing the ratio between the macroscopic velocity of the object (v) and the local speed of sound (a) in the medium.[28] The fundamental relation $M = v/a$ reveals that the speed of sound acts as an information limit within the fluid: it represents the velocity at which small pressure disturbances

propagate through the air. Since the speed of sound depends strongly on the absolute temperature of the gas (T), according to the thermodynamic relation $a = \sqrt{\gamma RT}$ (where γ is the ratio of specific heats and R is the specific gas constant), the aerodynamic behavior of a vehicle at a given velocity can vary dramatically with altitude and atmospheric conditions.[29]

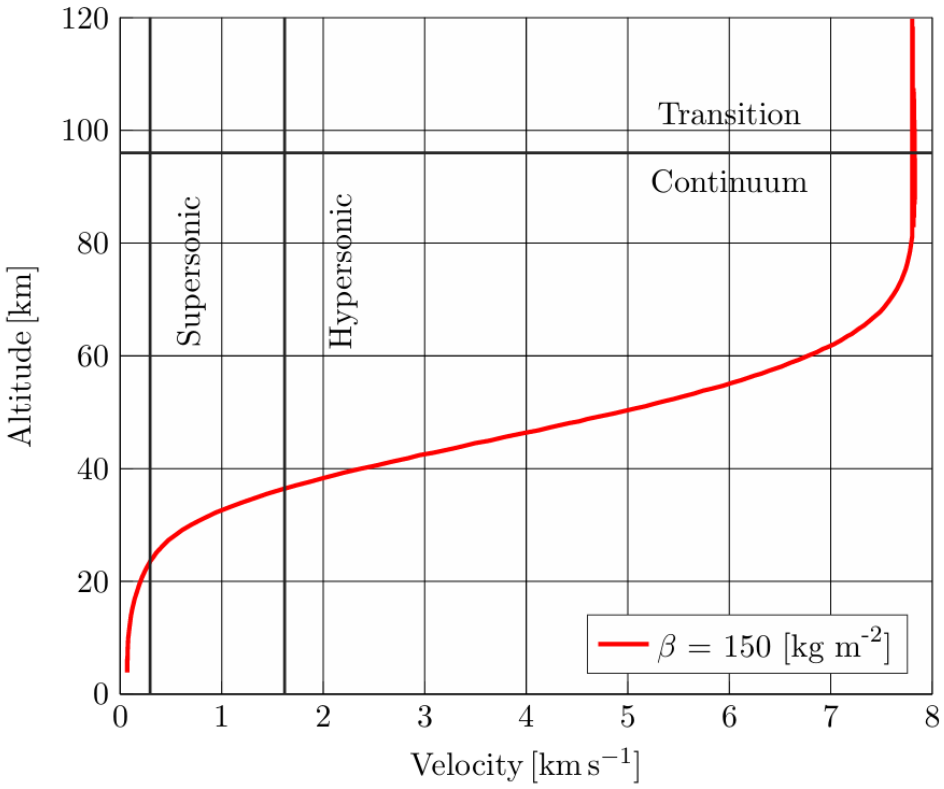

Figure 3.3: Altitude plotted over the velocity of an exemplary ballistic re-entry trajectory from 120km with indications of flow and flight regime changes

The subsonic regime is defined by flows in which the Mach number everywhere is below unity ($M < 1$). For engineering purposes, however, this regime is often subdivided into two subcategories based on the fluid's compressibility. When $M < 0.3$–0.4, air can be treated as incompressible. In this range, pressure variations induced by the vehicle's motion produce negligible changes in air density, permitting the use of Bernoulli's equation and simplified aerodynamic models. In this regime the pressure waves generated by the moving body propagate faster than the body itself; consequently, the fluid upstream of the vehicle is informed of the approaching object and begins to deviate its trajectory prior to physical contact, establishing a smooth, continuous flow field. As the speed increases beyond approximately Mach

0.4, compressibility effects become significant: air can no longer be assumed to have constant density, and dynamic pressure begins to compress the gas. Under these conditions, more advanced thermodynamic and compressible-flow models must be incorporated to accurately predict aerodynamic forces such as drag and lift[30]. The transonic regime, which extends approximately between Mach 0.75 and 1.20. The onset of this regime is defined by the critical Mach number (M_{crit}), which is the free-stream Mach number at which the local flow velocity first reaches Mach 1.0 at a specific point on the surface, typically where the curvature is greatest.[31] Supersonic flight occurs when the vehicle's speed is entirely greater than the speed of sound ($M > 1.2$ up to approximately $M \approx 5$). In this regime the vehicle travels faster than the pressure waves it generates, producing a continuous wavefront that takes the form of a cone known as the Mach cone. The cone's half-angle μ (the Mach angle) satisfies $\sin \mu = 1/M$ and becomes progressively sharper as the Mach number increases, a factor that directly impacts vehicle aerodynamic and structural design. The hypersonic regime is entered when velocities exceed approximately Mach 5. This threshold is not dictated by a single abrupt physical change, but rather marks the point at which multiple thermodynamic and chemical effects become dominant and can no longer be neglected. At these speeds, the kinetic energy of the flow is converted into thermal energy across the shock wave at a rate sufficient to excite internal molecular degrees of freedom and drive chemical reactions. The calorically perfect gas assumption, already an approximation in supersonic flight, breaks down entirely under these conditions [32]. Several coupled microscopic processes become significant: vibrational excitation, whereby O_2 and N_2 molecules store energy in internal vibrational modes in addition to translational and rotational modes; molecular dissociation, in which oxygen begins to dissociate at temperatures on the order of $\sim 2000\,\text{K}$, followed by nitrogen at temperatures exceeding $\sim 4000\,\text{K}$; and ionization, whereby at orbital velocities of approximately Mach 25 the gas forms a plasma sheath around the vehicle that attenuates or completely blocks radio-frequency signal propagation, resulting in a communication blackout [33].

While a Mach-number–based classification describes the macroscopic speed of the flow, there is an equally crucial physical dimension: the molecular structure of the fluid. The Navier-Stokes equations, which govern classical fluid mechanics, are based on the continuum hypothesis, in which macroscopic field variables, such as velocity, density, temperature are assumed to be well defined on length scales that are small compared with the characteristic dimensions of the system, yet large compared with intermolecular distances[34]. The dimensionless parameter that quantifies the deviation from the continuum hypothesis is the Knudsen number (Kn), defined as the ratio between the molecular mean free path (λ) and a characteristic length

scale of the system (L):

$$Kn = \frac{\lambda}{L}. \tag{3.1}$$

The mean free path λ represents the average distance travelled by a gas molecule between successive collisions. Using kinetic theory for a hard-sphere gas, λ can be expressed as:

$$\lambda = \frac{k_B\, T}{\sqrt{2}\,\pi\,\sigma^2\, P}, \tag{3.2}$$

where $k_B = 1.380649{\times}10^{-23}\ \mathrm{J\,K^{-1}}$ is the Boltzmann constant, T the thermodynamic temperature, $\sigma \approx 3.7 \times 10^{-10}$ m the effective molecular diameter for air, and P the static pressure. The widespread adoption of the Knudsen-number–based classification of flow regimes traces back to Tsien's 1946 work on Superaerodynamics. This subdivision distinguishes four principal regimes, each characterized by different governing physical mechanisms and corresponding mathematical models.

Flow regimes	**Kn range**
Continuum (No-slip)	$Kn < 0.01$
Continuum (slip)	$0.01 < Kn < 0.1$
Transition	$0.1 < Kn < 10$
Free molecular	$Kn > 10$

Table 3.1: Categorization of the flow regimes by Knudsen number [35]

In the continuum regime ($Kn < 0.01$), the Navier–Stokes equations accurately describe the flow field. The fundamental boundary condition is the no-slip condition, whereby the fluid velocity at the wall is equal to the velocity of the wall itself. This assumption implies that molecular momentum exchange with the surface is sufficiently efficient to eliminate any macroscopic relative velocity at the interface[29]. When $0.01 < Kn < 0.1$, the continuum hypothesis begins to break down within a thin near-wall region known as the Knudsen layer. In this region, molecules undergo an insufficient number of intermolecular collisions to establish perfect local thermodynamic equilibrium before interacting with the surface. As a result, a finite macroscopic velocity relative to the wall (velocity slip) and a discontinuity in temperature (temperature jump) are observed.

To model this regime, the Navier–Stokes equations are still applied in the bulk flow, while first- or second-order Maxwell boundary conditions are imposed at the wall. The velocity slip (u_{slip}) is given by:

$$u_{slip} = \left(\frac{2-\sigma_v}{\sigma_v}\right)\lambda\left(\frac{\partial u}{\partial n}\right)_w \tag{3.3}$$

where σ_v is the tangential momentum accommodation coefficient (TMAC), representing the fraction of molecules that are diffusely reflected by the surface. In the transitional regime ($0.1 < Kn < 10$), the Navier–Stokes equations lose their validity, as the constitutive relations linking stresses and heat fluxes to velocity and temperature gradients (Newton's and Fourier's laws) are no longer linear. An accurate description of the system requires the Boltzmann equation, which governs the evolution of the molecular velocity distribution function $f(t, \mathbf{x}, \mathbf{v})$[29]. Due to the complexity of the Boltzmann equation, particularly the fivefold collision integral, a direct analytical solution is in general not tractable. The description of the flow therefore requires dedicated numerical approaches capable of capturing the non-equilibrium molecular dynamics of the transitional regime, which are introduced in Chapter 4.1. For $Kn > 10$, the gas is so rarefied that a molecule, once reflected from the surface of a vehicle, will almost certainly travel to infinity without colliding with another air molecule. In this regime, aerodynamic forces are computed by summing the momentum transfer from individual molecular impacts on the surface, with incident molecular velocities described by Maxwell–Boltzmann statistics. This regime characterizes the flight environment of artificial satellites and space stations in Very Low Earth orbit (VLEO), where aerodynamic drag, although small, remains the primary cause of orbital decay[29].

3.3 Curved Bow Shock

The key phenomenon that defines the thermal and dynamic environment of atmospheric re-entry vehicles is the detached curved shock, also known as the bow shock. Unlike supersonic aircraft, which employ slender geometries to reduce wave drag, re-entry vehicles adopt blunt-body configurations specifically designed to generate a detached shock wave. This geometry is not optimised for cruise aerodynamic performance, but is instead driven by the need to manage the extreme thermal loads encountered during re-entry: the detached shock displaces the high-entropy, high-temperature shock layer away from the surface, significantly reducing the convective heat flux reaching the wall. In the absence of such a design approach, the aerothermal loads would likely exceed the structural and thermal limits of the vehicle. Understanding the complex flow structure between the shock and the body, where extreme entropy gradients, viscous interactions, and chemical transformations occur, is fundamental for the design of thermal protection systems (TPS) [36].

As the atmospheric density increases during the descent, the body velocity far exceeds the local speed of sound, preventing acoustic disturbances from propagating

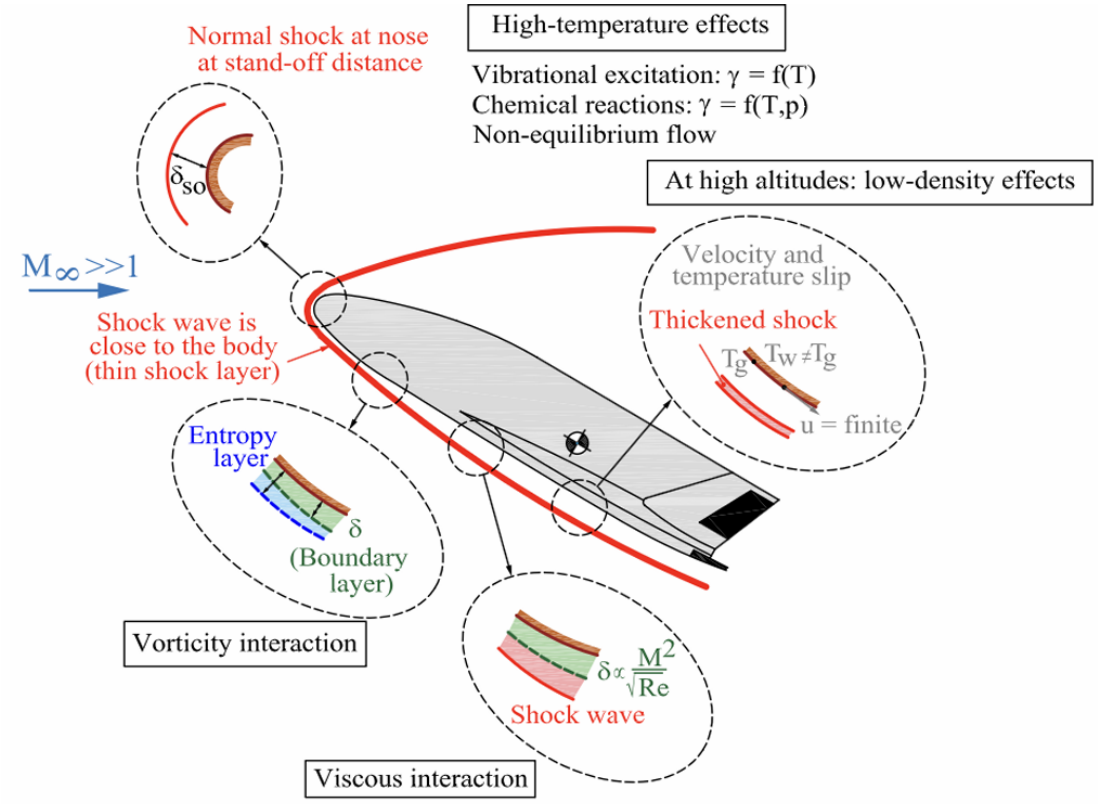

Figure 3.4: Schematic of hypersonic flow phenomena occuring around a vehicle [11]

upstream. The flow therefore has no forewarning of the obstacle, and the adjustment to the presence of the body occurs abruptly across a shock wave. A sharp discontinuity, the shock wave, therefore forms, instantaneously compressing and heating the gas. In the case of a capsule with a rounded nose, this shock assumes a curved shape and is positioned at a certain distance from the stagnation point, referred to as the stand-off distance (δ_{so}), as illustrated in Figure 3.4. The detached curved shock exhibits an inherently non-uniform character. At the vehicle's symmetry axis, the shock is locally perpendicular to the incoming flow, forming a normal shock at the stagnation point. Here, compression is maximum and the post-shock flow is brought to subsonic conditions, though it is important to note that this subsonic pocket is confined to the immediate vicinity of the stagnation region; away from the axis, the shock angle decreases and the downstream flow remains supersonic [36, 37]. Moving radially toward the shoulders of the vehicle, the shock gradually transitions into a weaker oblique shock, across which only the normal component of the upstream velocity is compressed while the tangential component is

preserved. The shock layer between the bow shock and the body surface is therefore a mixed subsonic-supersonic flow field, with a sonic line separating the two regions [37]. This variation of the shock angle along its curvature is the primary driver of the complexity of the hypersonic flow field. According to the Rankine-Hugoniot relations, the entropy jump across a shock strongly depends on the shock angle: a normal shock produces a much larger entropy increase than an oblique shock. Consequently, different streamlines crossing the shock at various distances from the symmetry axis experience different entropy increments, giving rise to the so-called entropy layer. This entropy gradient, according to Crocco's theorem, generates vorticity that interacts with the vehicle's boundary layer (vorticity interaction). The stand-off distance δ_{so} is a critical parameter for vehicle safety. It depends on the nose radius (R_n), the Mach number, and, most importantly, the density ratio across the shock (ρ_2/ρ_1). In extreme hypersonic conditions, the gas behind the shock reaches very high densities due to the excitation of internal degrees of freedom and chemical dissociation, causing the shock wave to approach the body surface, also known as thin shock layer. The shock compression converts the kinetic energy of the free stream into enthalpy; as demonstrated by Fay and Riddell (1958), the incident specific enthalpy increases quadratically with the free-stream velocity [38]:

$$h \approx \frac{1}{2}v^2. \tag{3.4}$$

In this high-enthalpy scenario, the shock layer is characterised by marked thermochemical nonequilibrium, where energy is distributed among vibrational excitation, molecular dissociation, and ionisation. Heat transfer to the vehicle occurs through three coupled mechanisms: convective heating, driven by the steep temperature gradient between the hot shock layer and the wall; radiative heating, which becomes significant at orbital velocities where the shock layer temperature is sufficient to emit thermal radiation; and catalytic heating, arising from the exothermic recombination of dissociated atoms on the vehicle surface. The overall heat balance at the wall is:

$$\dot{q}_{\text{conv}} + \dot{q}_{\text{rad}} + \dot{q}_{\text{cat}} = \epsilon\sigma T_w^4, \tag{3.5}$$

where the right-hand side represents wall reradiation, which constitutes the primary passive cooling mechanism for LEO re-entry vehicles.

Thermal protection systems (TPS) are designed to manage this heat input through one or more of the following approaches. Passive radiative cooling relies on high-emissivity surface materials that reradiate the absorbed heat; this mechanism is effective at moderate heat fluxes and is the basis of reusable ceramic tile systems such as those employed on the Space Shuttle. Ablative cooling is used when heat fluxes exceed the capacity of purely radiative systems: the TPS material undergoes

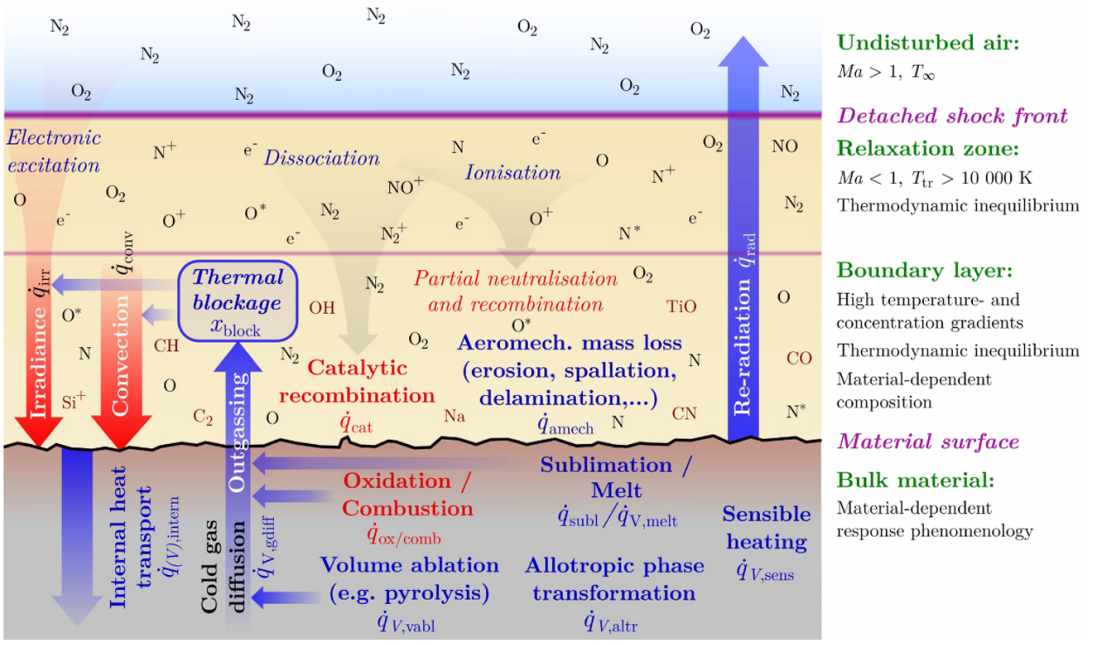

Figure 3.5: Schematic of molecular and heating processes occurring around the vehicle during re-entry [39]

controlled pyrolysis and surface recession, consuming energy through endothermic chemical reactions and injecting a protective gas layer into the boundary layer that further reduces convective heating. Active cooling, for example transpiration or film cooling, circulates a coolant through the structure or injects it at the wall, and is primarily considered for future reusable hypersonic vehicles.

A central role in all passive systems is played by heterogeneous catalysis, in which the exothermic recombination of atoms on the surface follows either the Eley-Rideal mechanism (direct gas-surface collision) or the Langmuir-Hinshelwood mechanism (diffusion and reaction between adsorbed species). The intensity of this phenomenon is quantified by the recombination coefficient γ, a critical parameter for the classification of TPS materials and the management of structural temperatures.

3.4 Motion in Flight

A body in flight within the atmospheric medium intrinsically possesses six degrees of freedom, assuming the rigid-body hypothesis. These degrees of freedom manifest as translational motions along the three spatial directions (fore-aft, lateral, and vertical) and rotations about the vehicle's three principal axes, conventionally identified as yaw, pitch, and roll. The mathematical description of this motion requires the adoption of appropriate coordinate systems, typically centered at the vehicle's center of gravity (CoG)[40].

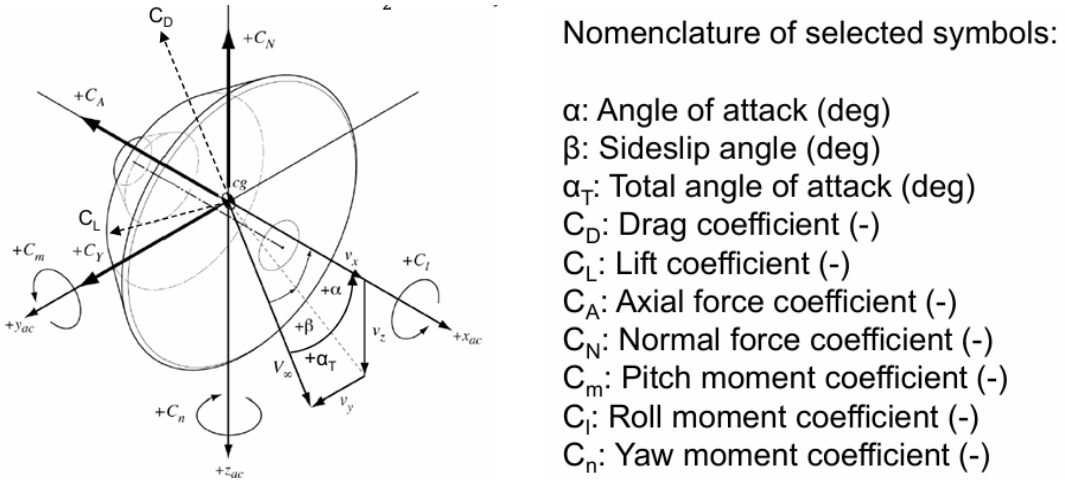

Figure 3.6: Definition of aerodynamic coefficients [11, 41]

3.4.1 Definition of Aerodynamic Coefficients

The modeling of aerodynamic forces is carried out through the definition of dimensionless coefficients that normalize the loads with respect to the freestream dynamic pressure:

$$q_\infty = \frac{1}{2}\rho_\infty V_\infty^2, \tag{3.6}$$

a reference area (A_{ref}), and a reference length (d_{ref}). For an axisymmetric body such as the ULPM, the reference area is usually taken as the maximum cross-sectional area, while the reference length corresponds to the body diameter.[40]

The fundamental definitions of force and moment coefficients are expressed as:

$$C_x = \frac{F_x}{\frac{1}{2}\rho_\infty V_\infty^2 A_{ref}}, \qquad C_{M_x} = \frac{M_x}{\frac{1}{2}\rho_\infty V_\infty^2 A_{ref} d_{ref}}. \tag{3.7}$$

The local aerodynamic loading is further characterised through the pressure coefficient c_p and the tangential stress coefficient c_τ, defined respectively as:

$$c_p = \frac{p - p_\infty}{q_\infty}, \qquad c_\tau = \frac{\tau_w}{q_\infty}, \tag{3.8}$$

where p is the local wall pressure, p_∞ the freestream static pressure, and τ_w the local wall shear stress. These distributions are integrated over the vehicle surface to yield the global force and moment coefficients.
In these expressions, F_x represents a generic aerodynamic force component along the x-axis, while M_x denotes the corresponding aerodynamic moment about the same axis. These coefficients are obtained by integrating the local pressure and shear stress distributions over the vehicle surface, which together constitute the global aerodynamic loading [42]. A complete aerodynamic characterization of the vehicle requires the use of angles describing the orientation of the velocity vector relative to the body axes. The angle of attack (α) and the sideslip angle (β) are the primary parameters. Visual analysis of re-entry configurations shows that aerodynamic forces are often decomposed either in the aerodynamic axis system (C_L, C_D) or in the body axis system (C_A, C_N).

3.5 Static Stability

Static stability is defined as the initial tendency of a vehicle to return to an equilibrium (trim) attitude after being disturbed. For a re-entry vehicle, this requires that the aerodynamic moments acting on the body produce a net restoring tendency whenever the vehicle deviates from its trim condition, ensuring that the thermal protection system or decelerator remains correctly oriented with respect to the incoming flow [43].

3.5.1 Equilibrium Conditions

For the pitching moment coefficient C_{m_y}, defined as $M_y = q_\infty\, A_{\text{ref}}\, L_{\text{ref}}\, C_{m_y}$, static stability requires the simultaneous satisfaction of three conditions. First, a restoring moment must exist, i.e., a negative pitching moment must be generated when the

vehicle is displaced from its equilibrium attitude, so as to drive it back toward the trim condition:

$$C_{m_y} < 0. \tag{3.9}$$

Second, the slope of the pitching moment curve evaluated at the trim point must be negative:

$$C_{m_\alpha} = \frac{\partial C_{m_y}}{\partial \alpha} < 0. \tag{3.10}$$

This condition ensures that if the vehicle nose moves upward, a nose-down restoring moment is generated, returning the vehicle toward its trim attitude. Additionally, the static margin must be not only positive but sufficiently large to guarantee robustness against perturbations encountered during flight. A margin that is merely positive but negligibly small renders the vehicle marginally stable, making the trim condition highly sensitive to external disturbances. Conversely, an excessively large margin, while providing strong resistance to perturbations, may result in an overly stiff attitude response. The admissible range of static margin therefore defines a stability envelope within which the vehicle is expected to operate throughout the re-entry trajectory.

Static stability is intrinsically linked to the relative positions of the Center of Gravity (CoG) and the Center of Pressure (CoP). The CoP is the point at which the resultant aerodynamic force acts such that no moment is generated about it. For aerodynamically stable flight, the CoG must be located ahead of the CoP with respect to the incoming flow. The distance between these two points defines the static margin; a positive and sufficient margin ensures that any normal force perturbation generates a stabilizing restoring moment [44].

As discussed in Chapter 2, the ULPM presents intrinsic stability challenges due to the aft position of the CoG. In the case of an expended upper stage, the CoG location is particularly unfavourable: with propellant depleted, the mass distribution shifts further aft along the body, making it inherently difficult to establish a positive static margin through aerodynamic means alone. The DAS concept addresses this by deploying conical panels at the aft end of the vehicle, shifting the CoP rearward and establishing a positive static margin without requiring additional ballast mass. However, the extent to which this shift is sufficient depends sensitively on the DAS geometry and the actual CoG position, motivating the parametric simulation campaign presented in Chapter 6. The influence of the DAS opening angle θ_2, fin length L_4, and CoG position on the static margin is the primary subject of that analysis [45].

3.5.2 Static Margin Evaluation

The longitudinal static stability of the investigated configurations was assessed by means of the static margin, derived from the aerodynamic coefficients obtained through the post-processing procedure. The static margin is defined as

$$SM = \frac{x_{NP} - x_{CoG}}{l_{ref}}, \tag{3.11}$$

where x_{NP} denotes the longitudinal position of the neutral point, x_{CoG} the longitudinal position of the centre of gravity, and l_{ref} the reference length. Since the neutral point is not directly available as a CFD output quantity, it was inferred from the aerodynamic derivatives with respect to the angle of attack, under the assumption of a linear aerodynamic regime. Within this framework, the pitching moment coefficient about the centre of gravity may be expressed as

$$C_m = C_{m,0} - \frac{x_{NP} - x_{CoG}}{l_{ref}} C_l, \tag{3.12}$$

where $C_{m,0}$ is the zero-lift pitching moment coefficient. Differentiating with respect to the angle of attack α yields

$$\frac{dC_m}{d\alpha} = -\frac{x_{NP} - x_{CoG}}{l_{ref}} \frac{dC_l}{d\alpha}, \tag{3.13}$$

from which the static margin is obtained as

$$SM = \frac{x_{NP} - x_{CoG}}{l_{ref}} = -\frac{dC_m/d\alpha}{dC_l/d\alpha}. \tag{3.14}$$

The aerodynamic derivatives $dC_m/d\alpha$ and $dC_l/d\alpha$ were evaluated by performing a least-squares linear regression of the CFD-computed coefficients over the considered angle-of-attack range. A positive static margin indicates that the neutral point is located aft of the centre of gravity, corresponding to a longitudinally statically stable configuration. A negative value denotes static instability, whereas values in the vicinity of zero are indicative of near-neutral stability.

3.6 Dinamic Stability

Dynamic stability analyzes how the vehicle responds over time to a perturbation, focusing on the damping of oscillations that occur around the trim position. The dynamic behavior of an axisymmetric re-entry vehicle is often modeled using a single-degree-of-freedom (1-DOF) second-order equation, analogous to a mass-spring-damper system:

$$I_{yy}\,\ddot{\alpha} - \underbrace{C_{m_\alpha}\,\alpha}_{\text{stiffness (static stability)}} - \underbrace{(C_{m_q} + C_{m_{\dot{\alpha}}})\,\dot{\alpha}}_{\text{dynamic damping}} = M(t) \tag{3.15}$$

Damping is governed by the quasi-steady interaction of the flow with the aft portion of the body and by the time lag of the wake (downwash lag). For a vehicle to be dynamically stable, the damping coefficient must be negative, ensuring that the energy of the oscillatory motion is dissipated into the surrounding fluid. It has been suggested in the literature that oscillation divergence may not arise solely from a constant negative damping coefficient, but rather from a wake-induced moment acting with a time delay t_{lag} relative to the body motion [46]. This phase lag between the body motion and the aerodynamic pressure response can inject energy into the system, leading to oscillations of increasing amplitude that may culminate in vehicle overturning prior to parachute deployment.

The dynamic stability of the vehicle is outside the scope of the present thesis, as its investigation would require unsteady flow field simulations, dynamic system identification procedures, and time-resolved experimental data [47]. The analysis is therefore limited to static stability, assessed through aerodynamic coefficients obtained from steady-state simulations.

3.7 Forced Rotation

Forced rotation (or spin stabilization) is a passive or semi-passive technique used to enhance the attitude stability of a rigid body and is based on the principle of conservation of angular momentum [48]. In an inertial reference frame, the variation of the angular momentum vector $\mathbf{L}$ is determined solely by the application of external torques $\boldsymbol{\tau}$, according to the fundamental relation:

$$\frac{d\mathbf{L}}{dt} = \boldsymbol{\tau}. \tag{3.16}$$

For a rigid body, the angular momentum is related to the angular rate $\boldsymbol{\omega}$ through the inertia tensor $\mathbf{I}$, expressed as:

$$\mathbf{L} = \mathbf{I}\boldsymbol{\omega}. \tag{3.17}$$

When a vehicle is spun rapidly about a symmetry axis, the magnitude of the angular momentum $|\mathbf{L}|$ increases significantly, which can provide the system with gyroscopic stiffness [49].

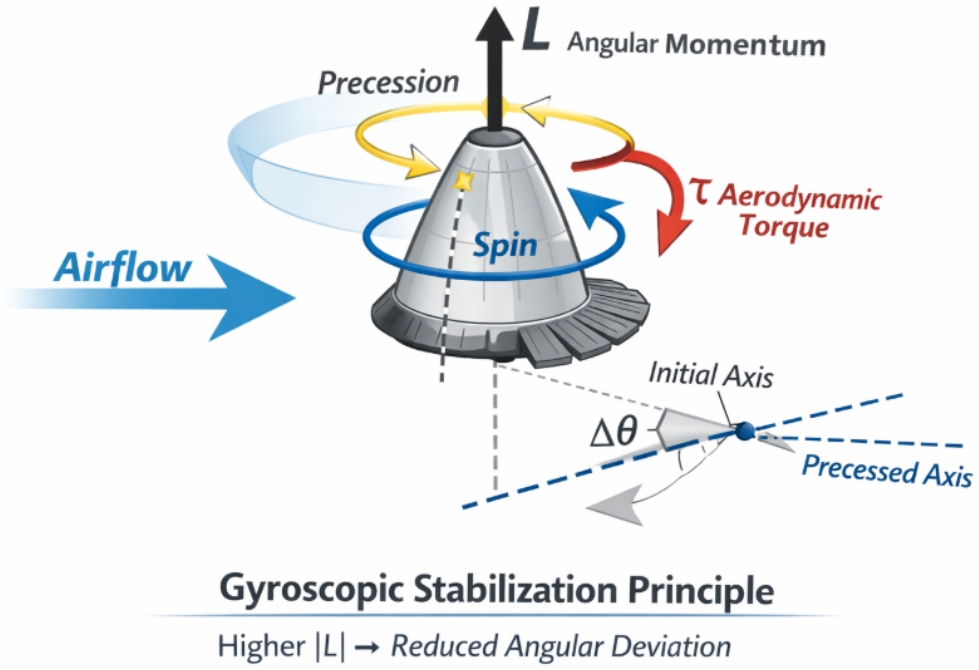

Figure 3.7: Principle of spin stabilization (AI-generated image)

3.7.1 Possible Implementations

Spin stabilization can be implemented through several approaches depending on vehicle design and mission requirements. The most common is mechanical spin-up, in which the vehicle is set into rotation prior to or during re-entry using deployable booms, offset masses, or internal flywheels. Alternatively, propulsive spin-up employs small thrusters or reaction control system (RCS) jets to impart angular velocity along the desired symmetry axis. A third option is aerodynamic spin, where canted fins or small vanes generate a torque due to the incoming flow, gradually spinning the vehicle during flight. Finally, off-centre masses or precessing mechanisms can be used to induce a natural spin or stabilise oscillations through gyroscopic coupling. Each approach involves trade-offs in terms of mass, mechanical complexity, control authority, and effectiveness under the combined aerodynamic and thermal loads of re-entry.

3.7.2 Advantages and Limitations

Spin stabilization is a mature and flight-proven technique, having been successfully applied in missions such as Pioneer and MMS, where passive gyroscopic stabilization was used without requiring active actuators during the critical re-entry or cruise phases. The primary advantage is the gyroscopic stability it provides: the aerodynamic torque $\boldsymbol{\tau}_{\text{aero}}$ induces a precessional motion of the angular momentum vector $\mathbf{L}$ rather than a catastrophic tumble [50]. The precession angular velocity can be estimated as:

$$\Omega_p \approx \frac{|\boldsymbol{\tau}_{\text{aero}}|}{I_{xx}\,\omega}, \tag{3.18}$$

where I_{xx} is the axial moment of inertia and ω the nominal spin rate. In addition, spin averages out mass asymmetries and thrust misalignments, reducing trajectory dispersion, and distributes the thermal load circumferentially across the TPS surface, mitigating local thermal gradients and preventing localised overheating [48].

However, the technique carries significant limitations. The spin rate does not remain constant during re-entry as atmospheric density and aerodynamic torques evolve, complicating attitude predictions. High spin rates induce centrifugal hoop stresses:

$$\sigma_\theta = \rho\,\omega^2 R^2, \tag{3.19}$$

which, combined with pressure-induced stresses, can subject structural materials such as Al-Li 2195 alloys to loads approaching their yield strength. A spin-up mechanism must be integrated prior to re-entry, adding mass, complexity, and cost. Furthermore, at high altitudes in rarefied flow conditions, the inverse Magnus effect acts in the opposite direction compared to continuum flow, potentially reducing

stability during the early phases of re-entry [51]. Finally, spin stabilization is incompatible with high-gain directional antennas, which require a fixed pointing direction.

3.7.3 Considerations on the Choice of Angular Velocity for Spin Stabilization

Forced spin stabilization is an established technique for passive attitude control during atmospheric re-entry, employed across a wide range of mission classes. However, identifying a target spin rate for the ULPM configuration is not straightforward, as the appropriate value depends on a combination of vehicle-specific and mission-specific factors that are not fully constrained within the scope of the present work. Rather than deriving a specific ω estimate, it is therefore more meaningful to identify the parameters on which such a choice would depend. The gyroscopic stiffness provided by spin stabilization scales with the axial moment of inertia of the vehicle and the square of the spin rate. For a large, propellant-depleted upper stage, the axial inertia is significantly higher than that of the small capsules and probes typically discussed in the spin stabilization literature, such as the Stardust re-entry capsule, for which a pre-entry roll rate was imparted in orbit to ensure attitude stability during descent. Directly transposing spin rates from such references would yield values incompatible with the inertial properties of the ULPM, as an equivalent gyroscopic stiffness would require a substantially lower ω for a heavier, larger-diameter stage. Furthermore, spin-stabilized capsules in the literature typically operate as part of a broader attitude control architecture, in which the roll rate is one element of an active guidance and control system. In such contexts, the spin rate is tuned to complement other control inputs rather than to provide stabilization in isolation, making direct comparison with a purely passive configuration inappropriate. The key factors that would govern the selection of a spin rate for the ULPM in a Dn2D context include: the axial and transverse moments of inertia of the expended stage; the magnitude and frequency of the aerodynamic disturbance moments expected along the re-entry trajectory; the mechanical feasibility of imparting and sustaining a given ω through a spin-up mechanism; the centrifugal structural loads on the DAS panels at the target spin rate; and the compatibility of the spin rate with any onboard systems sensitive to rotation. Whether forced spin stabilization would represent a meaningful complement to the passive DAS concept analyzed in this thesis therefore remains an open question, contingent on a dedicated attitude dynamics study and a more complete definition of the vehicle mass properties [52].

Chapter 4

Numerical Methods and Simulation Workflow

The aerothermal simulation of an upper stage during atmospheric re-entry between 120 km and 95 km altitude enables the characterization of the flow evolution from a transitional regime toward a near-continuum regime, and it requires moving beyond continuum models due to the high degree of gas rarefaction. In this altitude range, the high Knudsen number invalidates the Navier-Stokes equations, necessitating the solution of the Boltzmann equation through kinetic methods. This chapter analyzes the theoretical foundations of the Direct Simulation Monte Carlo (DSMC) and Bhatnagar-Gross-Krook (BGK) methods implemented within the PICLas framework of the Institute of Space Systems (IRS) in Stuttgart, defining the numerical rigor required for the study of various geometric configurations in a rarefied environment.[53]

The macroscopic description of a fluid, characterized by variables such as density, velocity, and temperature, is derived from the moments of the distribution function of microscopic parameters. When the molecular mean free path λ becomes comparable to the characteristic length L, the Knudsen number $Kn = \lambda /$ L indicates that intermolecular collisions are no longer sufficient to maintain the gas in a state of local thermodynamic equilibrium. In this particular thesis the characteristic length is the vehicle lenght.
The Boltzmann equation for a species s is defined as:

$$\frac{\partial f_s}{\partial t} + \mathbf{v} \cdot \nabla f_s + \frac{\mathbf{F}}{m_s} \cdot \nabla_{\mathbf{v}} f_s = \left[\frac{\partial f_s}{\partial t}\right]_{\text{coll}}, \tag{4.1}$$

where $f_s(\mathbf{x}, \mathbf{v}, t)$ represents the probability density of finding a particle with velocity $\mathbf{v}$ at position $\mathbf{x}$ and time t. The term on the right-hand side of the equation

corresponds to the collision integral, whose mathematical complexity renders analytical solutions for realistic geometries impossible. For this reason, particle-based methods are adopted to address this challenge by discretizing the distribution function into a large number of simulated particles, each assigned a statistical weight w_k representing a real number of physical molecules.

4.1 PICLas

PICLas is a three-dimensional, parallel, and modular simulation framework written in Fortran and based on the MPI standard for high-performance computing. Originally focused on combining the Particle-in-Cell (PIC) method for plasmas with the DSMC method for neutral gases, the code has been extended to include BGK and Fokker-Planck (FP) solvers, as well as modules for radiation and surface catalysis.[54, 55] The code architecture allows for the solution of Maxwell's or Poisson's equations for electromagnetic fields, coupled to the motion of charged particles [56, 57] For a neutral upper stage in re-entry, however, the DSMC and BGK-Flow modules constitute the primary components, even though also FP is also applicable. [58, 59]Computational grid generation is handled by the tool HOPR, which creates high-order, unstructured hexahedral meshes essential for accurately mapping the complex geometries of launch vehicle stages.[53, 60, 61]

4.1.1 DSMC Method

Unlike continuum-based methods, DSMC reproduces the gas behaviour by tracking the evolution of a representative ensemble of simulated computational particles, each assigned a statistical weight w_k representing a large number of real molecules [62]. The method provides a stochastic solution to the Boltzmann equation through operator splitting, which decouples particle motion and intermolecular collisions. Within each time interval Δt, particles first undergo ballistic transport according to their velocities, interacting only with domain boundaries or surfaces; intermolecular collisions and energy exchanges are then modelled probabilistically within each computational cell. The ability of DSMC to capture strong thermodynamic non-equilibrium arises directly from its kinetic formulation. The distribution function evolves freely from the simulated collisions, and non-equilibrium states emerge naturally[62, 54]. Molecular interactions are modelled using cross-section models such as the Variable Hard Sphere (VHS), which determines collision rates and post-collision velocity distributions, but does not itself impose equilibrium. Gas chemistry, including dissociation and recombination reactions, can be incorporated as an extension of the original method through additional probabilistic reaction models [62]. However, the stochastic nature of DSMC introduces statistical noise, which requires sampling a sufficient number of particles per cell to obtain accurate

macroscopic results. Consequently, the computational cost becomes prohibitive as gas density increases and re-entry altitude decreases, making DSMC most suitable for higher altitudes.

4.1.2 BGK Method

The Bhatnagar–Gross–Krook (BGK) model is a particle-based stochastic method, like DSMC, but replaces the complex binary collision operator of the Boltzmann equation with a linear relaxation term. Rather than simulating individual molecular collisions, the velocity distribution function f is assumed to relax toward a target equilibrium distribution f^{eq} at a characteristic collision frequency ν:

$$\left[\frac{\partial f}{\partial t}\right]_{\text{coll}} = \nu \left(f^{eq} - f\right). \tag{4.2}$$

The choice of target distribution determines the variant of the model. The standard BGK method uses a Maxwellian as f^{eq}, which however does not correctly reproduce the Prandtl number. The Ellipsoidal Statistical BGK (ESBGK) model, employed in the present work, replaces the Maxwellian with an anisotropic Gaussian distribution, recovering the correct transport coefficients [63]. Like DSMC, the stochastic particle implementation of BGK is subject to statistical noise, which requires a sufficient number of simulation particles per cell. However, BGK can operate with less stringent spatial and temporal resolution requirements than DSMC, making it significantly more efficient in denser flow regions where the mean free path is short and the flow approaches local equilibrium. In these conditions, BGK asymptotically recovers the Navier–Stokes solution in the continuum limit [64]. The main limitation of the BGK approach lies in its reduced accuracy in the transitional regime, where the forced relaxation toward the target distribution may fail to capture the correct non-equilibrium structure of the flow, particularly in the presence of strong shocks with highly anisotropic velocity distributions [65]. An additional source of inaccuracy in the present simulations is that chemical reactions are not yet incorporated in the BGK solver: while DSMC models reactions as outcomes of individual microscopic collisions, BGK reduces the collisional process to a collective relaxation, and the current implementation does not account for dissociation or recombination [66]. BGK therefore serves as an efficient solver for denser flow regions where overall numerical stability is prioritised, while DSMC remains the reference method in the highly rarefied regime.

4.2 Pre-processing and Atmospheric Model

The freestream conditions at each altitude are derived from trajectory data generated by STRAT, an in-house trajectory simulation tool developed at IRS [67]. For a given three-dimensional vehicle geometry and set of entry conditions, the code computes the re-entry trajectory and outputs the corresponding atmospheric parameters along the descent path, including local density, temperature, and velocity. In the present work, the tool is used to extract freestream conditions at the selected simulation altitudes, taking as input the altitude, velocity, and angle of attack of the upper stage.
For the comparative study of different geometric configurations, a methodological approximation was adopted: the atmospheric parameters at a given altitude were extracted from a single reference configuration and kept constant across all geometric variants at the same altitude. Although a change in DAS geometry technically affects the descent velocity and therefore the local flow properties, this variation is considered negligible within the altitude range investigated (120–95 km), allowing the purely aerodynamic effects of different designs to be isolated. The lower bound of 95 km was selected as a compromise between physical coverage of the re-entry corridor and computational feasibility, given the significant increase in simulation cost associated with denser flow conditions at lower altitudes. Extension of the campaign to lower altitudes remains an identified direction for future work.

4.2.1 Model Definition and Configuration Files

Once the atmospheric data have been obtained, the PICLas input files are configured. A five-species neutral air model (N, O, NO, O_2, N_2) is employed to capture thermochemical dissociation phenomena in the transitional flow regime. The global simulation parameters, including the end time, the Macro-Particle Factor (MPF) controlling the statistical weight of the simulated particles, and the reference to the mesh file (.h5) generated via HOPR, are specified in the parameter.ini file. The kinetic properties of the species, the collision model (Variable Hard Sphere, VHS), and the energy redistribution model (Larsen-Borgnakke) are defined in the DSMC.ini file.

Due to the high computational cost of DSMC and BGK simulations, all cases are executed on the Kerni HPC server at IRS Stuttgart. Input files are transferred via scp, and the parallel solver is launched in an MPI environment using 80 cores: mpirun -np 80 piclas parameter.ini DSMC.ini. The core count is chosen to maintain a ratio of approximately 100-200 mesh cells per core, minimising inter-node communication overhead. Computational cost increases significantly at

lower altitudes, where higher gas density leads to a larger number of simulated particles and collision events per time step.

4.2.2 Symmetries Plane and Domain Reduction

The axisymmetric geometry of the simplified CAD model allows the computational domain to be reduced, significantly lowering the number of mesh cells and simulated particles. In both the zero and non-zero angle of attack cases, the flow field retains a plane of symmetry coinciding with the pitch plane, and only one half of the domain is simulated, reducing the computational cost by a factor of two with no loss of physical accuracy. In PICLas, the symmetry boundary condition is imposed by specularly reflecting simulation particles that reach the symmetry plane: the velocity component normal to the plane is reversed while the tangential components are preserved. This is equivalent to mirroring the flow field across the symmetry boundary and ensures that the correct macroscopic quantities are recovered when the solution is reconstructed over the full domain.

4.3 Convergence Criteria and Simulation Verification

For steady-state simulations, convergence is assessed through the attainment of a statistical steady state. The temporal evolution of macroscopic quantities, in particular the total number density and translational temperature, is monitored; stationarity is considered reached when these quantities fluctuate around a stable mean value without systematic drift. Sampling of macroscopic properties is performed only after this condition is visually confirmed, to avoid contaminating the time-averaged results with transient data. For DSMC simulations, three microscopic quality criteria must be simultaneously satisfied throughout the domain. The ratio of the mean collision separation to the mean free path (MCS/MFP) must remain below 1, ensuring that collisions are spatially local. The maximum collision probability must remain below 0.8, preserving the validity of the stochastic collision scheme. Finally, the number of simulated particles per cell must remain above 10 to guarantee statistical significance [62, 53]. For BGK simulations, the equivalent criterion is that the maximum relaxation factor remains below 0.8, ensuring that the relaxation step does not overshoot the target distribution within a single time step [53]. The simulation workflow is supported by periodic output of state files in .h5 format, recording particle positions and velocities. These checkpoints allow the simulation to be restarted from the last saved state if the convergence criteria are not yet satisfied at the predefined end time, enabling adjustment of sampling parameters without losing accumulated computational progress.

Chapter 5

Methodology

This chapter presents the methodology adopted for the aerodynamic analysis of the re-entry configuration. The simulation workflow encompasses the definition of the atmospheric inflow conditions, the initialisation of the DSMC and BGK simulation files, the execution on the high-performance computing infrastructure, and the post-processing procedures used to extract and validate the results. The geometry of the reference vehicle and the simplified CAD model adopted for this study are described in Chapter 2, Section 2.2.3.

5.1 Simulation Workflow and Operational Setup

The execution of aerothermal simulations follows a structured workflow, starting from trajectory definition and concluding with the processing of macroscopic results on the high-performance computing server.

The simulation campaign is organised hierarchically according to three nested levels of variation: altitude, geometric configuration, and angle of attack. At the outermost level, the set of selected altitudes defines the freestream conditions for each campaign. The appropriate numerical method is selected based on the local Knudsen number $\mathrm{Kn} = \lambda/L$: at higher altitudes, where rarefaction effects dominate and intermolecular collisions are infrequent relative to molecule, surface interactions, the Direct Simulation Monte Carlo (DSMC) method is employed. At lower altitudes, as the mean free path decreases and the collision frequency increases, the velocity distribution function approaches a near-equilibrium Maxwellian form, making the BGK relaxation model a valid and computationally more efficient alternative to the full DSMC treatment. At the intermediate level, the geometric configuration of the Deployable Aerodynamic Stabilizer (DAS) is varied across a range of opening angles θ_2 and panel lengths L_4, as described in Chapter 6. For each configuration,

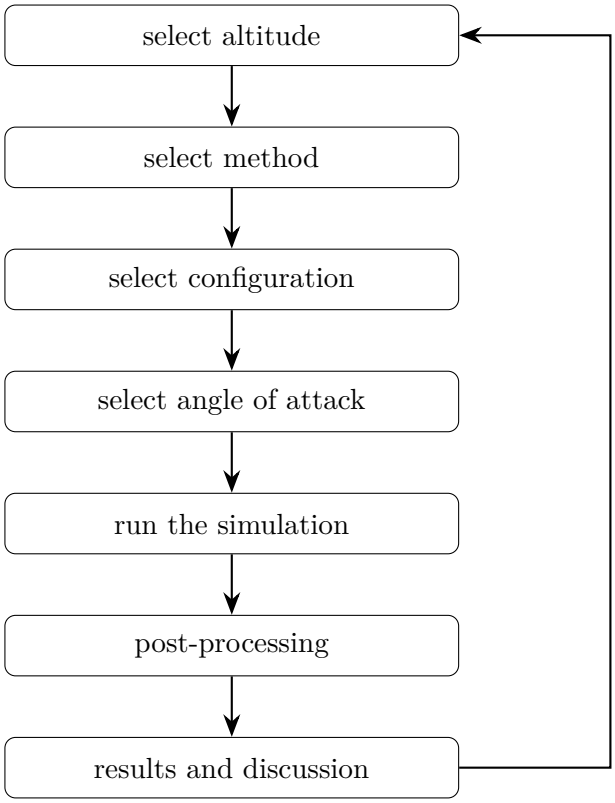

Figure 5.1: Analysis workflow

a set of angles of attack α is simulated at the innermost level to characterise the full aerodynamic response of the vehicle and evaluate static stability through the pitching moment coefficient C_{m_y} as a function of α.
Each simulation is executed on the Kerni HPC server at IRS Stuttgart and, upon convergence, undergoes post-processing to extract the aerodynamic force and moment coefficients. The results are then analysed and discussed, and the loop proceeds to the next configuration, angle of attack, or altitude as appropriate. The iterative structure allows systematic comparison across all parametric combinations and ensures that conclusions on passive stability are drawn consistently across the full altitude range of interest.

5.2 Numerical Simulation Approach

The simulation campaign was structured according to an incremental approach, aimed at validating the transition between numerical methods as atmospheric density increases along the re-entry profile. At 120 km, characterised by the highest

Knudsen number of the campaign, all geometric configurations were simulated exclusively using DSMC. This phase establishes the aerodynamic force and moment coefficients across the full range of DAS configurations in the rarefied regime, providing the reference dataset against which results at lower altitudes are compared. At 105 km, a cross-method validation was performed for a reference configuration ($\alpha = 60°$, $\beta = 0°$). Three simulation setups were compared: a full DSMC simulation, a BGK simulation initialised from a converged DSMC flow field (restart), and a BGK simulation initialised from uniform freestream conditions (from scratch). The agreement of aerodynamic coefficients between the two solvers at this intermediate altitude serves as a methodological gate: once the BGK model is verified to reproduce the flow physics accurately at 105 km, it is adopted as the primary solver for the lower-altitude phase. At 95 km, all simulations were performed exclusively using BGK. This choice yields a significant reduction in computational cost in a regime where the high collision frequency would render full DSMC prohibitive, while preserving the accuracy of the macroscopic quantities of interest. It is noted, however, that the BGK formulation employed here does not account for chemical reactions. As the altitude decreases and the aerothermal environment intensifies, dissociation and recombination reactions become increasingly relevant, particularly for the prediction of surface heat flux. The aerodynamic force and moment coefficients are expected to be less sensitive to chemistry than the heat flux, but this limitation should be considered when interpreting the results at 95 km, and motivates the inclusion of chemistry models as a priority in future simulation campaigns.

5.3 Post-Processing

Once the simulation has been completed and convergence verified, the extraction of macroscopic results is performed to assess the aerothermal performance of the vehicle. The post-processing workflow is aimed at transforming the cell-wise sampled data into global forces, moments, and heat fluxes. The first step involves exporting the final simulation state (e.g., `visuDSMC` files) into a structured tabular format, referred to as `output.csv`. This file contains, for each cell center on the surface mesh, the spatial coordinates, element area, force per unit area, and local heat flux. In this thesis, the symmetry of the simulated body was exploited by modeling only half of the geometry; therefore, the first stage of post-processing in MATLAB consists of reconstructing the complete body. Using the `mirror3dData` function, the dataset is expanded by applying reflection matrices (across the XY and XZ planes) or rotation matrices, ensuring that the integrated force calculations account for the full vehicle surface. The core of the analysis lies in a computational routine that processes the information contained in the CSV file exported from

the DSMC simulation. The total forces acting on the vehicle in the body-fixed reference frame are obtained by summing the contributions from each surface cell according to:

$$\mathbf{F}_{\text{tot}} = \sum_i \left(\mathbf{P}_{\text{unit},i} \cdot A_i\right), \tag{5.1}$$

where $\mathbf{P}_{\text{unit},i}$ represents the force per unit area associated with cell i and A_i is the corresponding cell area. Similarly, the aerodynamic moments with respect to a predefined Center of Gravity (CoG) are calculated as:

$$\mathbf{M}_{\text{tot}} = \sum_i \left(\mathbf{r}_i \times \mathbf{F}_i\right), \tag{5.2}$$

where $\mathbf{r}_i$ is the position vector from the CoG to the point of application of force $\mathbf{F}_i$. A crucial advantage of this methodology lies in its flexibility: any variation in the CoG location can be fully accommodated during post-processing by simply recalculating the moments within the MATLAB script, without the need to rerun the DSMC fluid-dynamics simulation.

5.3.1 Projected Area

A critical parameter for the proper non-dimensionalization of aerodynamic and aerothermal results is the projected area (A_{proj}), which depends on the angle of attack (α). The MATLAB script implements an analytical formula based on the projection of the vehicle's geometric components along the flow direction.
Considering the upper stage as composed of a nose cone, cylindrical body, and deployable aerodynamic system (DAS) 2.2, approximated as segments of cones or cylinders with radii r_1, r_2, r_3 and lengths l_1, l_2, l_3, the projected area is calculated as followed.

$$A_{\text{proj}} = \pi r_3^2 \cos(\alpha) + \frac{1}{2}\left[(r_1 + r_2)l_1 + 2r_2(l_2 - l_1) + (r_2 + r_3)(l_3 - l_2)\right]\sin(\alpha) \tag{5.3}$$

where r_1 is the initial radius of the forebody section (nose cone), measured after the first fillet or tip, r_2 is the radius of the main cylindrical body of the vehicle, r_3 is the maximum radius at the end of the DAS section (rear flare), l_1 is the length of the nose cone section, from the tip to the start of the cylindrical body, l_2 is the cumulative position at the end of the cylindrical body ($l_2 - l_1$ represents the actual length of the cylinder alone), l_3 is the total length of the vehicle including the extended DAS system ($l_3 - l_2$ represents the length of the flare section). This formulation allows accurate calculation of the projected area as a function of the angle of attack, enabling correct scaling of aerodynamic forces and heat fluxes in subsequent analyses. The resulting projected area values as a function of angle of attack are reported in Appendix A.1.

Chapter 6

Results and discussion

This chapter presents the results obtained during the numerical simulation campaign. The exposition is structured according to flight altitude, progressing from 120 km to 105 km and concluding at 95 km. This sequence reflects the transition across different flow regimes encountered during atmospheric re-entry, spanning from the free-molecular regime at higher altitudes to near-continuum conditions at lower altitudes. The primary focus of the analysis is the characterization of the aerodynamic force distribution acting on the upper stage surface, from which the force and moment coefficients are derived. Building upon the work of K.Weinmann [26], which has already examined the influence of the flight regime, expressed through the Knudsen number, for the baseline configuration, the present study extends the investigation to the aerodynamic design space. In particular, the influence of the deployable stabilizer opening angle, the center-of-gravity position, and the angle of attack on the static stability of the vehicle is systematically assessed across the three altitude regimes considered. Additionally, heat flux density distributions are examined, although these results must be interpreted with caution given the known limitations of the BGK implementation in capturing non-equilibrium thermochemical phenomena. For all the results presented, the projected area was evaluated for each configuration. The corresponding values are reported in Table A.1.

6.1 Simulations at Kn = 0.56

This section presents the numerical results obtained at an altitude of 120 km, corresponding to a Knudsen number of Kn = 0.56. According to the classification criteria discussed in Chapter 3, this value places the flow regime well within the transitional regime.

6.1.1 Influence of the Opening Angle

The investigation focuses on the influence of the opening angle on the flow field and aerodynamic coefficients. The opening angle was systematically varied from 30° to 70° in constant increments of 10°. Figure 6.1 show the velocity and temperature profiles for the 70° and 30° configurations respectively at zero angle of attack. The figures corresponding to the additional configurations are presented in the Appendix.

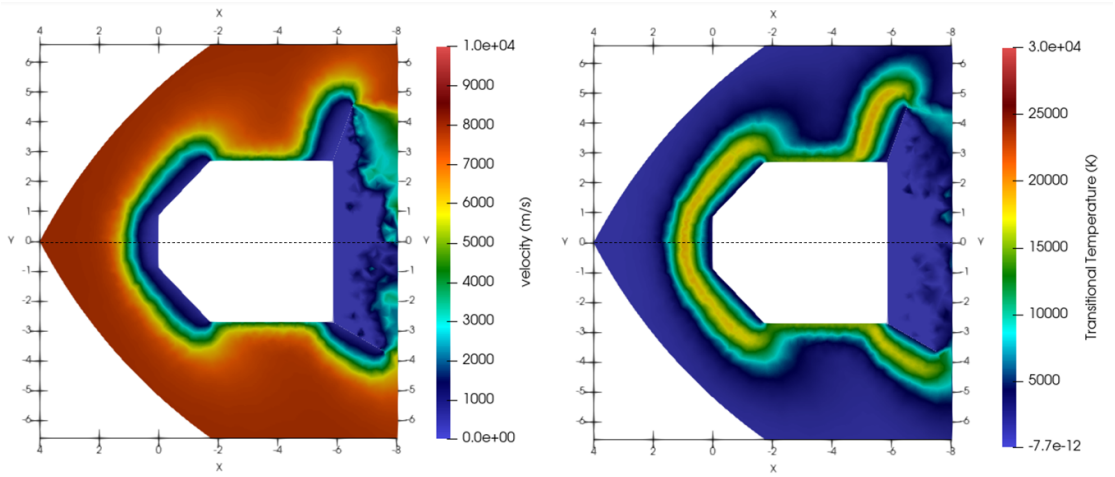

Figure 6.1: Flow field characteristics for the configuration with 70° opening angle (top) and 30° opening angle (bottom): velocity field (left) and total temperature (right).

In the flow field maps, a distinct detached bow shock is observed, located at a defined stand-off distance upstream of the nose and the deployable aerodynamic stabilizer. The temperature field closely follows the shock morphology, reflecting the dissipative character typical of a curved shock. Consistent with flow alignment along the symmetry axis, the shock structure is mirror-symmetric about the centerline. The peak temperature, reaching values close to 2.1×10^4 K, is confined within the frontal shock layer. In the region downstream of the upper stage, a wake characterized by very low velocities is identified, where fluid expansion promotes

the development of shear layers and low-velocity wake structures.

Effect on the Aerodynamics Coefficient and Forces

The following section presents the distribution of the pressure coefficient c_p as a function of the opening angle.

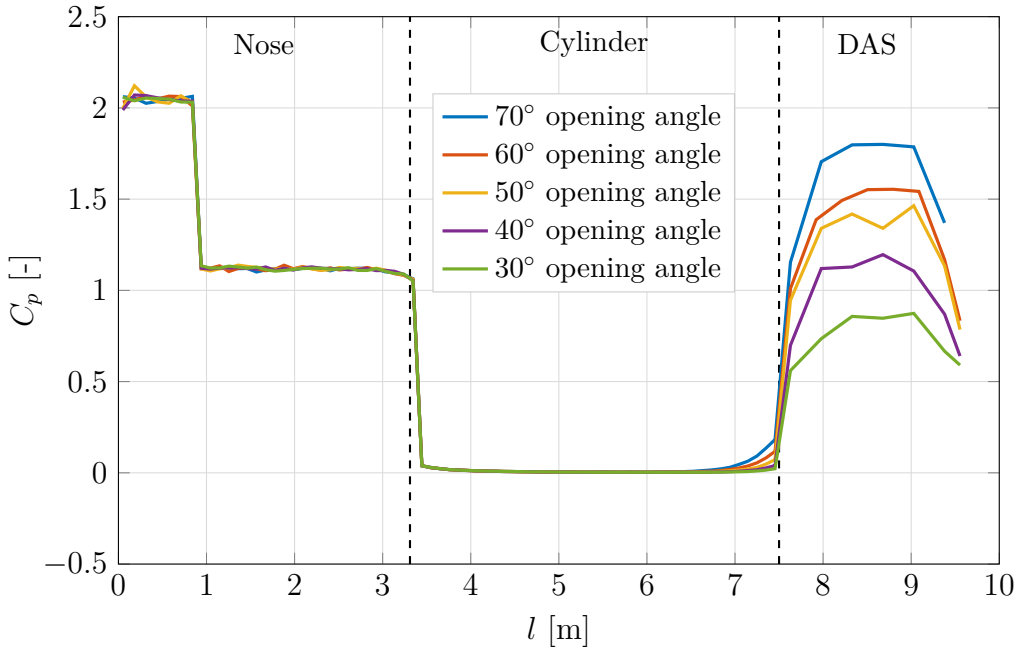

Figure 6.2: Pressure coefficient C_p along the surface for different DAS opening angles. AoA $= 0°$, $h = 120\,\text{km}$, $\phi = 0°$.

Figure 6.2 shows the pressure coefficient c_p distribution along the surface of the re-entry capsule for five different DAS opening angles, at zero angle of attack and an altitude of 120 km. Along the nose region ($l < 3.31\,\text{m}$), all configurations exhibit nearly identical c_p values of approximately 2.0, with a slight decrease to around 1.1 moving downstream, indicating that the stagnation and expansion behaviour in this region is independent of the DAS geometry. A sharp drop to $c_p \approx 0$ occurs at the nose-cylinder junction, and the coefficient remains essentially null throughout the entire cylinder section ($3.31 < l < 7.50\,\text{m}$), consistent with the shadow region characteristic of rarefied flow at this altitude. The most significant differentiation among configurations emerges in the DAS region ($l > 7.50\,\text{m}$), where c_p rises steeply for all cases and reaches a peak whose magnitude scales monotonically with the opening angle: the 70° configuration attains the highest value of approximately 1.8, while the 30° configuration peaks near 0.9, with the intermediate angles distributed accordingly. This behaviour reflects the stronger recompression and higher surface

impact pressure experienced by wider DAS geometries, which intercept a larger portion of the incoming rarefied flow. The subsequent decrease in c_p towards the aft end of the DAS is common to all configurations and is attributable to the local flow expansion past the peak compression point. Figure 6.3 presents the dimensional drag and lift forces as a function of the angle of attack for the five DAS opening angle configurations at $h = 120\,\text{km}$. The drag force D decreases monotonically with increasing AoA for all configurations, with the 70° opening angle consistently yielding the highest values (ranging from approximately 80.2 N at 0° to 68.0 N at 45°) and the 30° configuration the lowest (from 49.6 N to 57.0 N). Notably, the 30° and 40° configurations exhibit a non-monotonic behaviour, with drag increasing slightly beyond 15°–20° before recovering a decreasing trend. The lift force L increases monotonically from zero at 0° for all configurations, with saturation becoming apparent beyond 30°–35°. The spread among opening angles is moderate: at 45° AoA, L ranges from approximately 57.0 N (30° opening) to 68.0 N (70° opening), corresponding to a relative difference of approximately 19%.

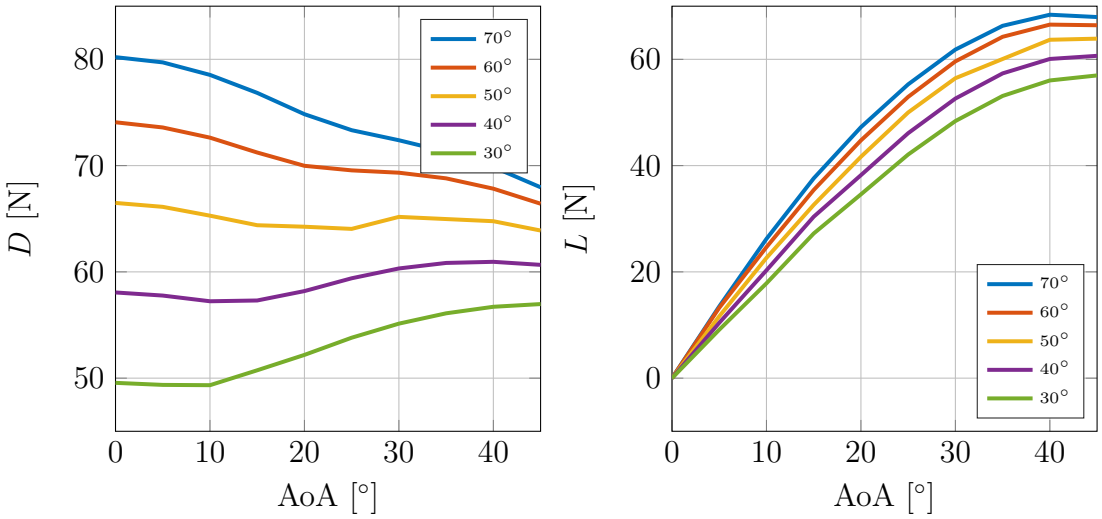

Figure 6.3: Drag D (left) and lift L (right) as a function of AoA for different DAS opening angles. $h = 120\,\text{km}$.

The corresponding non-dimensionalised coefficients C_d and C_l, normalised by the projected reference area $A_{\text{proj}}(\alpha)$ as defined in Section 5.3.1, are shown in Figure 6.4. As defined in Equation 6.1, the drag coefficient is normalised by A_{proj}, the freestream density ρ, and the flow velocity V:

$$C_{\text{D}} = \frac{D}{\frac{1}{2}\rho V^2 A_{\text{proj}}} \tag{6.1}$$

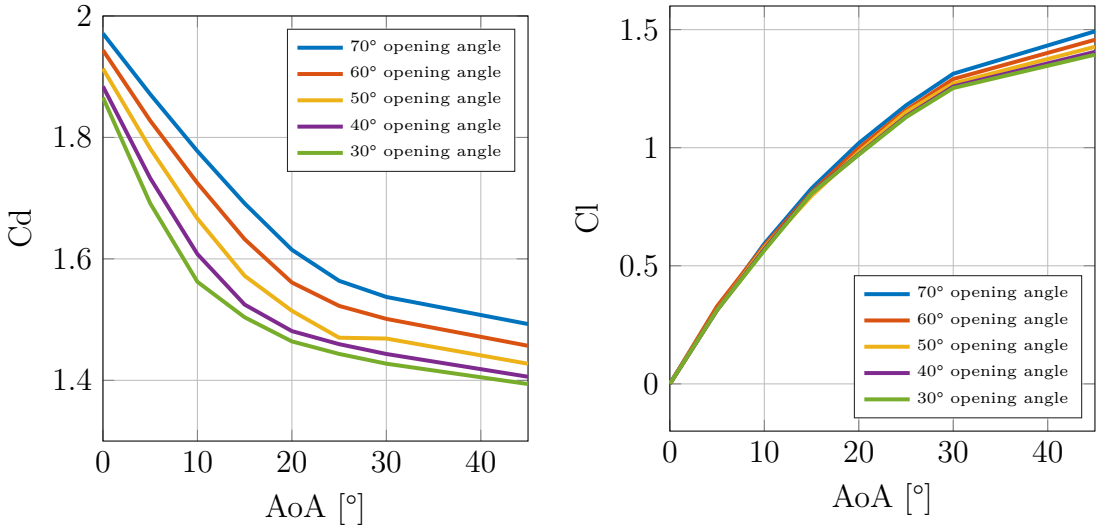

Figure 6.4: Trend of Cd (left) and Cl (right) at 120 km for different opening angle. The used reference area is the projected area listed in the table A.1.

Since ρ and V are fixed at a given altitude, the monotonic decrease of C_d with increasing AoA is primarily attributable to the growth of A_{proj}. As the upper stage pitches up, a larger cross-sectional area is exposed to the flow, reducing the normalised coefficient even though the actual drag force remains nearly unchanged. At 0° AoA, C_d spans from 1.866 (30° opening) to 1.971 (70° opening), a relative spread of approximately 5.6%. This spread narrows progressively with increasing AoA, converging to values between 1.394 and 1.493 at 45°, corresponding to a residual difference of approximately 7.1%. The 70° configuration consistently yields the highest C_d across the full AoA range, while the 30° configuration yields the lowest, confirming that a larger opening angle produces a proportionally greater increase in aerodynamic force than in projected area. The lift coefficient C_l increases monotonically from zero at 0° AoA, as expected from geometric symmetry, and exhibits progressive saturation beyond 30°. At 45°, C_l asymptotically approaches values between 1.394 (30° opening) and 1.493 (70° opening), a relative spread of only approximately 7.1%. The sensitivity of C_l to the opening angle remains considerably smaller than that observed for C_d across the full AoA range, confirming that the DAS geometry primarily governs the axial aerodynamic loading rather than lateral force generation.

Using the pitching moment coefficient Cm_y, and still focusing on the influence of the opening angle, some relevant differences can be observed. The formula used are explained in Section 3.5.1.

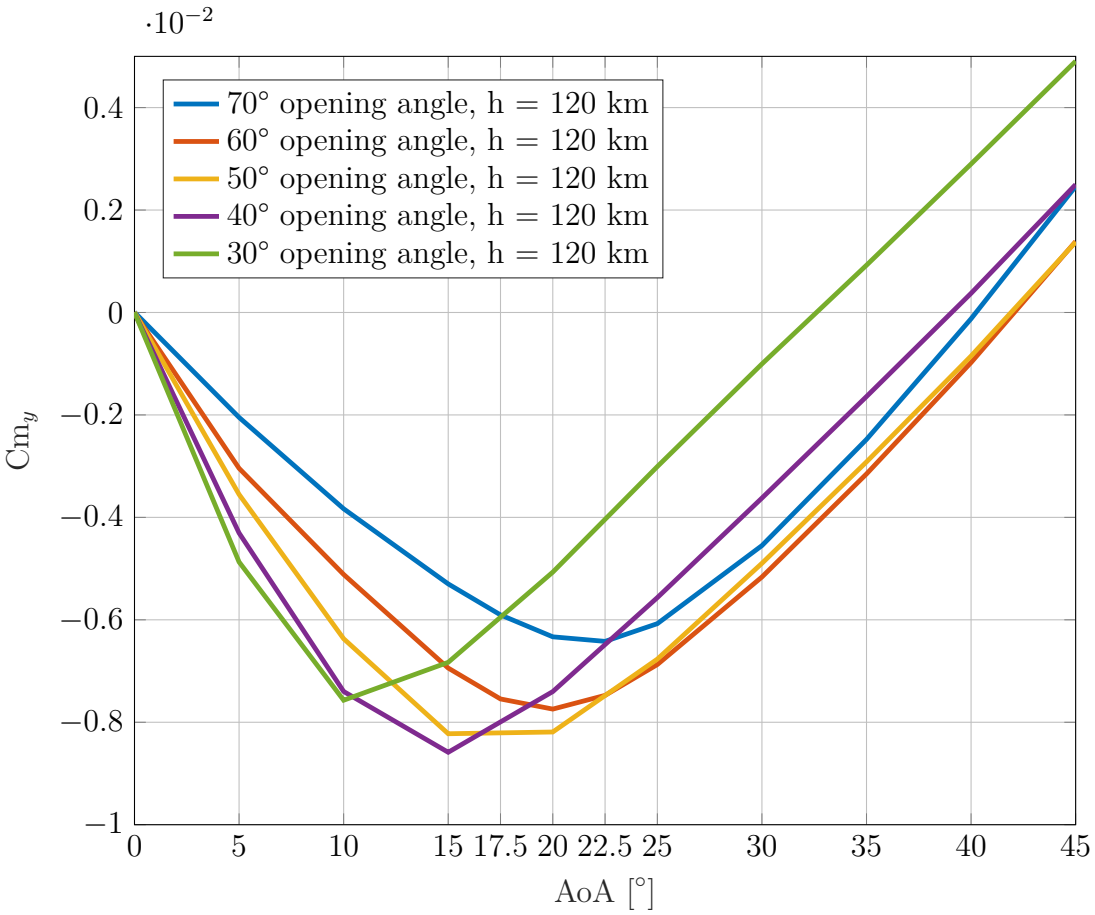

Figure 6.5: Cm_y for different configurations at 120km. The used reference area is the projected area listed in the table A.1.

Analysis of the various opening angle variation, shows that they are stable starting from AoA = 0°, where $C_{m_y} = 0$ due to the geometric symmetry of the body with respect to the velocity vector, up to a limiting value between 10° and 22.5°, depending on the specific aerodynamic configuration considered. The analysis aims to identify the influence of the opening angle on two key parameters: the angle of attack at which the restoring moment vanishes, and the magnitude of the moment coefficient itself. It should be noted that the presence of a restoring moment does not necessarily provide sufficient stability margin, as the actual dynamic behaviour depends on additional factors not considered in this static analysis. Regarding the angle at which Cm_y crosses zero, the 70° configuration maintains a negative slope of the moment coefficient up to approximately AoA = 22.5°, while the smaller opening angles lose their stabilizing moment at lower angles of attack. Regarding the magnitude of Cm_0, the 40° configuration exhibits the highest peak values, while

the differences between the remaining configurations are relatively small. The flow field velocity and temperature distributions for the 50° opening-angle configuration are reported as functions of the angle of attack in Figure 6.6, 6.7.

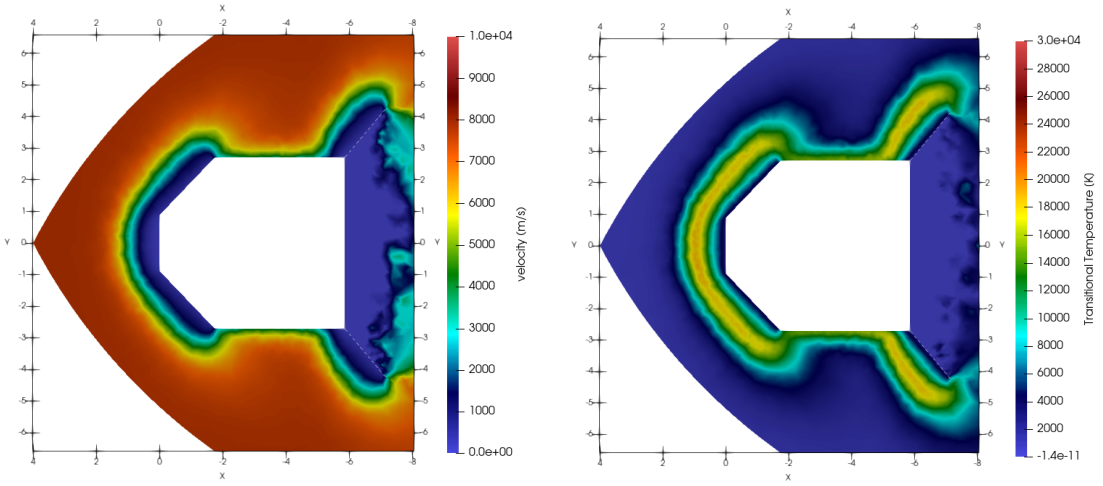

Figure 6.6: Flow field for the 50° configuration at AoA 0°: velocity (left) and total temperature (right).

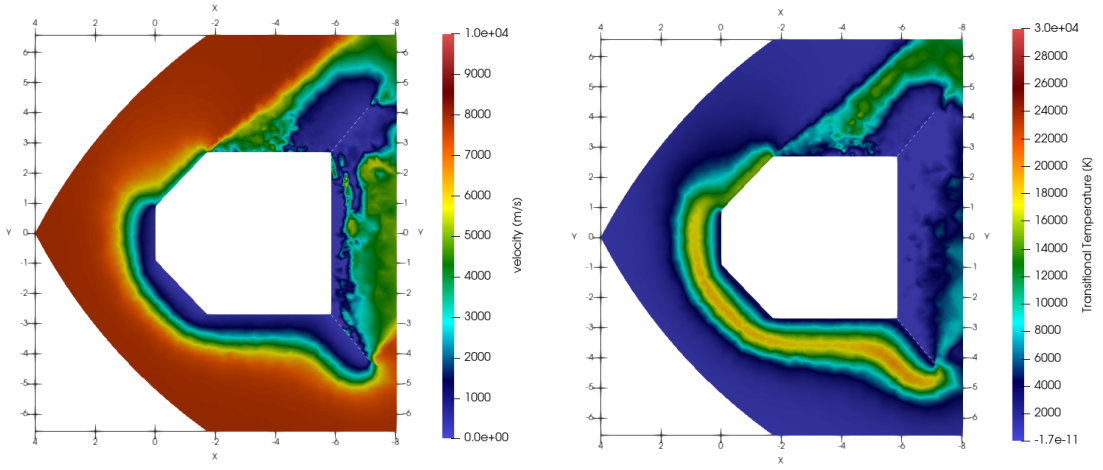

Figure 6.7: Flow field for the 50° configuration at AoA 45°: velocity (left) and total temperature (right).

As the AoA varies, the temperature distribution remains consistent with the shock wave morphology, showing a migration of the stagnation point from the symmetry

axis toward the windward shoulder exposed to the flow. The projected frontal area of the upper stage increases with angle of attack, acting as a larger hypersonic compression surface. The wake becomes asymmetric and no longer aligned with the geometric axis, with a more extended low-velocity region developing in the upper sector. It should be noted that the accurate characterisation of wake structures remains challenging even under perfectly symmetric conditions, as wake flows are inherently complex and sensitive to numerical parameters. The figures corresponding to the additional angles of attack are presented in the Appendix A.1.

Figure 6.8 shows the pressure coefficient c_p and the tangential stress coefficient c_τ along the windward surface for the 50° opening angle configuration at two angles of attack, AoA = 0° and AoA = 30°, at an altitude of 120 km.

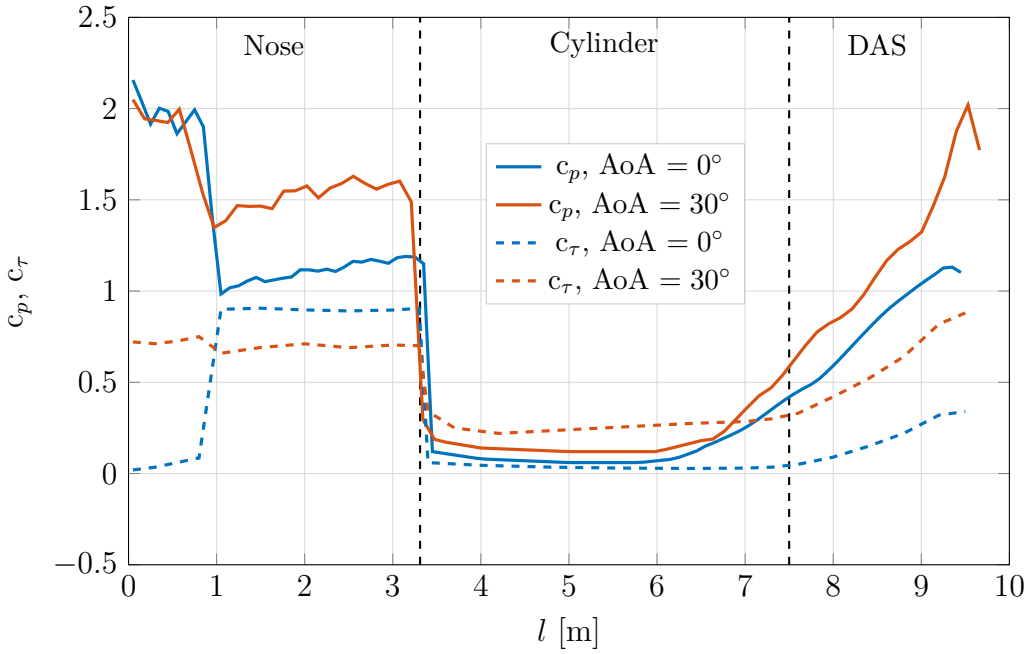

Figure 6.8: Pressure coefficient c_p (solid) and tangential coefficient c_τ (dashed) along the windward surface for AoA = 0° and 30°.

Along the nose region ($l < 3.31$ m), c_p reaches its maximum value of approximately 2.0 at the stagnation point for both angles of attack, then decreases progressively toward the nose-cylinder junction. At AoA = 30°, the stagnation value is slightly lower and the distribution more gradual, consistent with the asymmetric flow impingement on the windward side. The tangential coefficient c_τ is elevated in the nose region, particularly at higher AoA, reflecting the increased shear stress due to the stronger velocity gradients along the inclined surface. In the cylinder region

($3.31 < l < 7.50\,\mathrm{m}$), c_p drops sharply to near-zero values at AoA $= 0°$, consistent with the shadow region characteristic of rarefied flow, where molecules impinge primarily on the frontal surfaces. At AoA $= 30°$, however, c_p remains significantly higher throughout the cylinder, as the windward side is now directly exposed to the incoming flow. The tangential coefficient c_τ similarly increases with AoA in this region, indicating a higher shear stress contribution to the total aerodynamic load. In the DAS region ($l > 7.50\,\mathrm{m}$), both configurations show a steep rise in c_p, reaching a peak near the leading edge of the deployable panels. At AoA $= 30°$, the peak value reaches approximately 2.0, considerably higher than the AoA $= 0°$ case, reflecting the stronger recompression on the windward DAS surface at higher incidence. The tangential coefficient c_τ also increases toward the aft end of the DAS, though its magnitude remains smaller than c_p throughout, confirming that normal forces dominate the aerodynamic loading in this regime.

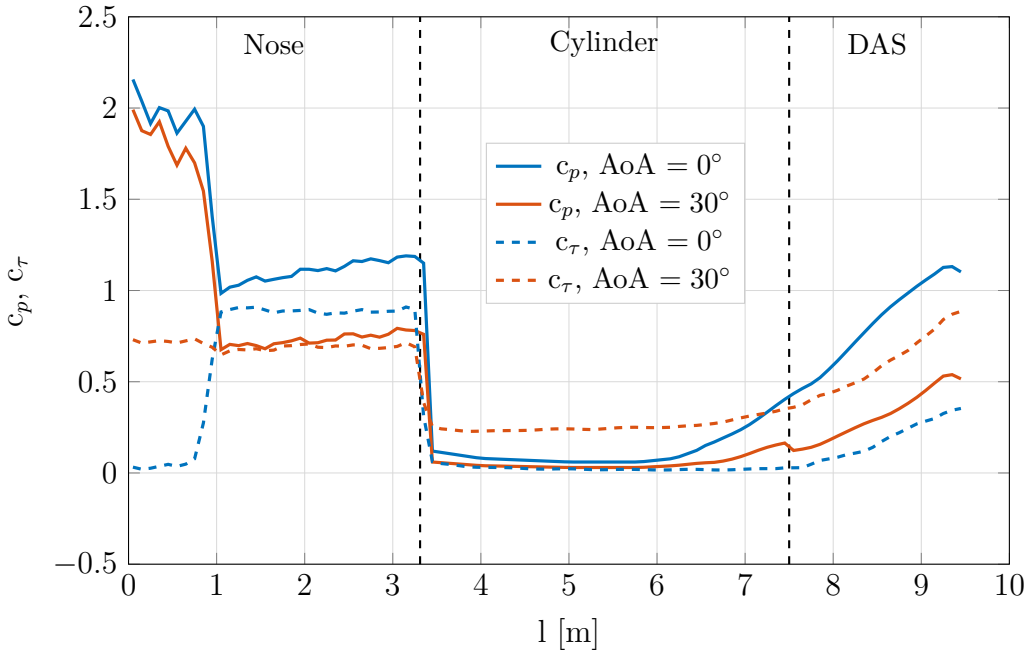

Figure 6.9: Pressure coefficient C_p along the leeward surface for different angles of attack. 50° opening angle, $h = 120\,\mathrm{km}$.

Figure 6.9 presents the pressure coefficient c_p and tangential stress coefficient c_τ along the leeward surface for the 50° opening angle configuration at $h = 120\,\mathrm{km}$. At AoA $= 0°$, the leeward distribution is symmetric to the windward counterpart, confirming the absence of any net pitching moment. At AoA $= 30°$, a marked asymmetry develops between the two surfaces. In the nose region, the leeward stagnation peak reaches approximately 1.6, compared to 2.0 on the windward side,

corresponding to a reduction of approximately 20%. In the cylinder region, the leeward c_p remains near zero for both angles of attack, whereas the windward side sustains values of approximately 0.3-0.4 at AoA = 30°, a difference consistent with the shadow effect characteristic of rarefied transitional flow. The most significant asymmetry occurs in the DAS region, where the windward pressure peak reaches approximately 2.0 while the leeward peak is limited to approximately 1.1, representing a differential of approximately 45%. This pronounced pressure imbalance between the windward and leeward DAS panels constitutes the primary aerodynamic mechanism responsible for the generation of a net restoring pitching moment about the vehicle center of gravity, directly underpinning the static stability behaviour discussed in Section 3.

Summarising, the influence of the DAS opening angle on the aerodynamic coefficients at $h = 120\,\text{km}$ is found to be limited. The c_p and c_f distributions along both the windward and leeward surfaces remain largely invariant across the range of opening angles considered, with differences confined to the DAS region. Similarly, the lift coefficient C_L shows negligible sensitivity to the opening angle across the full AoA range, with the curves for all configurations remaining nearly coincident. The drag coefficient C_D, by contrast, exhibits a more discernible dependence on the opening angle, with larger opening angles consistently yielding higher values due to the greater projected frontal area exposed to the flow. This confirms that at 120 km, the opening angle primarily governs the axial aerodynamic loading, while its influence on the pressure distribution and lateral force generation remains secondary.

6.1.2 Influence of the Center of Gravity

The effect of the center of gravity position on static stability is analyzed for the 60° opening-angle configuration. As a reference, the nominal CoG position is taken from the baseline configuration defined in [26], located at $x_\text{CoG} = 5.8\,\text{m}$ from the nose tip along the longitudinal axis. In practice, the CoG position is subject to variation depending on the flight configuration, residual fuel load, and the mass of the DAS system itself. To account for this variability, the CoG is varied by ±5% along the x-axis relative to the nominal value, corresponding to a displacement of approximately $\pm 0.3\,\text{m}$, which represents a structurally realistic range in terms of spatial arrangement and subsystem placement.

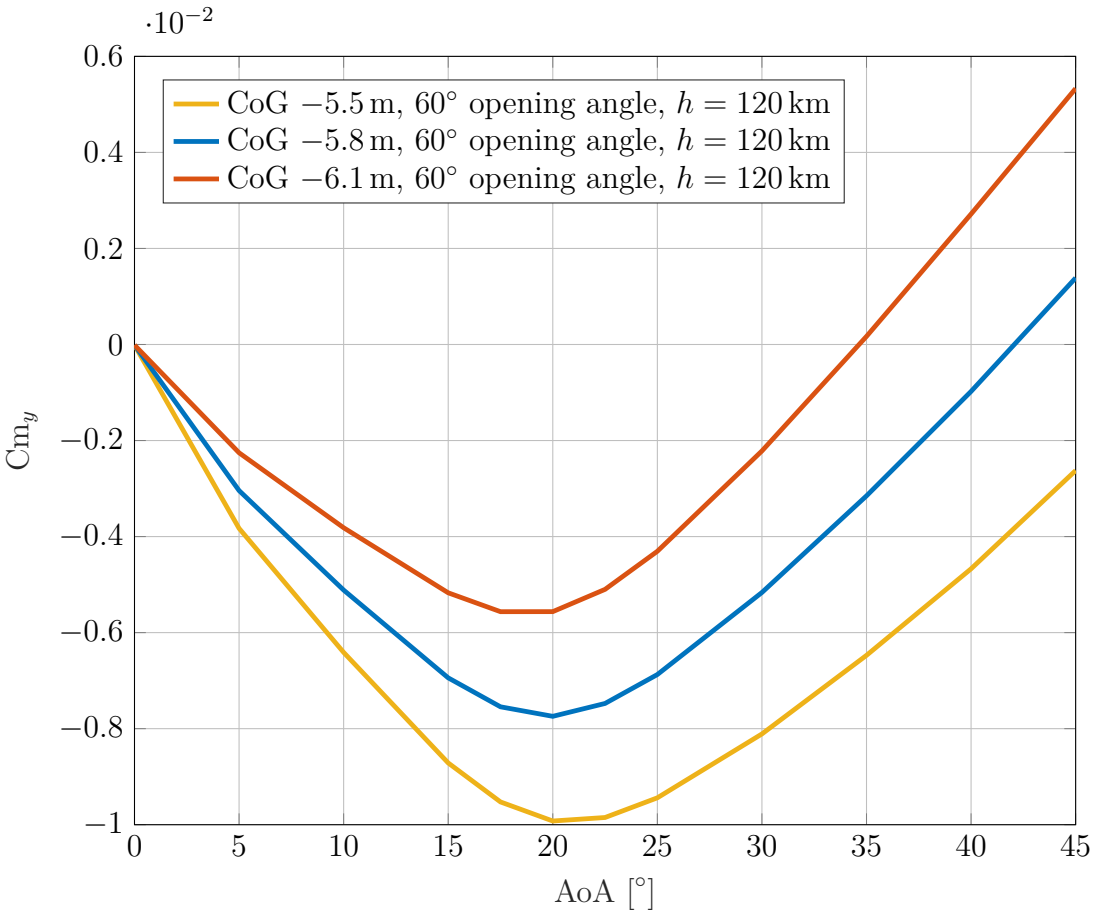

Figure 6.10: Trend of the pitching moment coefficient Cm_y at 120 km (60° opening angle) for different center of gravity positions.

The aerodynamic pitching moment M_y is reported in Figure 6.11 for the configurations exhibiting the highest static stability margins, from which several considerations regarding the re-entry dynamics can be drawn.

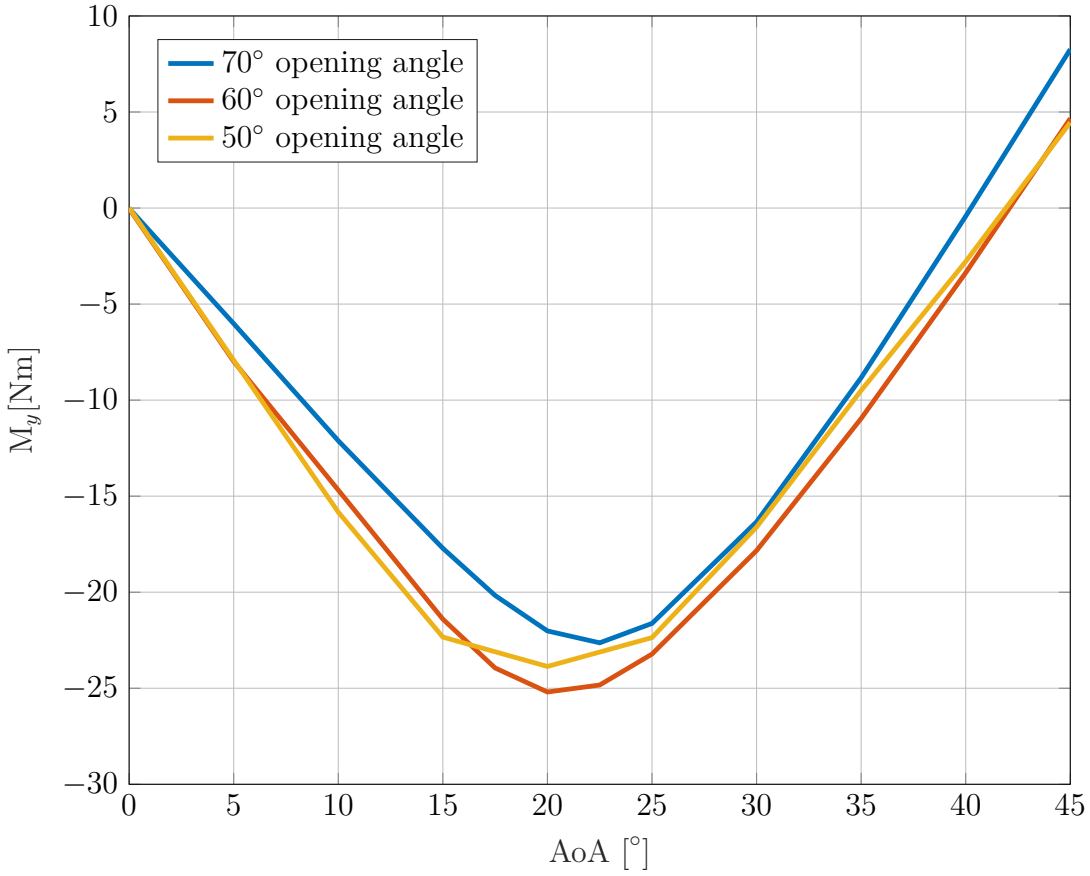

Figure 6.11: Trend of the pitching moment M_0 as a function of the angle of attack (AoA) for different opening configurations at 120 km altitude.

At an altitude of 120 km, the aerodynamic moment M_y exhibits values on the order of 10 Nm. This is consistent with the highly rarefied flow conditions at this altitude: the atmospheric density is extremely low and, although the vehicle presents a large reference area, the momentum transferred per molecular impact remains insufficient to generate significant aerodynamic loads. As shown in the following sections, these values increase by approximately one order of magnitude at 105 km and further at 95 km, in accordance with the rapid increase in atmospheric density along the re-entry trajectory. A direct comparison with values reported in the literature should be treated with caution, as pitching moment magnitudes are sensitive to the choice of reference length, reference area, and the specific vehicle geometry and attitude considered.

6.1.3 Influence of the DAS Panel Length

The panel length L_4 represents a key geometric parameter of the DAS, as it directly governs the aft reference area and therefore the magnitude of the aerodynamic forces and moments generated during re-entry. Two configurations are compared throughout the simulation campaign: a baseline panel length of 2.0 m and an extended configuration of 2.5 m, both at a fixed opening angle of 60°. The influence of this parameter on the drag coefficient C_d, lift coefficient C_l, and pitching moment coefficient C_{m_y} is assessed across all three altitudes.

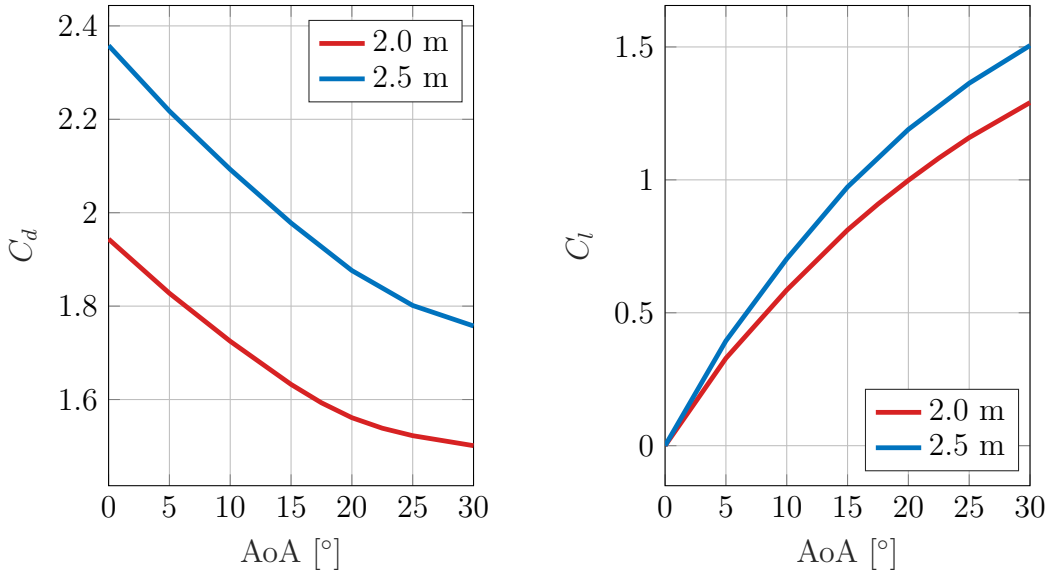

Figure 6.12: C_d(left) and C_l (right) as a function of AoA for the 60° opening angle configuration. Panel lengths 2.0 m and 2.5 m. $h = 120$ km.

The drag coefficient $C_d$is consistently higher for the 2.5 m configuration across the full AoA range, reflecting the larger projected area exposed to the flow. At AoA = 0°, C_d increases from 1.944 for the 2.0 m panel to 2.358 for the 2.5 m panel, a relative increase of approximately 21%. This difference narrows with increasing AoA, reducing to approximately 17% at AoA = 30°, as the projected area growth with incidence partially offsets the geometric advantage of the longer panel. The lift coefficient C_l increases monotonically with AoA for both configurations and shows a more pronounced sensitivity to panel length than $C_d$at high incidence: at AoA = 30°, C_l reaches 1.291 for the 2.0 m configuration and 1.505 for the 2.5 m configuration, a relative difference of approximately 17%, confirming that the longer panel generates a proportionally larger lateral force component at high angles of attack.

Figure 6.13 presents the pitching moment M_y as a function of AoA for the two panel length configurations at $h = 120\,\text{km}$.

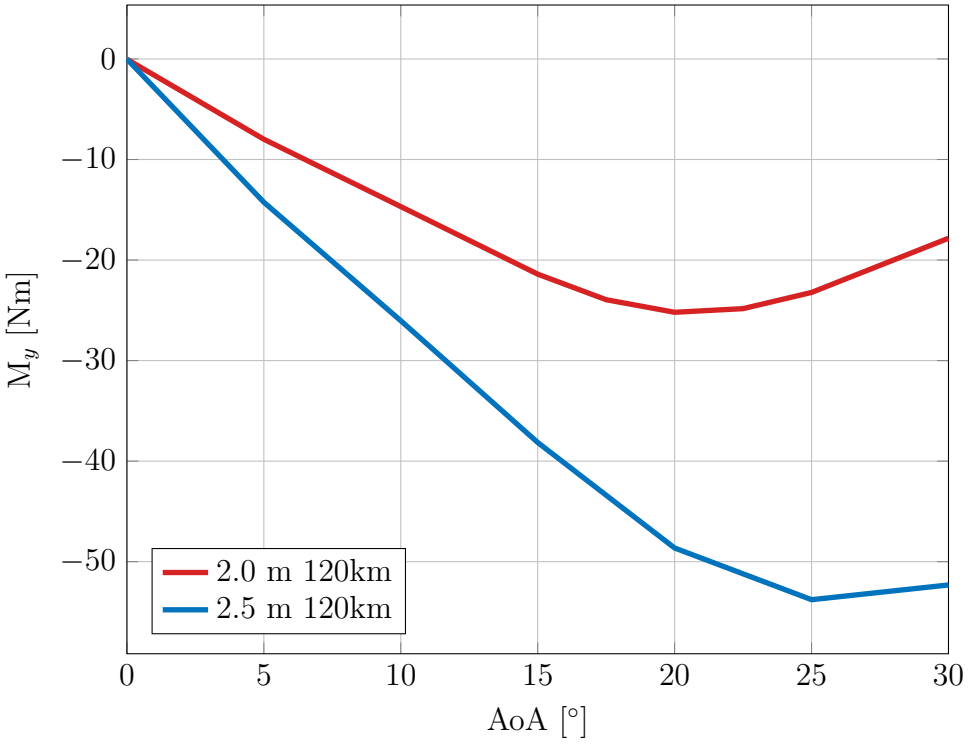

Figure 6.13: Pitching moment M vs. AoA at 120 km.

The 2.5 m configuration generates a substantially larger restoring moment across the full AoA range: at the peak, reached near AoA = 20°, M_y reaches −53.8 Nm for the 2.5 m panel compared to −25.2 Nm for the 2.0 m configuration, representing an increase of approximately 113%. This confirms that panel length has a dominant influence on the absolute restoring moment, significantly exceeding the effect of the opening angle observed in the previous sections. Both configurations exhibit moment saturation beyond AoA ≈ 20°–25°, with M_y recovering toward less negative values at higher incidence. Neither configuration reaches a trim point within the simulated AoA range, indicating that the stable equilibrium attitude lies beyond 30° for both panel lengths at this altitude.

6.2 Simulations at Kn = 0.06

The analysis proceeds at an altitude of 105 km, corresponding to a Knudsen number of Kn = 0.06. This value places the flow in the transitional regime, at reduced rarefaction compared to the 120 km case. The increase in atmospheric density results in a shorter mean free path, modifying the shock-layer structure and the surface heat flux distribution relative to the higher-altitude results. Preliminary simulations at this altitude were performed using DSMC; however, the higher gas density increased the computational cost by approximately one order of magnitude compared to the 120 km simulations, making convergence times prohibitive. The BGK method, described in Chapter 4.1, was therefore adopted as the primary solver. Prior to its general application, the physical consistency of the BGK approximation in this regime must be verified against DSMC results. To this end, the reference configuration (60° opening angle, $\alpha = 0°$) was simulated using three approaches: DSMC alone, BGK initialised from a converged DSMC flow field (restart), and BGK initialised from uniform conditions (from scratch).

The results obtained from the different numerical procedures are presented in order to enable a detailed comparative analysis and to verify the mutual consistency of the solvers. In order to reduce computational times, a hybrid approach was initially tested, consisting of a DSMC pre-initialization followed by numerical refinement using the BGK method, as illustrated in Figure 6.14. This strategy was implemented to overcome the excessive runtimes required by the DSMC solver alone to reach a convergent steady state. The rationale behind this approach was to leverage the DSMC solver's capability to account for chemical reactions, thereby establishing the correct gas phase composition before switching to the BGK method, which is computationally more efficient, for the final convergence phase. The results confirmed the validity of this approach: the velocity and temperature profiles exhibit a high level of agreement with the DSMC reference solution, with minimal and localized deviations. However, despite the method's accuracy, the reduction in computational time remained insufficient for the requirements of the simulation campaign. Consequently, the BGK method was applied from the initial time step, and the corresponding results are reported in the following.

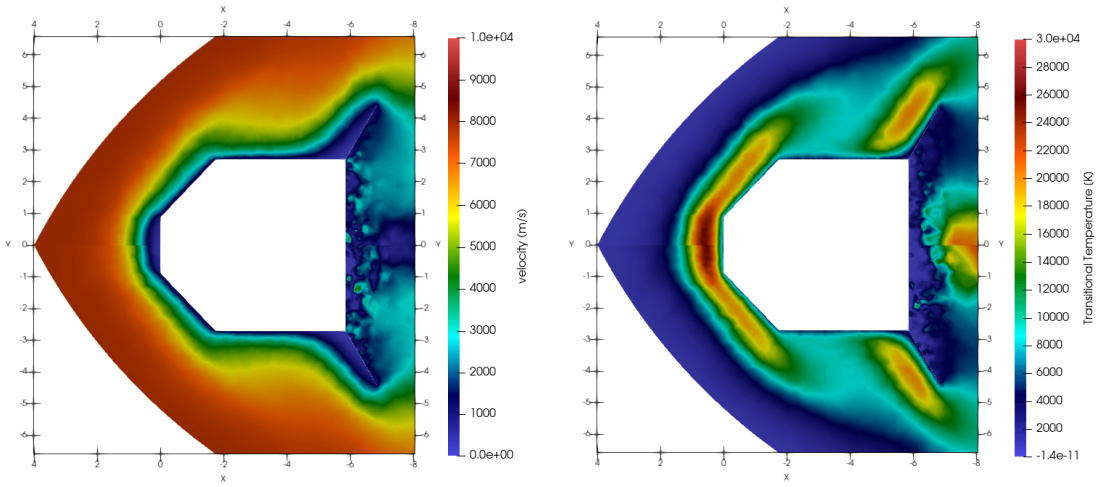

Figure 6.14: Comparison between hybrid DSMC–BGK solution (top) and purely DSMC solution (bottom) at 105km: velocity field (left) and total temperature (right).

As shown in Figure 6.15, the DSMC and BGK methods exhibit good overall agreement, although some differences can be identified.

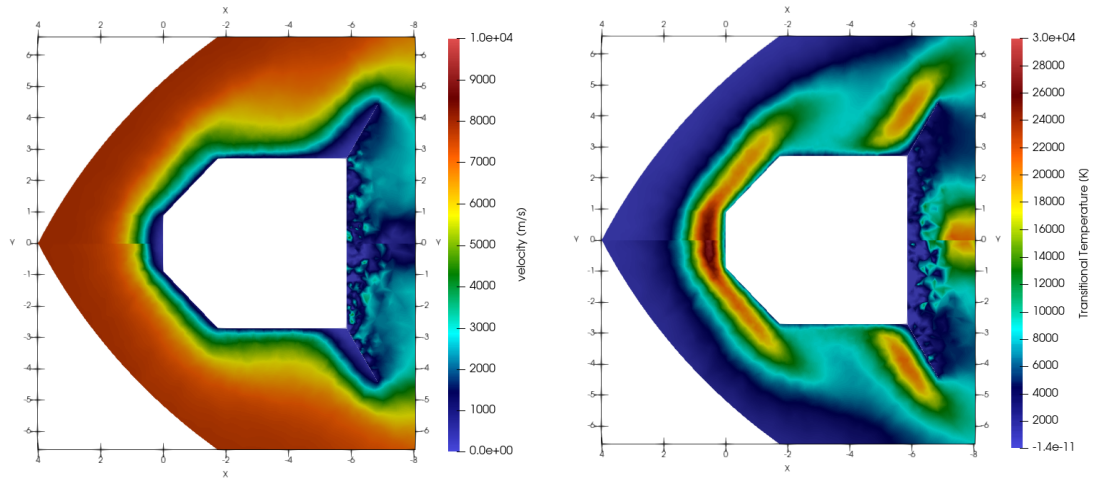

Figure 6.15: Comparison between DSMC solution (top) and BGK initialized from macroscopic conditions at initial time (bottom) at 105km: velocity field (left) and total temperature (right).

With reference to the velocity field, discrepancies arise when comparing the solutions along the centerline (symmetry axis). In the BGK solution, the upstream region

ahead of the shock is more extended than that predicted by DSMC, while the shock thickness along the stagnation streamline is smaller compared to the DSMC result. Concerning the temperature profile, a very good agreement is observed across the entire computational domain. However, the BGK solution displays a more pronounced translational temperature region, with peak values approximately 21% higher than those obtained with DSMC. These findings underline the limitations of the BGK approach, mainly due to instrinct differences in the two methods and the absence of chemical reactions in the model.

Figure 6.16 presents the heat flux distribution $\dot{q}$ along the vehicle surface for three simulation method together with the relative deviation $\Delta\dot{q}$ of each method with respect to the DSMC reference solution, for the 60° opening angle configuration at $\alpha = 0°$ and $h = 105\,\text{km}$. In the nose region ($l < 3.31\,\text{m}$), all three methods predict a peak heat flux of approximately 33-38 kW m^{-2} at the stagnation point, followed by a monotonic decrease toward the nose-cylinder junction. The DSMC solution yields systematically lower values in this region compared to BGK and DSMC+BGK, with deviations reaching approximately +15 % for BGK. This discrepancy is physically attributed to the endothermic nature of the dissociation reactions included in the DSMC chemistry model. A fraction of the thermal energy is absorbed by the chemical reactions, reducing the net heat flux deposited on the surface. The BGK formulation, which does not account for chemical reactions, therefore overestimates the heat flux in the high-temperature shock layer ahead of the nose.

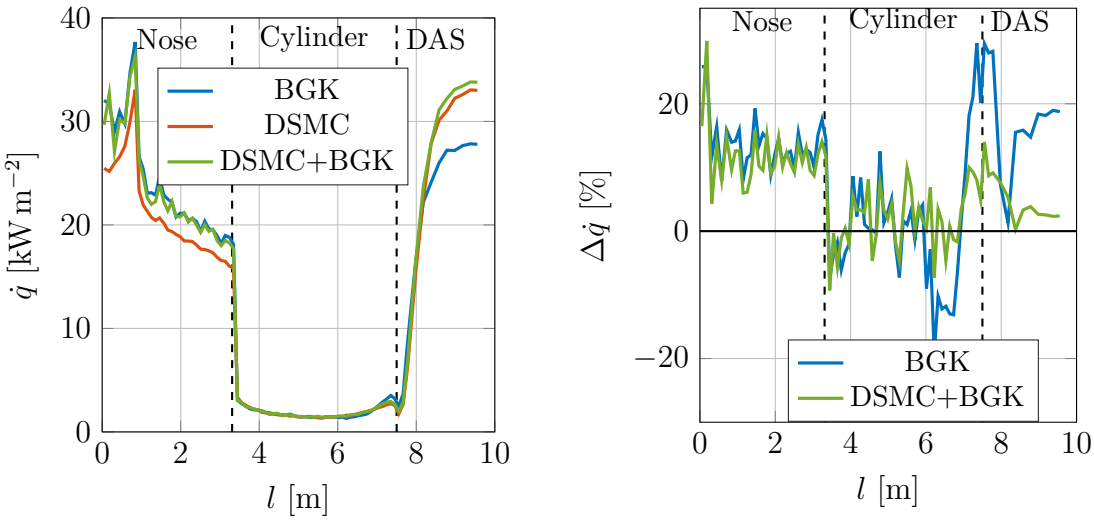

Figure 6.16: Heat flux distribution (left) and relative deviation with respect to DSMC (right) for three simulation methods. 60° opening angle, $\alpha = 0°$, $h = 105\,\text{km}$.

In the cylinder region ($3.31 < l < 7.50\,\mathrm{m}$), $\dot{q}$ drops sharply to near-zero values for all methods, consistent with the shadow effect in rarefied flow, and the three solutions converge to within a few percent of each other. In the DAS region ($l > 7.50\,\mathrm{m}$), the heat flux rises steeply, reaching peak values of approximately 28-34 $\mathrm{kW\,m^{-2}}$ at the leading edge of the deployable panels, where the DSMC solution again predicts the highest values. The deviation of BGK with respect to DSMC reaches approximately $-15\,\%$ at the DAS peak, with a local excursion up to $+29\,\%$ near the panel leading edge. The physical origin of this behaviour is not uniquely attributable to a single cause. The effect might be due to several reasons: it might be due to BGK itself, since the BGK collision operator does not reproduce the full non-equilibrium distribution of DSMC. If the particle number at the DAS is not sufficient, a statistical deviation may appear. Alternatively, in the DSMC simulation with chemistry, recombination reactions may occur between the nose and the DAS, by which energy is stored in the molecular bond. The particles that subsequently impinge on the DAS in the DSMC simulation thus carry a higher internal energy, leading to an increased heat flux on the deployable panels.
Overall, the relative deviations between the three methods remain within approximately $\pm 30\,\%$ across the entire surface, with the DSMC+BGK hybrid approach consistently providing the closest agreement with the full DSMC solution. These levels of discrepancy are considered acceptable for the purposes of the present parametric analysis, confirming that the BGK-based simulations provide a reliable and computationally efficient alternative to full DSMC for the aerothermal characterisation of the ULPM at this altitude.

The results of the simulations at this altitude are reported below. Since the computational times remain relatively high and given the large number of simulations required, only the configurations with 50°, 60°, and 70° opening angles were simulated. Figure 6.17 presents the dimensional drag and lift forces as a function of the angle of attack for the three DAS opening angle configurations at $h = 105\,\mathrm{km}$.

Effect on the Aerodynamics Coefficient and Forces

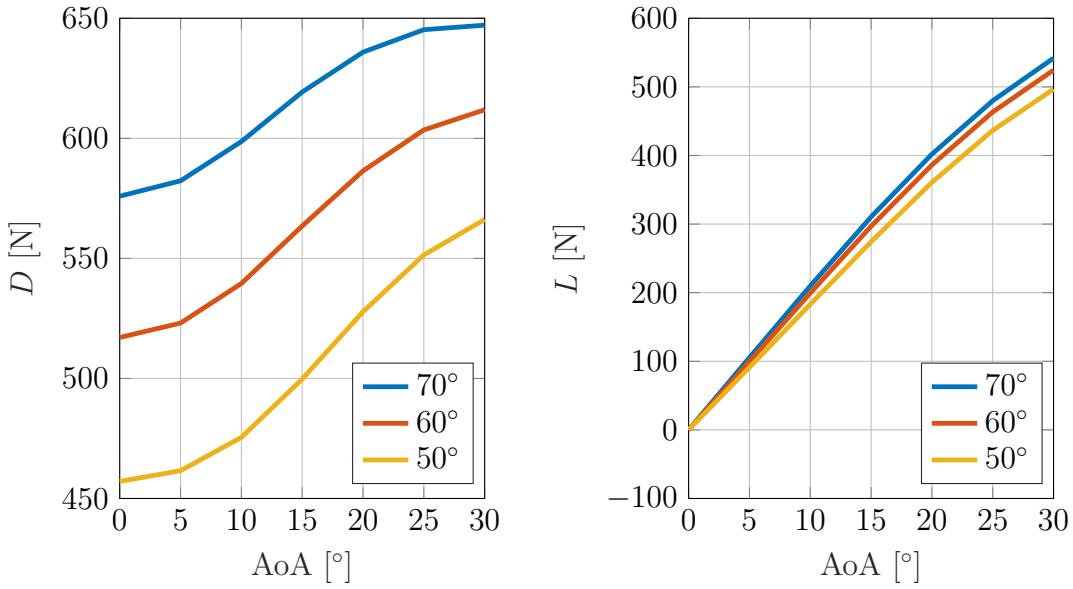

Figure 6.17: Drag D (left) and lift L (right) as a function of AoA for different DAS opening angles. $h = 105\,\text{km}$.

Unlike the behaviour observed at 120 km, the drag force D increases monotonically with AoA for all configurations, reflecting the denser flow conditions at 105 km where the increased molecular flux on the windward surfaces dominates over the projected area growth. At AoA = 0°, D ranges from 457 N (50° opening) to 576 N (70° opening), a relative spread of approximately 26%. At AoA = 30°, this spread narrows to approximately 14%, with values ranging from 566 N to 647 N, as the aerodynamic loading becomes increasingly governed by the AoA rather than the DAS geometry. The lift force L increases monotonically from near-zero at AoA = 0° for all configurations, with saturation becoming apparent beyond 25°. At AoA = 30°, L ranges from 497 N (50° opening) to 542 N (70° opening), a relative difference of approximately 9%, confirming that the opening angle exerts a stronger influence on the axial than on the lateral force component.

The corresponding non-dimensionalised coefficients C_d and C_l, normalised by the projected reference area $A_{\text{proj}}(\alpha)$ as defined in Section 5.3.1, are shown in Figure 6.18.

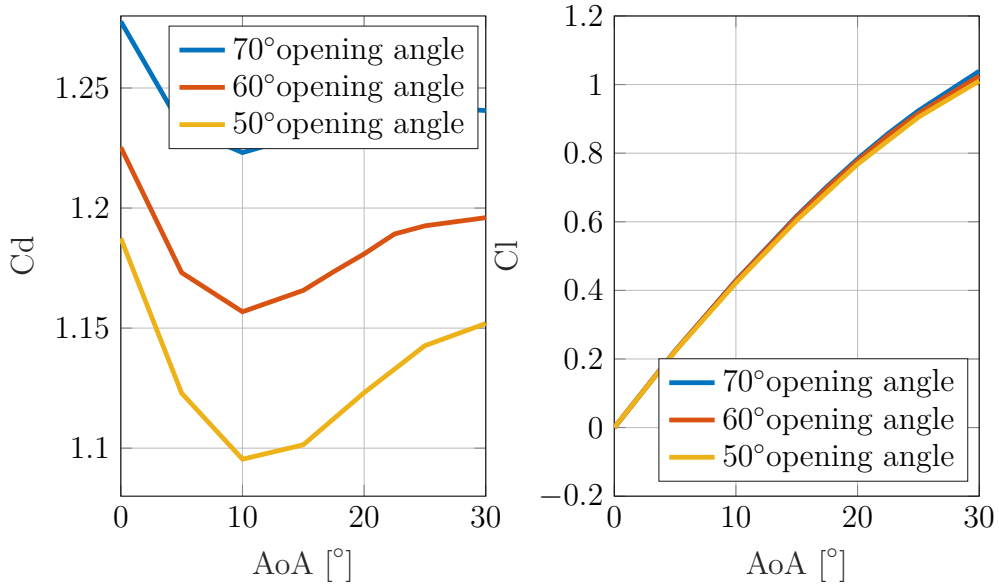

Figure 6.18: Comparison of drag coefficient (Cd) and lift coefficient (Cl) versus angle of attack (AoA) for 50°, 60°, and 70° opening angles.

The drag coefficient C_{D} exhibits a non-monotonic behaviour with AoA for all configurations, decreasing from its maximum at 0° to a minimum near 10°–15°, before increasing again toward 30°. This reflects the competing effects of the projected area growth, which reduces C_{D}, and the increase of the actual drag force with AoA, which dominates at higher incidence. The 70° configuration consistently yields the highest C_{D} across the full AoA range, with a spread of approximately 9% between the 50° and 70° cases at 0° AoA. The lift coefficient C_{L} increases monotonically from zero and is largely insensitive to the opening angle, with all three configurations differing by less than 3% at 30° AoA.

Figure 6.19 presents the pitching moment coefficient C_{m_y} as a function of the angle of attack for the three DAS opening angle configurations at $h = 105\,\mathrm{km}$.

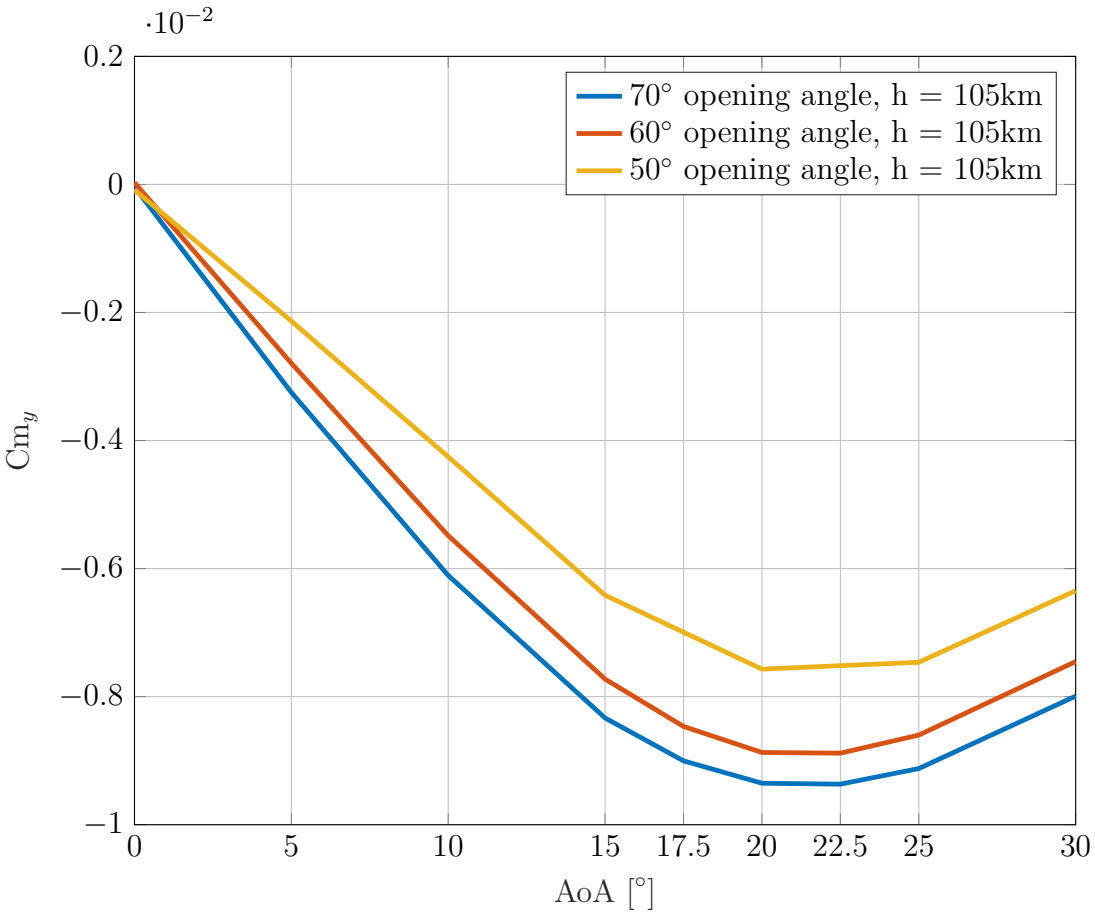

Figure 6.19: Comparison of the moment coefficient Cm_y for different opening angles at an altitude of 105 km.

At AoA = 0°, C_{m_y} is effectively zero for all configurations, consistent with the axisymmetric flow conditions. As the angle of attack increases, C_{m_y} becomes increasingly negative for all geometries, confirming the presence of a restoring pitching moment and a negative slope $C_{m_\alpha} < 0$ throughout the simulated range. The magnitude of C_{m_y} increases with the opening angle: at AoA = 22.5°, the 70° configuration reaches a peak of -9.37×10^{-3}, compared to -8.88×10^{-3} for the 60° case and -7.57×10^{-3} for the 50° case. Beyond the respective peak values, the magnitude of C_{m_y} decreases for all configurations, indicating the onset of moment saturation at high incidence. The 70° opening angle exhibits the largest $|C_{m_y}|$ across the full AoA range and therefore provides the greatest restoring moment among the configurations considered.

The velocity and total temperature distributions for the 70° opening-angle configuration are reported below as functions of the angle of attack. The remaining angles of attack are reported in the appendix.

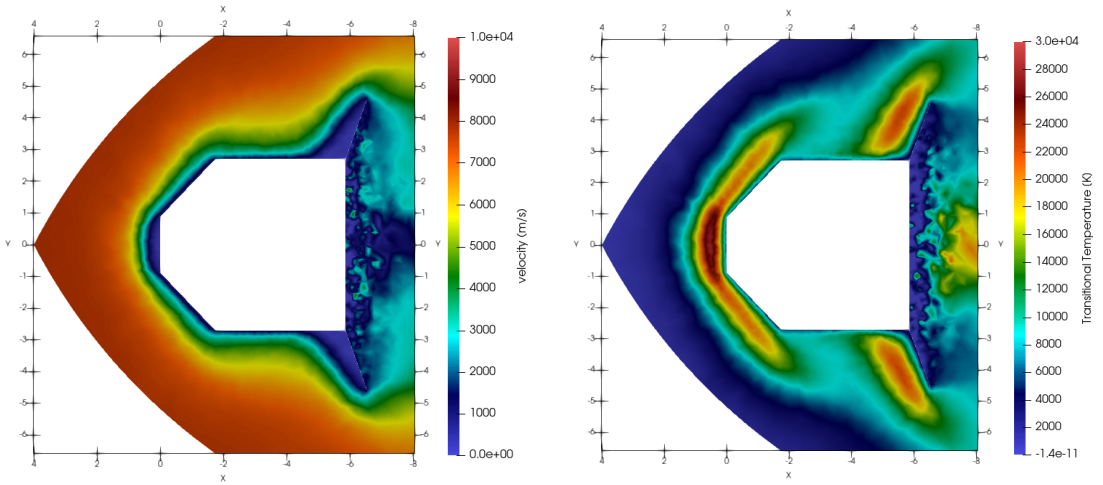

Figure 6.20: Flow field for the 70° configuration at 105 km and AoA 0°: velocity (left) and total temperature (right).

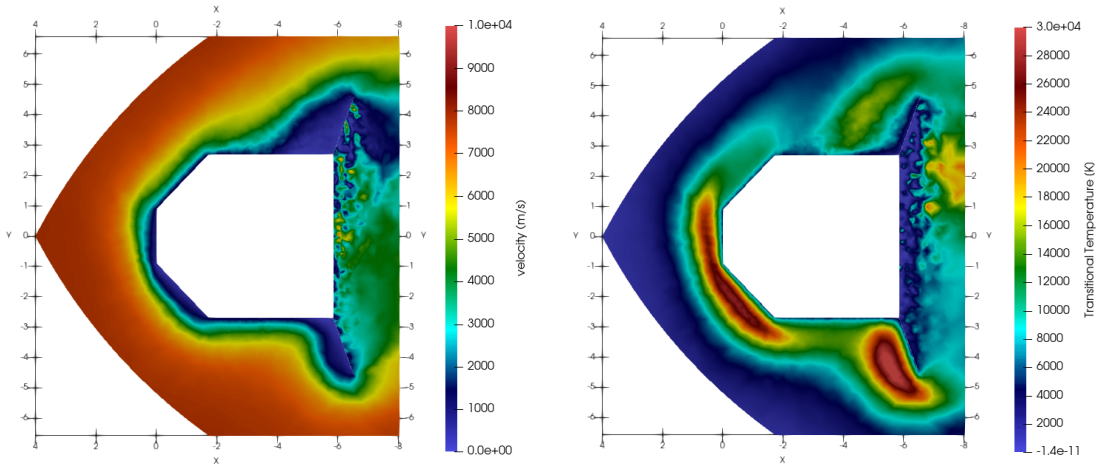

Figure 6.21: Flow field for the 70° configuration at AoA 30°: velocity (left) and total temperature (right).

It is relevant to analyze the flow characteristics at this altitude. Compare to the previous altitude, the distance between the shock and the capsule nose tends to

decrease slightly, as the denser air compresses the shock closer to the surface. The wake behind the capsule becomes more complex, and the velocity gradients around the DAS become steeper, increasing the shear stress on the surface. Simultaneously, both the kinematic and thermal boundary layers compress toward the structure. This effect, combined with the higher kinetic energy of the flow, results in elevated temperature peaks and increased wall heat flux compared to the 120 km altitude case. For further details, reference is made to Section 6.3.

The influence of the center of gravity position on the pitching moment coefficient C_{m_y} is investigated as a function of the angle of attack at $h = 105\,\text{km}$.

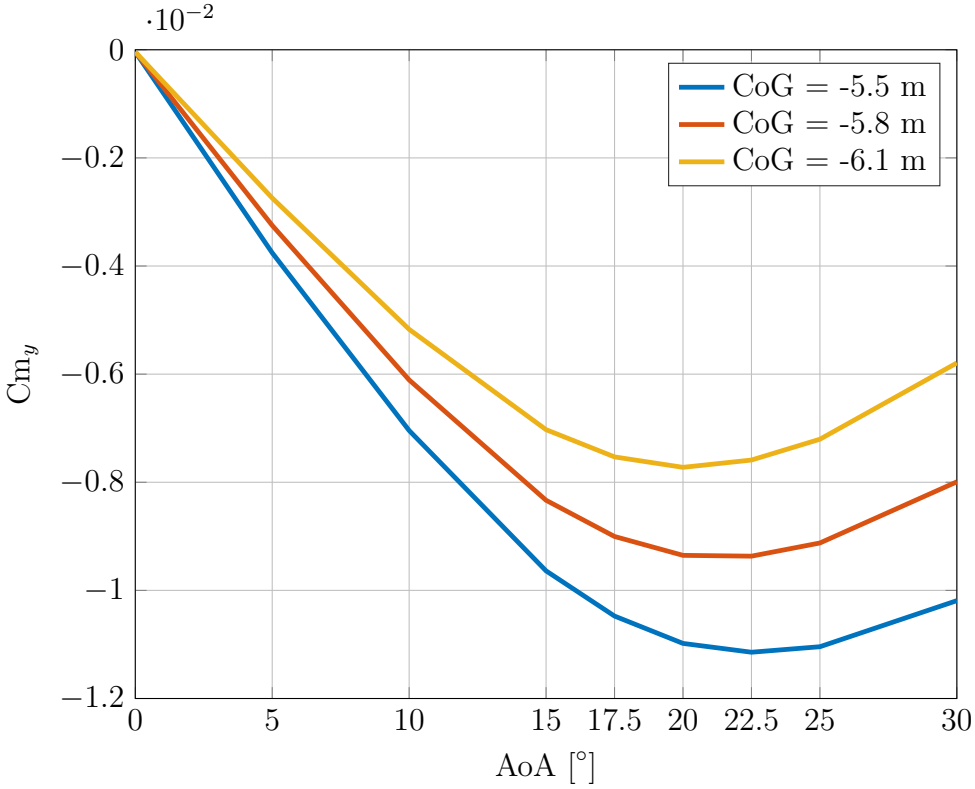

Figure 6.22: Trend of the moment coefficient Cm_y as a function of angle of attack for different center-of-gravity positions (105 km altitude, 70° opening angle).

The influence of the center of gravity position on C_{m_y} at $h = 105\,\text{km}$ is consistent with the behaviour observed at 120 km. Shifting the CoG downstream increases both the magnitude of C_{m_y} and the AoA range over which a restoring moment is present, with the effect on the moment magnitude being particularly pronounced.

Specifically, a 30 cm aftward displacement of the CoG, corresponding to approximately 5% of the nominal value, extends the stable AoA range across the full simulated range up to 45°, compared to approximately 40° for the nominal configuration. The peak restoring moment increases from -7.74×10^{-3} to -9.92×10^{-3}, representing an increase of approximately 28%, confirming the high sensitivity of the stability margin to CoG position. Conversely, a forward displacement of equal magnitude reduces the peak to -5.56×10^{-3} and restricts the stable range to approximately 32°, highlighting the asymmetric influence of CoG displacement on static stability.

In order to quantify the actual aerodynamic loads acting on the upper stage, a comparison of the moment coefficient as a function of the angle of attack between the two analyzed altitudes is presented below. This comparative analysis allows the assessment of load evolution from 120 km to 105 km, highlighting the system's sensitivity to the increase in atmospheric density along the re-entry trajectory.

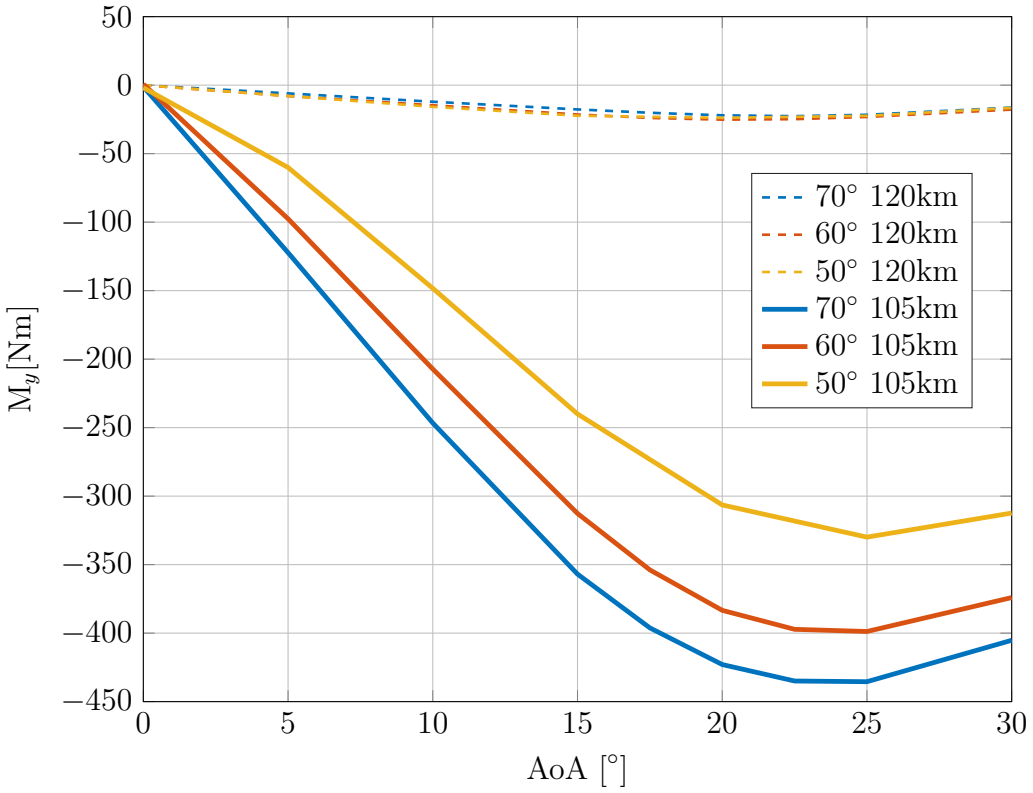

Figure 6.23: Trend of the moment M_0 as a function of angle of attack for the 50°, 60°, and 70° configurations at 120 km (dashed lines) and 105 km (solid lines).

The comparative analysis reported in Figure 6.23 clearly demonstrates that the aerodynamic moment M_y at $h = 105\,\text{km}$ is significantly larger in magnitude than the corresponding values at 120 km across all configurations and angles of attack. At AoA $= 22.5°$, the 70° configuration reaches a peak of approximately $-435\,\text{Nm}$ at 105 km, compared to $-22.6\,\text{Nm}$ at 120 km, representing an increase of approximately one order of magnitude. This amplification is a direct consequence of the higher atmospheric density encountered during descent, which increases the dynamic pressure and therefore the absolute aerodynamic loading on the vehicle, while the normalized coefficient C_{m_y} remains comparatively stable across altitudes. The ordering among configurations is preserved between the two altitudes, with the 70° opening angle consistently generating the largest restoring moment. To further investigate the evolution of these aerodynamic loads and validate the observed trend of increasing moment magnitude with decreasing altitude, the simulation campaign was extended to $h = 95\,\text{km}$.

6.2.1 Effect of the length of the DAS

Figure 6.24 presents the drag and lift coefficients as a function of AoA for the two panel length configurations at $h = 105\,\text{km}$.

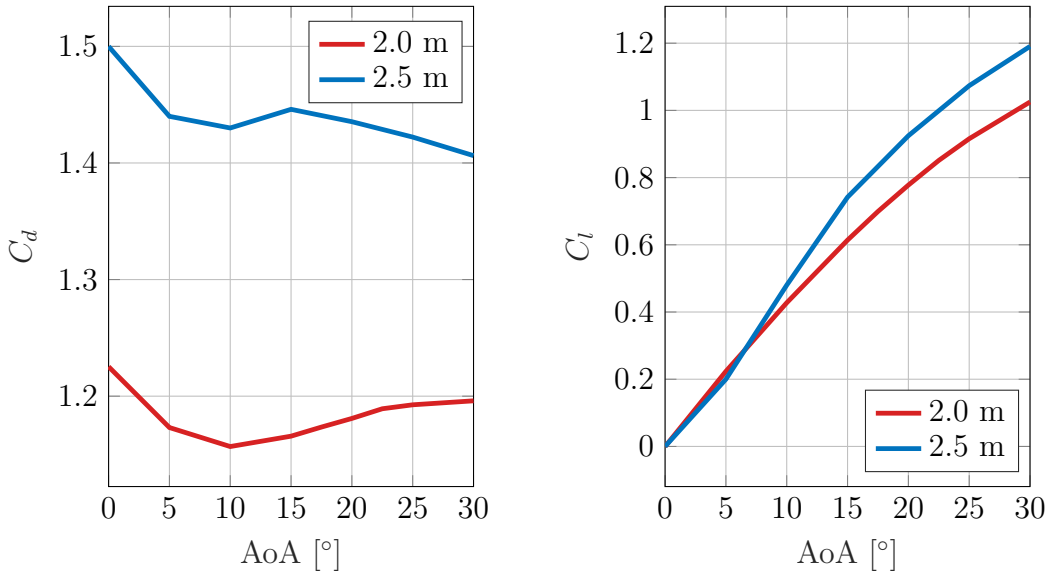

Figure 6.24: C_d(left) and C_l (right) as a function of AoA for the 60° opening angle configuration. Panel lengths 2.0 m and 2.5 m. $h = 105\,\text{km}$.

The drag coefficient $C_d$exhibits a non-monotonic behaviour for both configurations, decreasing from its maximum at 0° to a minimum near AoA = 10°, before

increasing again toward 30°. The 2.5 m configuration consistently yields higher $C_d$values across the full AoA range: at AoA = 0°, $C_d$is 1.225 for the 2.0 m panel and 1.500 for the 2.5 m panel, a relative difference of approximately 22%. This spread remains approximately constant throughout the AoA range, reducing slightly to approximately 18% at AoA = 30°. Compared to the results at 120 km, the absolute values of $C_d$are lower at 105 km for both configurations, reflecting the different flow regime and the increased role of the projected area normalisation at higher dynamic pressure. The lift coefficient C_l increases monotonically from zero for both configurations and shows a moderate sensitivity to panel length: at AoA = 30°, C_l reaches 1.025 for the 2.0 m configuration and 1.191 for the 2.5 m configuration, a relative difference of approximately 16%, consistent with the trend observed at 120 km.

Figure 6.25 presents the pitching moment M_y as a function of AoA for the two panel length configurations at $h = 105$ km.

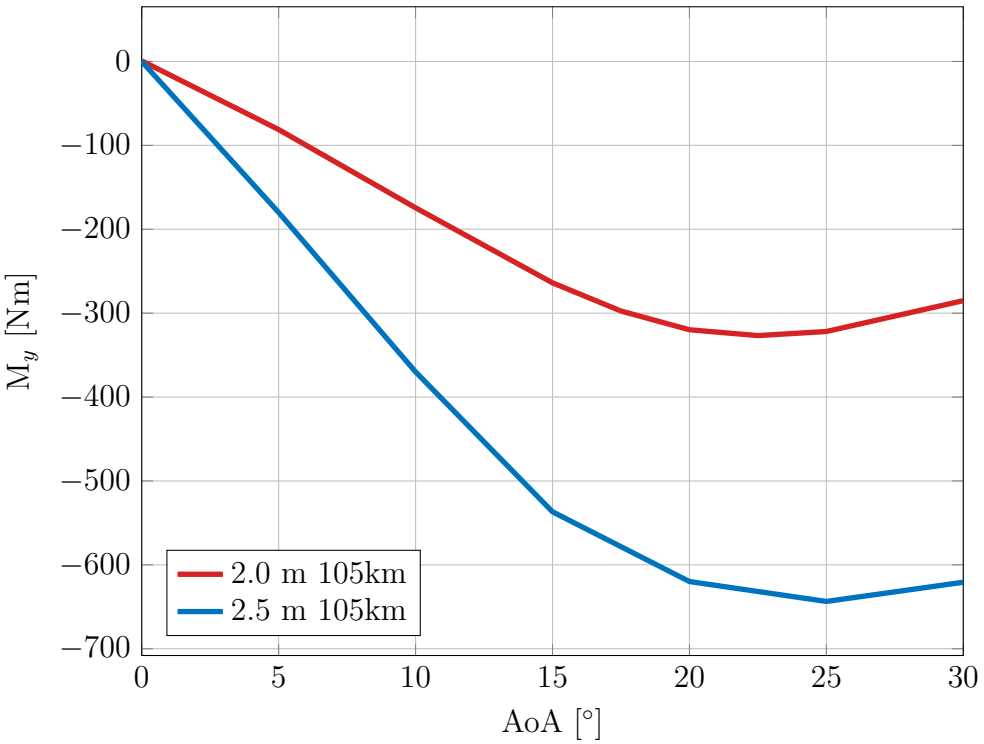

Figure 6.25: Pitching moment M vs. AoA at 105 km.

Consistent with the trend observed at 120 km, the 2.5 m configuration generates a substantially larger restoring moment across the full AoA range. At the peak, reached near AoA = 22.5°, M_y reaches −643.6 Nm for the 2.5 m panel compared to −326.8 Nm for the 2.0 m configuration, representing an increase of approximately 97%. The absolute values are approximately one order of magnitude larger than those observed at 120 km for both configurations, consistent with the significant increase in atmospheric density at this altitude. Both configurations exhibit moment saturation beyond AoA ≈ 22.5°–25°, with M_y recovering toward less negative values at higher incidence. As at 120 km, neither configuration reaches a trim point within the simulated AoA range, confirming that the vehicle remains in a restoring moment condition throughout the full range of angles of attack considered.

6.3 Simulations at Kn = 0.01

The simulation campaign was extended to $h = 95\,\text{km}$. At this altitude, the further increase in atmospheric density resulted in a significant computational load even for the BGK method, necessitating a strategic selection of simulation cases. Given the consistency of the trends observed at higher altitudes, the investigation was focused on the AoA range between 15° and 30°, where the aerodynamic curves exhibit a change in concavity and the flow behaviour is most relevant for stability analysis. The parametric study was further restricted to the 60° and 70° opening angle configurations, which exhibited the most favourable aerodynamic performance at 105 km. Figure 6.26 presents the dimensional drag and lift forces as a function of the angle of attack for the two selected configurations at $h = 95\,\text{km}$.

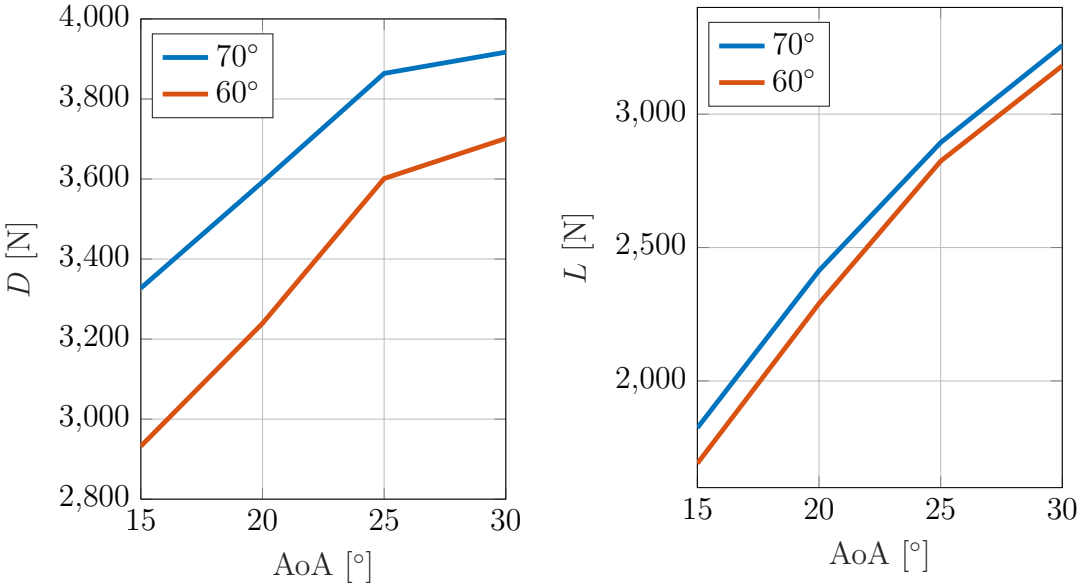

Figure 6.26: Drag D (left) and lift L (right) as a function of AoA for the 60° and 70° DAS opening angle configurations. $h = 95\,\text{km}$.

Both the drag force D and the lift force L increase monotonically with AoA across the simulated range, consistent with the trend observed at 105 km. At AoA = 15°, D takes values of approximately 2932 N (60°) and 3327 N (70°), a relative difference of approximately 13%. This spread reduces to approximately 6% at AoA = 30°, where D reaches 3701 N and 3917 N respectively. The absolute magnitudes are approximately one order of magnitude larger than those observed at 105 km, reflecting the significantly higher dynamic pressure at this altitude. The lift force L similarly increases with AoA, ranging from approximately 1691 N to 1824 N

at 15° and from 3181 N to 3257 N at 30°. The relative spread between the two configurations narrows considerably with increasing AoA, from approximately 8% at 15° to less than 3% at 30°, confirming that lateral force generation becomes increasingly insensitive to the opening angle at higher incidence angles.

The corresponding non-dimensionalised coefficients $C_d$and C_l, normalised by the projected reference area $A_{\text{proj}}(\alpha)$ as defined in Section 5.3.1, are shown in Figure 6.27.

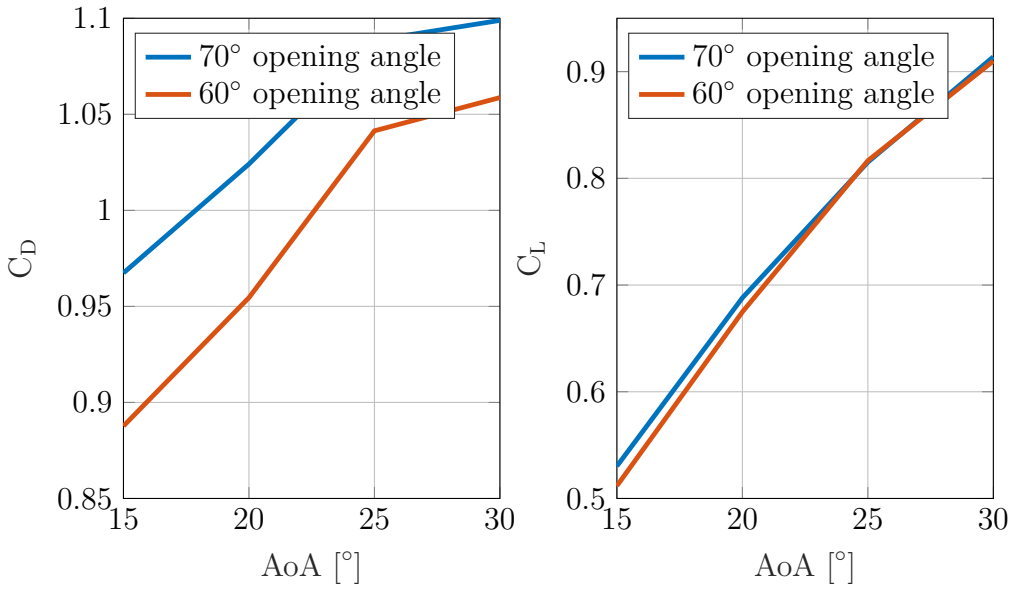

Figure 6.27: Trend of Cd (left) and Cl (right) as a function of angle of attack (AoA) for 70° and 60° opening angles at 95 km altitude.

The drag coefficient $C_d$increases monotonically with AoA for both configurations, in contrast to the non-monotonic behaviour observed at 105 km, indicating that at 95 km the growth of the actual drag force D with AoA dominates over the increase of A_{proj} throughout the entire simulated range. At AoA = 15°, $C_d$takes values of approximately 0.888 (60°) and 0.967 (70°), a relative spread of approximately 9%, which reduces to approximately 4% at AoA = 30°. The lift coefficient C_l increases monotonically from approximately 0.51–0.53 at 15° to approximately 0.91 at 30° for both configurations, with the two curves remaining nearly coincident across the full AoA range and differing by less than 1% at AoA = 30°, confirming that C_l is effectively independent of the opening angle at this altitude.

The pitching moment coefficient C_{m_y} as a function of AoA is presented in Figure 6.28.

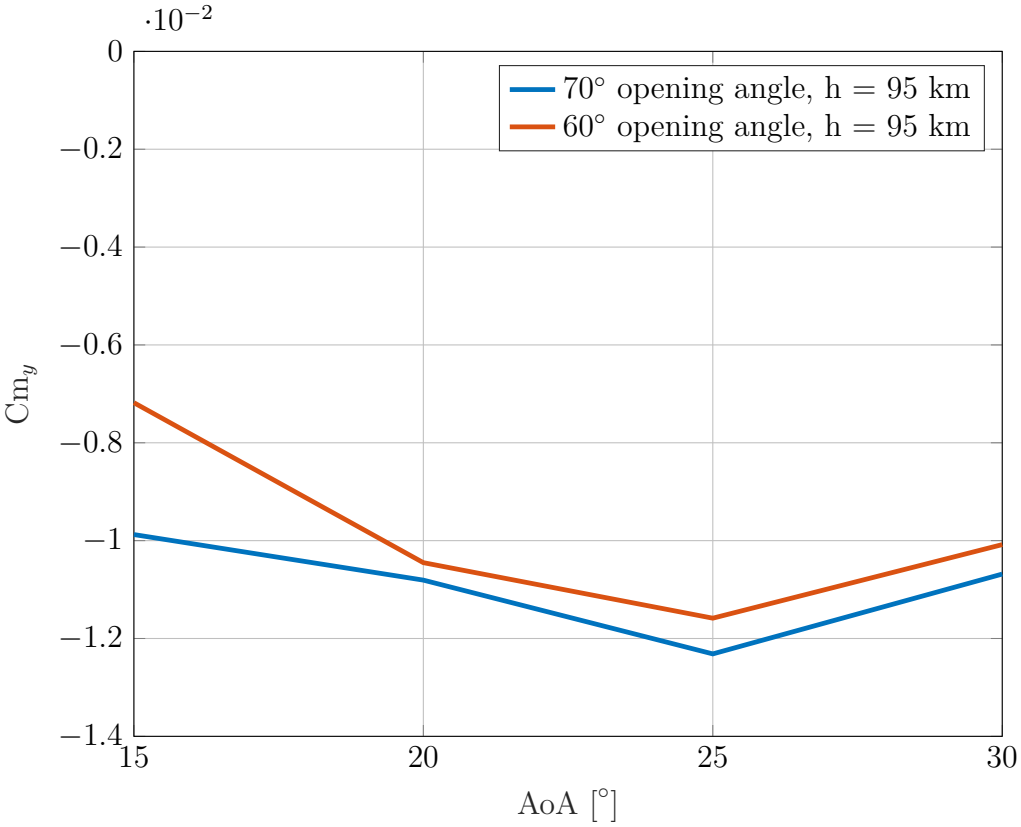

Figure 6.28: Trend of the moment coefficient Cm_y as a function of angle of attack (AoA) for different opening angle configurations at 95 km altitude.

Both configurations satisfy the static stability criteria throughout the simulated AoA range, with C_{m_y} remaining negative across the full range of 15°–30°. The influence of the opening angle on longitudinal stability remains present, with the 70° configuration consistently exhibiting a larger restoring moment magnitude. The peak of $|C_{m_y}|$ is reached near AoA = 25° for both configurations, after which moment saturation sets in. The analysis of the CoG sensitivity at this altitude confirms trends consistent with those observed at higher altitudes; the corresponding results are reported in Appendix A.4.

A comparative plot of the aerodynamic moment M_y across all investigated altitudes is presented in Figure 6.29, providing a quantitative basis for assessing the evolution of longitudinal static stability along the re-entry trajectory.

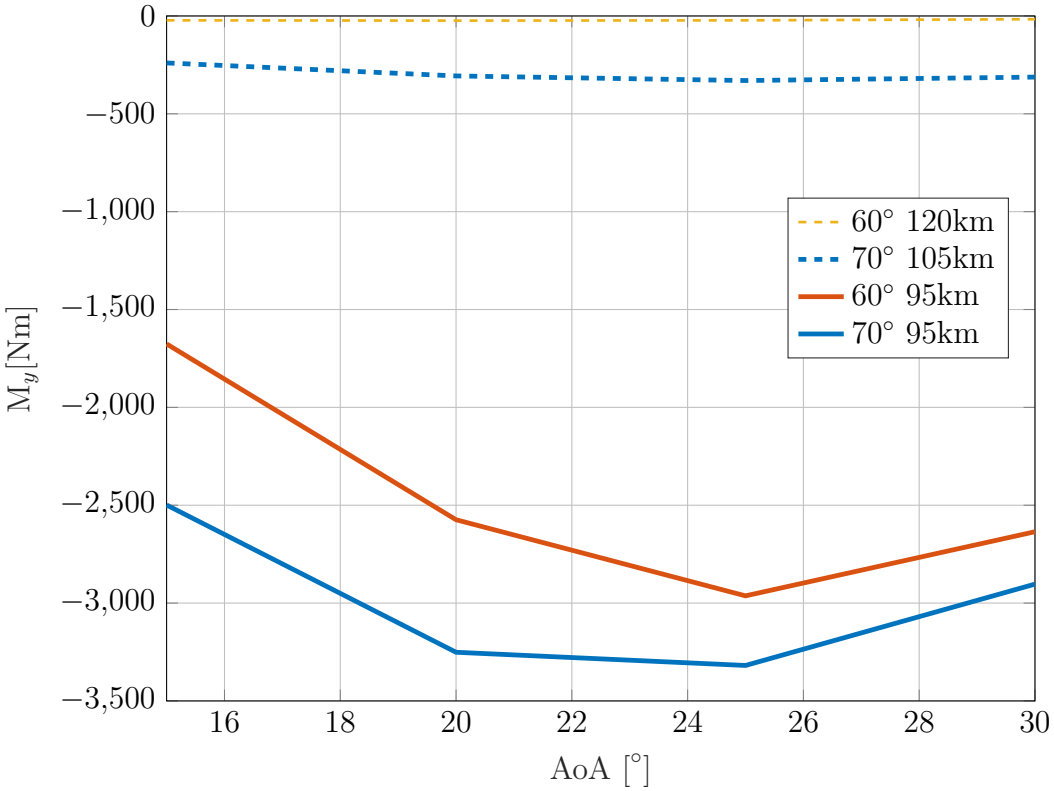

Figure 6.29: Moment M_0 as a function of angle of attack for the different configurations and altitudes.

The moment magnitudes at 95 km are substantially larger than those observed at higher altitudes, with peak values of approximately −3319 Nm (70°) and −2963 Nm (60°), compared to values on the order of tens of Nm at 120 km. This progressive amplification is consistent with the rapid increase in atmospheric density along the descent trajectory and is expected to continue at lower altitudes. The ordering among configurations is preserved across all altitudes, with the 70° opening angle consistently generating the largest restoring moment.

At this stage of the discussion, it is relevant to analyze the evolution of the aerodynamic coefficients with altitude to provide a concise overview of the system behaviour along the re-entry trajectory. The 60° opening angle configuration is selected as a representative case. Figure 6.30 shows $C_d$and C_l as functions of AoA for all three altitudes investigated.

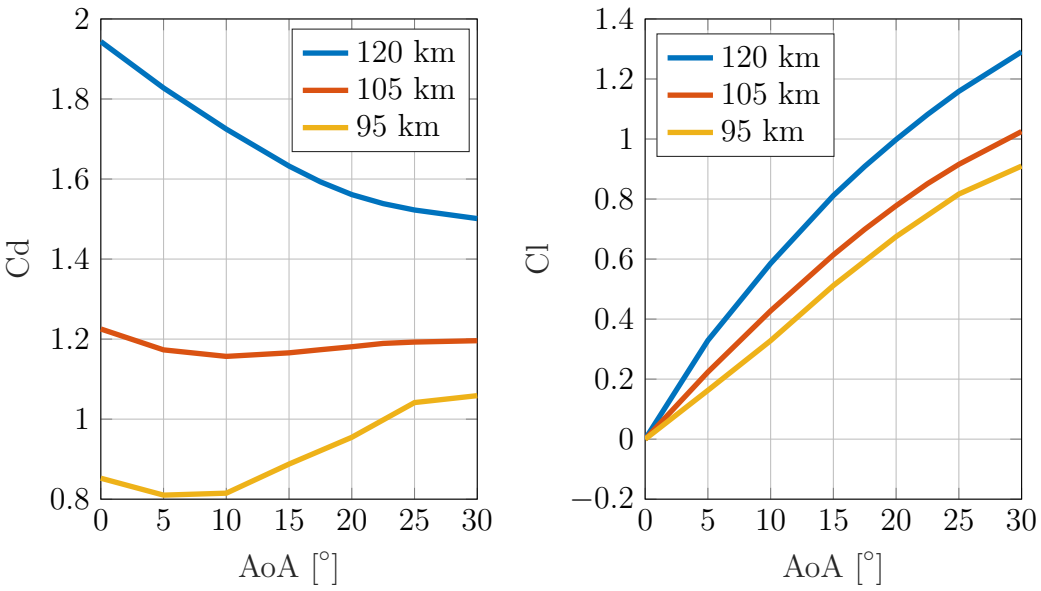

Figure 6.30: Trend of Cd (left) and Cl (right) of the 60° opening angle as a function of angle of attack (AoA) for different altitudes.

The evolution of $C_d$with altitude reflects the transition from the transitional flow regime toward continuum conditions. At 120 km, the high degree of gas rarefaction limits intermolecular collisions, resulting in a high momentum transfer per molecular impact and a corresponding $C_d \approx 1.9$. As the altitude decreases to 95 km, the increase in density and collision frequency promotes the formation of a well-defined detached shock layer, which deflects incoming molecules before direct surface impact and reduces the net momentum transfer. The macroscopic effect is a marked reduction in $C_d$to values approaching 0.85–1.06 across the simulated AoA range. The lift coefficient C_l, while continuing to increase monotonically with AoA at all altitudes, decreases progressively with decreasing altitude. This behaviour is attributable to the modification of the surface pressure distribution associated with the regime transition: as the shock layer consolidates and its stand-off distance decreases, the pressure asymmetry between the windward and leeward surfaces is reduced, lowering the effective lift-curve slope $C_{l_\alpha} = \partial C_l / \partial \alpha$. A visual comparison of the velocity fields at the three altitudes is presented in Figures 6.31–6.32–6.33 for the 60° opening angle configuration at AoA = 30°. A consistent trend is observed: as altitude decreases, the bow shock stand-off distance reduces and the shock structure becomes more compact and better defined. The angle of attack remains the primary driver of shock asymmetry, while altitude governs the proximity of the shock to the vehicle surface and the degree of flow compression.

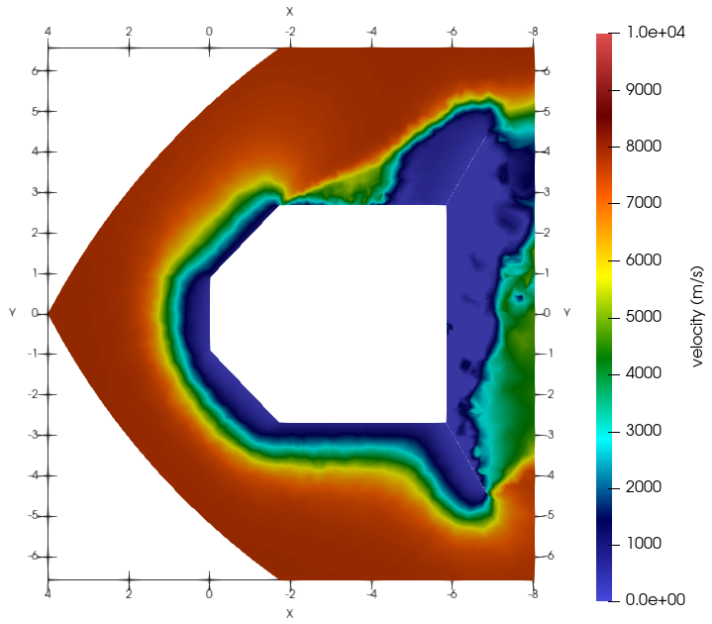

Figure 6.31: Velocity field at an altitude of 120 km (60° opening angle, AoA = 30°).

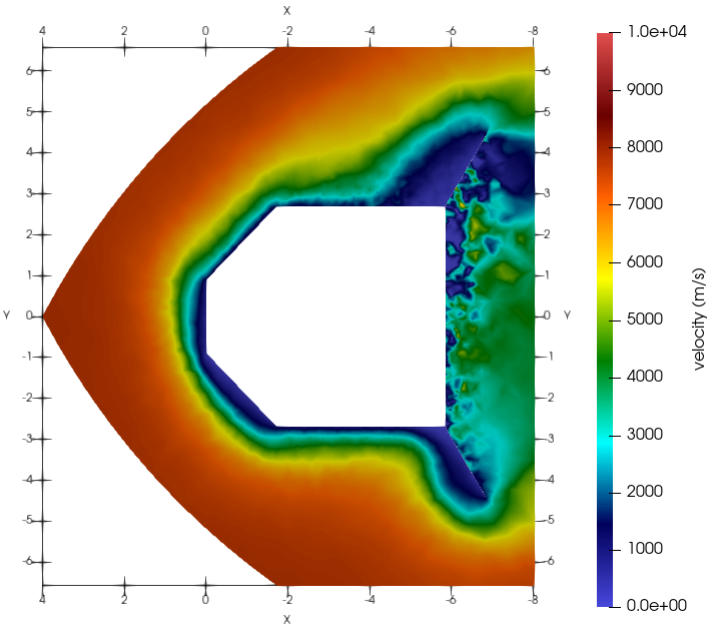

Figure 6.32: Velocity field at an altitude of 105 km (60° opening angle, AoA = 30°).

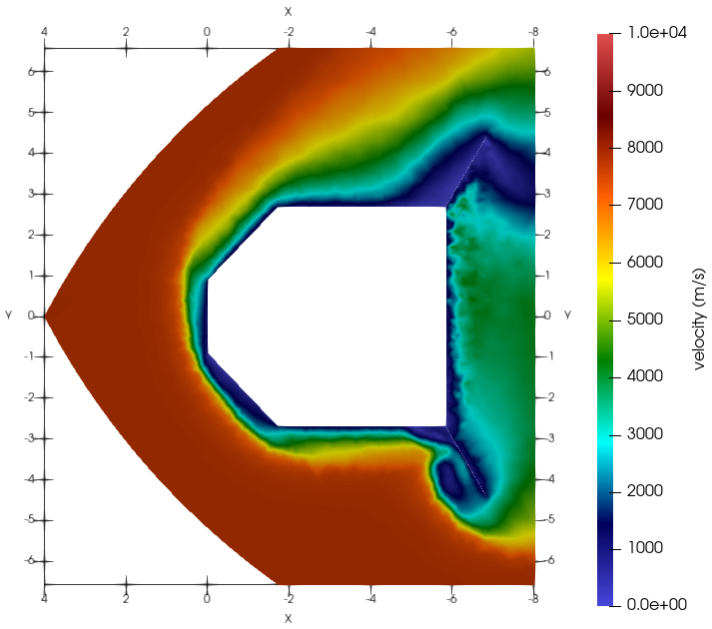

Figure 6.33: Velocity field at an altitude of 95 km (60° opening angle, AoA = 30°).

At 95 km, the more compact shock topology is directly responsible for the modifications in surface pressure distribution and the resulting variations in the global aerodynamic coefficients discussed above.

6.3.1 Effect of the Length of the DAS

Figure 6.34 presents the drag and lift coefficients as a function of AoA for the two panel length configurations at $h = 95$ km, over the simulated range of 15°–30°. The drag coefficient $C_d$increases monotonically with AoA for both configurations, reflecting the dominance of the actual force increase over the projected area growth at this altitude. The sensitivity of C_d to panel length is markedly reduced compared to the higher altitudes: at AoA = 15°, $C_d$is 0.888 for the 2.0 m panel and 1.000 for the 2.5 m panel, a relative difference of approximately 13%, which further reduces to approximately 1% at AoA = 30°, where the two curves are nearly coincident. This convergence suggests that at 95 km the aerodynamic loading becomes increasingly governed by the angle of attack rather than the DAS geometry. The lift coefficient C_l increases monotonically for both configurations and shows similarly reduced sensitivity to panel length: at AoA = 30°, C_l reaches 0.910 for the 2.0 m panel and 0.888 for the 2.5 m panel, a difference of approximately 2%, with the two curves remaining nearly coincident across the full AoA range.

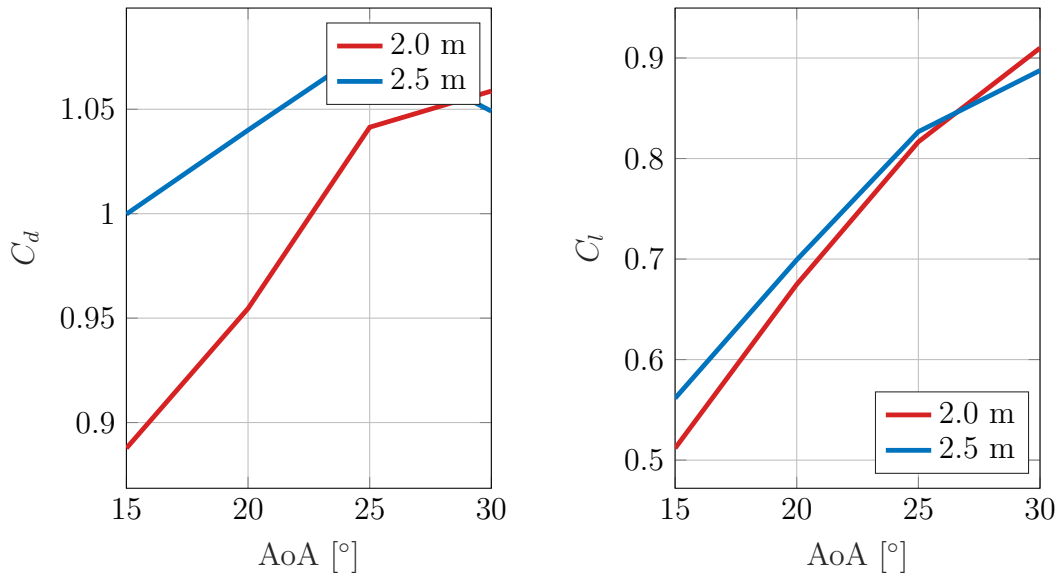

Figure 6.34: C_d(left) and C_l (right) as a function of AoA for the 60° opening angle configuration. Panel lengths 2.0 m and 2.5 m. $h = 95$ km.

Figure 6.35 presents the pitching moment coefficient C_{m_y} as a function of AoA for the two panel length configurations at $h = 95$ km.

Both configurations satisfy the static stability criteria throughout the simulated AoA range, with C_{m_y} remaining negative and $C_{m_\alpha} < 0$ up to the respective peak values. A notable difference with respect to the higher altitudes is observed in the low-AoA behaviour: the 2.0 m configuration exhibits a near-zero C_{m_y} up to approximately 5°, with the restoring moment becoming significant only beyond 10°, whereas the 2.5 m configuration develops a restoring moment already from low angles of attack. At the peak, reached near AoA = 25°, the 2.5 m configuration yields $C_{m_y} = -1.315 \times 10^{-2}$, compared to -1.159×10^{-2} for the 2.0 m panel, a relative increase of approximately 13%. This spread is considerably smaller than the differences observed at 120 km and 105 km, consistent with the convergence of $C_d$and C_l noted above, and confirms that the influence of panel length on the normalized aerodynamic coefficients diminishes as atmospheric density increases. Both configurations exhibit moment saturation beyond AoA $\approx 25°$.

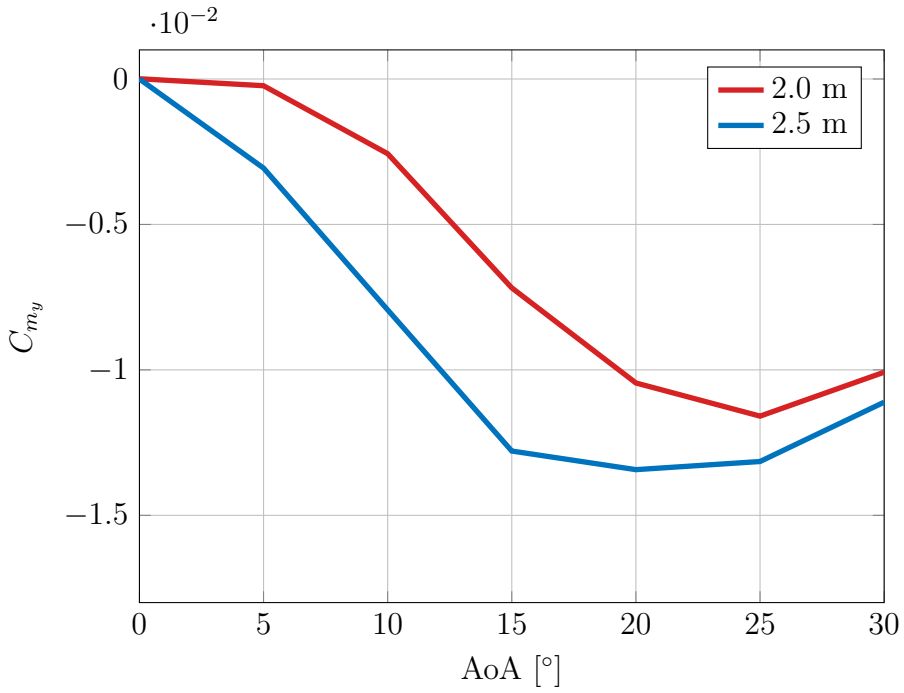

Figure 6.35: C_{m_y} as a function of AoA for the 60° opening angle configuration. Panel lengths 2.0 m and 2.5 m. $h = 95\,\text{km}$.

6.4 Forced Rotation

Forced spin stabilization represents a potential complement to the passive aerodynamic stability provided by the DAS, particularly in flight regimes where the aerodynamic restoring moment alone may be insufficient to maintain a controlled attitude. This section discusses whether the addition of a forced spin rate ω about the longitudinal axis would be beneficial for the ULPM configuration analyzed in this work.

The gyroscopic momentum generated by spin stabilization is proportional to the axial moment of inertia I_{xx} and the angular velocity ω. For the present configuration, the following inertial properties are assumed: $I_{xx} = 30{,}000\,\text{kg}\,\text{m}^2$ and $I_{yy} = I_{zz} = 50{,}000\,\text{kg}\,\text{m}^2$. These values are assumptions, as the precise mass distribution of the expended ULPM is not available within the scope of this work. It is noted that $I_{xx} < I_{yy}$, which is characteristic of an elongated body and implies that the vehicle is a *prolate* spinner. This configuration is known to be dynamically unstable under energy dissipation, as any perturbation tends to drive the vehicle toward a flat spin about the axis of maximum inertia. This represents an important

argument against the use of forced spin stabilization for this vehicle class.
A further argument against the addition of spin comes from the aerodynamic stability already provided by the DAS. The simulation results presented in the preceding sections demonstrate that all configurations satisfying the three static stability criteria, existence of a restoring moment, negative C_{m_α}, and sufficient static margin, do so passively across the full altitude range investigated, without requiring any active attitude control. The DAS geometry alone is sufficient to establish a positive static margin and generate a restoring pitching moment throughout the re-entry corridor from 120 km to 95 km. In this context, the addition of a forced spin would not address the root cause of any residual instability, but would instead introduce additional complexity in terms of the spin-up mechanism, structural loads on the DAS panels due to centrifugal effects, and potential interference with onboard systems sensitive to rotation.

On the other hand, spin stabilization could in principle provide resistance to transient perturbations not captured by the static stability analysis, such as asymmetric deployment of the DAS panels or impulsive disturbances during stage separation. The gyroscopic moment generated by the assumed I_{xx} would resist such perturbations, maintaining the vehicle attitude until the aerodynamic restoring moment re-establishes the trim condition. However, given the prolate nature of the vehicle and the availability of passive aerodynamic stability across the full re-entry corridor, the benefit of spin stabilization appears marginal relative to its implementation cost.

In conclusion, the addition of forced spin stabilization is not recommended as a primary stability strategy for the ULPM in a Design not to Demise context. The passive DAS concept provides sufficient static stability throughout the investigated altitude range, and the inertial properties of the expended upper stage make spin stabilization potentially counterproductive due to the prolate spinner instability. Should residual dynamic instabilities be identified in future unsteady simulations, a limited spin rate could be considered as a supplementary measure, provided that a dedicated structural assessment of the centrifugal loads on the DAS panels is performed and the spin-up mechanism is shown to be feasible within the mass and volume budget of the stage.

Chapter 7

Conclusions and Future Work

The aerodynamic stability of an upper-stage module equipped with a Deployable Aerodynamic Stabilizer (DAS) during atmospheric re-entry was investigated across the transitional and near-continuum flow regimes, spanning altitudes from 120 km to 95 km. The analysis aimed at identifying which design parameters promote longitudinal static stability during re-entry of an orbital upper stage, and at assessing the feasibility of a passive stabilization approach in the context of the Design not to Demise philosophy. All configurations examined exhibit a restoring pitching moment over a range of angles of attack and a consistently negative C_{m_y} within that range, without requiring active attitude control. The basic criteria for longitudinal static stability are therefore met across all simulations within a bounded angle-of-attack range. Whether this is sufficient to ensure controlled re-entry in practice requires further substantiation, in particular through comparison with mission-level stability requirements and dynamic stability analysis, as outlined in the following section. Nevertheless, these results constitute a necessary condition for the feasibility of a Design not to Demise approach for large expendable upper stages, and confirm that passive stabilization via a DAS is a viable avenue for further investigation. Both C_{m_y} and the peak restoring moment are already present at 120 km, confirming that the transitional regime cannot be excluded from a complete stability assessment. Among the geometric and mass parameters investigated, the DAS panel length L_4 emerges as the most influential design variable, followed by the centre of gravity position, while the DAS opening angle exerts a moderate but non-negligible influence. Increasing the panel length from 2.0 m to 2.5 m produces an increase in the peak restoring moment of approximately 113 % at 120 km and 97 % at 105 km, while extending the stable angle-of-attack range by approximately 11 % at both altitudes. At 95 km this effect reduces to approximately 57 % on

the peak moment. Across the opening angle range investigated (30°–70°), the spread in peak $|C_{m_y}|$ is of the order of 20–25 % at a given altitude, with larger opening angles consistently yielding greater restoring moments; this ordering is preserved across all three altitudes. The longitudinal position of the centre of gravity (CoG) is identified as a highly sensitive design parameter. A displacement of only $\pm 0.3\,\mathrm{m}$ ($\pm 5\,\%$ of the nominal CoG position) produces changes of up to 28 % in the peak restoring moment at 120 km, with comparable sensitivity observed at 105 km and 95 km. A forward CoG position, closer to the nose, increases the magnitude of the restoring moment at any given angle of attack, and is therefore beneficial for stability. However, the installation of the DAS system itself displaces mass toward the aft end of the stage, shifting the CoG in a direction that reduces the restoring moment. This represents an inherent trade-off in the design of the DAS concept: the same system that provides aerodynamic stabilization partially offsets its own effectiveness through the associated mass displacement. The mass budget of the deployable system must therefore be treated as an integral part of the stability assessment from the earliest design stages, rather than as an independent add-on. Regarding the feasibility of the Design not to Demise approach, the present results provide a necessary but not sufficient basis for a definitive assessment. The static stability criteria are satisfied over a bounded angle-of-attack range for all configurations across all three altitudes, which constitutes a prerequisite for controlled re-entry. The directions required to complete this assessment are outlined in the following section.

7.1 Future Work

The present campaign identifies several directions for future investigation. The most immediate priority is the extension of the simulation campaign to lower altitudes, toward the peak aerodynamic heating region at approximately 60 km, where the flow reaches full continuum conditions and both aerodynamic loads and thermal fluxes increase substantially. This would allow verification of whether the stability trends identified in the transitional regime persist into the continuum, and whether any configuration transitions from stable to unstable behavior where the dynamic pressure is significantly higher. A systematic evaluation of larger DAS geometries, both in terms of panel length beyond 2.5 m and opening angles beyond 70°, would help establish the upper bound of achievable restoring moment for this vehicle class, and identify whether a saturation regime exists beyond which further geometric scaling yields diminishing stability returns. The quantification of the static margin through the computation of the Centre of Pressure position as a function of angle of attack and altitude is identified as a critical next step, as it would allow a formal assessment of all three stability criteria and provide a basis for comparison with mission-level stability requirements. The extension to unsteady simulations for dynamic stability characterization is a further necessary step, as the present static analysis cannot capture oscillatory behavior, limit cycles, or the damping properties of the configuration during attitude perturbations. Dynamic instabilities, which are known to occur in the transonic regime for blunt-body re-entry vehicles, may also be present in the transitional regime and should be investigated. Finally, an integrated aerothermal and structural assessment of the DAS panels under re-entry loads would be required to evaluate the thermal protection requirements and the mechanical feasibility of the deployable system, closing the loop between aerodynamic performance and structural survivability that is at the core of the Design not to Demise concept.

Bibliography

[1] J. McDowell. *General Catalog of Artificial Space Objects Release 1.7.3*. Tech. rep. Accessed: September 23, 2025. 2025 (cit. on p. 1).

[2] B. Fritsche, H. Klinkrad, A. Kashkovsky, and E. Grinberg. «Spacecraft Disintegration During Uncontrolled Atmospheric Re-entry». In: *Acta Astronautica* 47.2-9 (2000), pp. 513–522 (cit. on p. 1).

[3] Carmen Pardini and Luciano Anselmo. «The kinetic casualty risk of uncontrolled re-entries before and after the transition to small satellites and mega-constellations». In: *Journal of Space Safety Engineering* 9.3 (2022), pp. 414–426. DOI: 10.1016/j.jsse.2022.04.003 (cit. on p. 1).

[4] European Space Agency (ESA). *ESA Space Debris Mitigation Compliance Verification Guidelines*. Technical Report. European Space Agency (ESA), 2025 (cit. on p. 1).

[5] European Space Agency (ESA). *Reentry and Collision Avoidance – Space Debris*. https://www.esa.int/Space_Safety/Space_Debris/Reentry_and_collision_avoidance. Accessed: September 23, 2025. 2025 (cit. on p. 1).

[6] P. M. Waswa and J. A. Hoffman. «Illustrative NASA Low Earth Orbit Spacecraft Subsystems Design-for-Demise Trade-offs, Analyses and Limitations». In: *International Journal of Design Engineering* 5.1 (2012), pp. 21–40 (cit. on p. 1).

[7] C. Pardini and L. Anselmo. «On the Need to Assess and Mitigate the Risk from Uncontrolled Re-entries of Artificial Space Objects in View of the Current and Future Developments in Space Activities». In: *Acta Astronautica* 219 (2024), pp. 662–669 (cit. on pp. 2, 5, 6).

[8] J. S. Fischer, S. Fasoulas, C. Brun-Buisson, and E. Del Olmo. «Comparison Study on the Environmental Impact of Different Launcher Architectures». In: *74th International Astronautical Congress (IAC)*. Vol. 2023. IAC-23, D2, 9-D6.2,3, X78935. Baku, Azerbaijan, 2023 (cit. on p. 2).

[9] J.-S. Fischer and S. Fasoulas. «Assessment of Launch and Re-entry Emissions of Space Transportation Systems and Their Environmental Impact». In: *International Astronautical Federation (IAF)*. 2024, pp. 756–766 (cit. on p. 2).

[10] S. Förste, L. E. Yousfi, F. Turco, C. Traub, J. S. Fischer, and S. Fasoulas. «A Comprehensive Assessment of Rocket Body Related Space Debris and Discussion of Suitable Means of Risk Reduction». In: *75th International Astronautical Congress* (cit. on p. 3).

[11] E. Mooij. *Re-entry Systems*. Springer Nature, 2024 (cit. on pp. 5–7, 19, 22).

[12] European Space Agency. *ESA Space Environment Report 2025*. Tech. rep. European Space Agency, 2025. URL: https://www.esa.int/Space_Safety/Space_Debris (cit. on p. 5).

[13] S. Förste, L. El Yousfi, J.-S. Fischer, F. Turco, C. Traub, and S. Fasoulas. «A Comprehensive Assessment of Rocket Body Related Space Debris and Discussion of Suitable Means of Risk Reduction». In: *Acta Astronautica* 230 (2025), pp. 54–64 (cit. on pp. 7, 8).

[14] S. Heinrich, A. Humbert, and R. Amiel. «GREENSPACE: Recovery & Reusability Scenarios for Launcher Industry». In: *2018 SpaceOps Conference*. Vol. 2018. Marseille, France, 2018 (cit. on p. 7).

[15] Patrik Kärräng, Tobias Lips, and Toshiya Hanada. «Demisability of Critical Spacecraft Components During Atmospheric Re-entry». In: *Journal of Space Safety Engineering* 6.3 (2019), pp. 181–189. DOI: 10.1016/j.jsse.2019.09.001 (cit. on p. 7).

[16] Patrik Kärräng, Tobias Lips, and Toshiya Hanada. «Design for Containment Techniques to Reduce Spacecraft Re-Entry Footprint». In: *2nd International Conference on Flight Vehicles, Aerothermodynamics and Re-entry Missions & Engineering (FAR)*. 2022. URL: https://elib.dlr.de/191479/ (cit. on p. 8).

[17] José P. Ferreira, Robert D. Braun, Prasun N. Desai, and Joseph Wang. «Potential Ozone Depletion From Satellite Demise During Atmospheric Reentry in the Era of Mega-Constellations». In: *Geophysical Research Letters* 51 (2024). DOI: 10.1029/2024GL109280 (cit. on p. 8).

[18] Christopher M. Maloney, Robert W. Portmann, Martin N. Ross, and Karen H. Rosenlof. «Investigating the Potential Atmospheric Accumulation and Radiative Impact of the Coming Increase in Satellite Reentry Frequency». In: *Journal of Geophysical Research: Atmospheres* (2025). DOI: 10.1029/2024JD042141 (cit. on p. 8).

[19] European Space Agency (ESA). *ESA's Re-Entry Prediction*. https://reentry.esoc.esa.int/home/recovereddebris (cit. on p. 8).

[20] SpaceX. *Falcon 9 User's Guide*. 2021. URL: https://www.spacex.com/media/falcon-9-users-guide-2021-09.pdf (cit. on p. 8).

[21] European Space Agency. *Ariane 6 — Europe's New Ariane 6 Rocket Powers into Space*. 2024. URL: https://www.esa.int/Enabling_Support/Space_Transportation/Ariane/Europe_s_new_Ariane_6_rocket_powers_into_space (cit. on p. 8).

[22] John M. DiNonno and Neil Cheatwood. «Low-Earth Orbit Flight Test of an Inflatable Decelerator (LOFTID) Mission Overview and Science Return». In: *AIAA SciTech Forum and Exposition*. Technical overview of HIAD performance and re-entry aerodynamics. Orlando, FL, USA: American Institute of Aeronautics and Astronautics, 2024 (cit. on p. 9).

[23] G. Guidotti et al. «The EFESTO Project: Advanced European Re-Entry System Based on Inflatable Heat Shield». In: (2022) (cit. on p. 9).

[24] Alan M. Cassell, Brandon Smith, Paul Wercinski, Shakib Ghassemieh, Ken Hibbard, Adam Nelessen, and James Cutts. *ADEPT: A Mechanically Deployable Re-Entry Vehicle System Enabling Interplanetary CubeSat and Small Satellite Missions*. Technical Report 20240000167. NASA Ames Research Center, 2024. URL: https://ntrs.nasa.gov/citations/20240000167 (cit. on p. 9).

[25] Stefano Mungiguerra, Gennaro Zuppardi, and Raffaele Savino. «Rarefied Aerodynamics of a Deployable Re-entry Capsule». In: *Aerospace Science and Technology* 69 (2017), pp. 395–403. DOI: 10.1016/j.ast.2017.07.007 (cit. on p. 9).

[26] Kajetan Weinmann. «Aerothermal and Aerodynamic Characterization for Deployable Recovery Concepts for Orbital Rocket Stages». Master's Thesis. Stuttgart, Germany: Universität Stuttgart, Institut für Raumfahrtsysteme, Jan. 2026 (cit. on pp. 11, 43, 52).

[27] Domenic D'Ambrosio. *Slides del corso di Aerotermodinamica Ipersonica*. Torino, Lecture Notes. 2024 (cit. on p. 13).

[28] R. A. Minzner, C. A. Reber, L. G. Jacchia, F. T. Huang, A. E. Cole, A. J. Kantor, T. J. Keneshea, S. P. Zimmerman, and J. M. Forbes. *Defining Constants, Equations, and Abbreviated Tables of the 1975 U.S. Standard Atmosphere*. NASA Technical Report (NASA TR R-459). National Aeronautics and Space Administration, 1976 (cit. on pp. 13, 14).

[29] Hsue-Shen Tsien. «Superaerodynamics, Mechanics of Rarefied Gases». In: *Journal of the Aeronautical Sciences* 13.12 (1946), pp. 653–664 (cit. on pp. 15, 17, 18).

[30] R. A. Minzner, C. A. Reber, O. K. Moe, A. O. Nier, G. R. Swenson, S. P. Zimmerman, and J. M. Forbes. *The 1976 Standard Atmosphere Above 86-km Altitude: Recommendations of Task Group II to COESA*. NASA Special Publication NASA-SP-398. National Aeronautics and Space Administration, 1976. URL: https://ntrs.nasa.gov/api/citations/19770003812/downloads/19770003812.pdf (cit. on p. 16).

[31] Umberto Maria Caracciolo. *Analisi aerotermodinamica di velivoli ipersonici: approfondimento su una particolare categoria di veicoli: "lo scramjet"*. Bachelor/Master Dissertation. Selinus University, Faculty of Engineering & Technology, 2023. URL: https://www.uniselinus.education/sites/default/files/2023-05/Umberto%20Maria%20Caracciolo.pdf (cit. on p. 16).

[32] NASA STEM Team. *What Is Supersonic Flight? (Grades 5–8)*. 2009. URL: https://www.nasa.gov/learning-resources/for-kids-and-students/what-is-supersonic-flight-grades-5-8/ (cit. on p. 16).

[33] Spartan College of Aeronautics and Technology. *From Subsonic to Hypersonic Flow: Navigating the Speed Regimes of Aviation*. 2023. URL: https://www.spartan.edu/news/from-subsonic-to-hypersonic-flow-navigating-the-speed-regimes-of-aviation/ (cit. on p. 16).

[34] Xiang Ren, Junya Yuan, Bijiao He, Mingxing Zhang, and Guobiao Cai. «Grid criteria for numerical simulation of hypersonic aerothermodynamics in transition regime». In: *Journal of Fluid Mechanics* 881 (2019), pp. 585–601. DOI: 10.1017/jfm.2019.756 (cit. on p. 16).

[35] George Karniadakis, Ali Beskok, and Narayan Aluru. *Microflows and Nanoflows: Fundamentals and Simulation*. New York: Springer, 2005 (cit. on p. 17).

[36] Iliya Milman. *An Investigation of the Supersonic Blunt-Body Problem*. Research Project / Report. Technion – Israel Institute of Technology, Faculty of Aerospace Engineering, 2022 (cit. on pp. 18, 19).

[37] John D. Anderson. *Hypersonic and High Temperature Gas Dynamics*. 2nd. AIAA Education Series, 2006. ISBN: 978-1-56347-780-5 (cit. on pp. 19, 20).

[38] Embry-Riddle Aeronautical University. *Hypersonic Flight Vehicles*. 2025. URL: https://eaglepubs.erau.edu/introductiontoaerospaceflightvehicles/chapter/hypersonic-flight-vehicles/ (cit. on p. 20).

[39] G. Herdrich and A. S. Pagan. *Wiedereintrittstechnologie – Reentry Technology*. Lecture slides, Institute of Space Systems, University of Stuttgart. 2023/2024 (cit. on p. 21).

[40] A. Guidi. «Re-entry Motion of an Axisymmetric Vehicle and Its Analysis Based on Flight Simulation». In: *Proceedings of the 23rd International Congress of the Aeronautical Sciences (ICAS 2002)*. International Council of the Aeronautical Sciences. 2002 (cit. on p. 22).

[41] Juan R. Cruz. *Flight Mechanics Lecture Notes*. Tech. rep. NASA Langley Research Center, Atmospheric Flight and Entry Systems Branch. URL: https://bigidea.nianet.org/wp-content/uploads/2015/10/%20Flight-Mechanics-Lecture-Notes-V6.pdf (cit. on p. 22).

[42] P. Noeding and R. Molina. «Aero(thermo)dynamic CFD Analyses of the PARES Re-Entry Capsule Shape in Comparison to Recent Test Results». In: *Proceedings of the 1st CEAS European Air and Space Conference*. Council of European Aerospace Societies. 2007 (cit. on p. 23).

[43] Cole D. Kazemba, Robert D. Braun, Mark Schoenenberger, and Ian G. Clark. *Dynamic Stability Analysis of Blunt Body Entry Vehicles Using Time-Lagged Aftbody Pitching Moments*. NASA Technical Report (ARC-E-DAA-TN11849). National Aeronautics and Space Administration, Ames Research Center, 2013 (cit. on p. 23).

[44] Valerio Carandente, Gennaro Zuppardi, and Raffaele Savino. «Aerothermodynamic and stability analyses of a deployable re-entry capsule». In: *Acta Astronautica* 93 (2014), pp. 291–303. DOI: 10.1016/j.actaastro.2013.07.030 (cit. on p. 24).

[45] R. Belgi. «Design Analysis of Deployable Elements for the Return of Orbital Rocket Bodies». Master's Thesis. Institute of Space Systems, University of Stuttgart, 2023/2024 (cit. on p. 24).

[46] Susumu Teramoto, Kojiro Hiraki, and Kozo Fujii. «Numerical Analysis of Dynamic Stability of a Reentry Capsule at Transonic Speeds». In: *AIAA Journal* 39.4 (2001), pp. 646–653. DOI: 10.2514/2.1355 (cit. on p. 26).

[47] Cole D. Kazemba et al. «Survey of Blunt Body Dynamic Stability in Supersonic Flow». In: *AIAA Paper*. American Institute of Aeronautics and Astronautics, 2012 (cit. on p. 26).

[48] Vladimir S. Aslanov and Dmitry A. Sizov. «Large Debris Removal: Using Features of Attitude Motion for Load Factor Regulation during Re-Entry». In: *Aerospace* 11.9 (2024), p. 786. DOI: 10.3390/aerospace11090786 (cit. on pp. 27, 28).

[49] V. S. Aslanov and A. V. Doroshin. «Stabilization of a Reentry Vehicle by a Partial Spin-up during Uncontrolled Descent». In: *Cosmic Research* 40.2 (2002), pp. 178–185 (cit. on p. 27).

[50] Behrad Vatankhahghadim. *Spin Stabilization*. Lecture Notes, Lecture 13. AER506: Spacecraft Dynamics and Control, University of Toronto. 2019 (cit. on p. 28).

[51] Yazhong Jiang, Yuxing Ling, and Shikang Zhang. «Investigation of the Inverse Magnus Effect on a Rotating Sphere in Hypersonic Rarefied Flow». In: *Applied Sciences* 14.3 (2024), p. 1042. DOI: 10.3390/app14031042 (cit. on p. 29).

[52] Ashley M. Korzun, Brian R. Hollis, Adam J. Wise, Derek S. Liechty, Christopher D. Karlgaard, and Rohan G. Deshmukh. «Aerodynamic Performance of the Low-Earth Orbit Flight Test of an Inflatable Decelerator (LOFTID) Technology Demonstration Mission». In: *AIAA 2024 SciTech Forum*. American Institute of Aeronautics and Astronautics. 2024 (cit. on p. 29).

[53] PICLas Developers. *PICLas User Guide*. PICLas Documentation. 2025 (cit. on pp. 31, 32, 35).

[54] Stefanos Fasoulas et al. «Combining Particle-in-Cell and Direct Simulation Monte Carlo for the Simulation of Reactive Plasma Flows». In: *Physics of Fluids* 31.7 (2019), p. 072006. DOI: 10.1063/1.5097638 (cit. on p. 32).

[55] Claus-Dieter Munz, Monika Auweter-Kurtz, Stefanos Fasoulas, Asim Mirza, Philip Ortwein, Marcel Pfeiffer, and Tilman Stindl. «Coupled Particle-In-Cell and Direct Simulation Monte Carlo Method for Simulating Reactive Plasma Flows». In: *Comptes Rendus Mécanique* 342.10–11 (2014), pp. 662–670. DOI: 10.1016/j.crme.2014.07.005 (cit. on p. 32).

[56] Stefanos Fasoulas et al. «Combining particle-in-cell and direct simulation Monte Carlo for the simulation of reactive plasma flows». In: *Physics of Fluids* 31.7 (2019) (cit. on p. 32).

[57] W. Reschke et al. «Recent developments of DSMC within the reactive plasma flow solver PICLas». In: *AIP Conference Proceedings*. Vol. 1786. 1. AIP Publishing LLC, 2016 (cit. on p. 32).

[58] M. Pfeiffer, A. Mirza, and P. Nizenkov. «Evaluation of particle-based continuum methods for a coupling with the direct simulation Monte Carlo method based on a nozzle expansion». In: *Physics of Fluids* 31.7 (2019) (cit. on p. 32).

[59] PICLas Development Team. *PICLas – Particle-In-Cell and Direct Simulation Monte Carlo*. https://github.com/piclas-framework/piclas. Accessed: March 22, 2026 (cit. on p. 32).

[60] Julian Beyer, Marcel Pfeiffer, and Stefanos Fasoulas. «Radiation Modeling in the PIC-DSMC Code PICLas». In: *Proceedings of the 8th International Workshop on Radiation of High Temperature Gases for Space Missions*. European Space Agency & CNES. 2019 (cit. on p. 32).

[61] Franziska Hild and Marcel Pfeiffer. «Comparison of Stochastic BGK and FP Methods for the Simulation of Non-Equilibrium Multi-Species Molecular Gas Flows». In: *arXiv preprint* (2025). eprint: 2501.18599v2 (cit. on p. 32).

[62] G. A. Bird. *Molecular Gas Dynamics and the Direct Simulation of Gas Flows*. Oxford: Oxford University Press, 1994. ISBN: 9780198561958. DOI: 10.1093/oso/9780198561958.001.0001 (cit. on pp. 32, 35).

[63] Marcel Pfeiffer. «Extending the Particle Ellipsoidal Statistical Bhatnagar–Gross–Krook Method to Diatomic Molecules Including Quantized Vibrational Energies». In: *Physics of Fluids* 30.11 (2018), p. 116103. DOI: 10.1063/1.5054961 (cit. on p. 33).

[64] PICLas Developers. *PICLas User Guide: Workflow*. PICLas Documentation. 2025 (cit. on p. 33).

[65] HOPR Development Team. *HOPR – High Order Preprocessor*. https://gitlab.com/hopr-framework/hopr. Accessed: March 22, 2026 (cit. on p. 33).

[66] Julian Beyer, Marcel Pfeiffer, and Stefanos Fasoulas. «High-Fidelity Rarefied Gas Flow Simulations Using the Hybridizable Discontinuous Galerkin DSMC Method in PICLas». In: *Journal of Computational Physics* 423 (2020), p. 109810. DOI: 10.1016/j.jcp.2020.109810 (cit. on p. 33).

[67] Arturs Jasjukevics. «Title of the Thesis». Master's Thesis. Stuttgart, Germany: University of Stuttgart, 2024 (cit. on p. 34).

Appendix A

Appendix A.1

Table A.1: Superficie proiettata A_{proj} in funzione dell'AoA per diverse configurazioni di pinna

configuration [°]	**70°**	**60°**	**60° (2.5 m)**	**50°**	**40°**	**30°**
0° AoA	65.88	61.71	74.36	56.30	49.90	43.01
5° AoA	68.97	65.19	78.20	60.08	53.98	47.25
10° AoA	71.54	68.18	81.45	63.44	57.64	51.14
15° AoA	73.57	70.65	84.07	66.32	60.86	54.63
17.5° AoA	74.37	71.69	86.06	67.57	62.30	56.23
20° AoA	75.03	72.58	85.00	68.69	63.62	57.71
22.5° AoA	75.55	73.34	87.39	69.68	64.82	59.09
25° AoA	75.92	73.96	86.76	70.53	65.89	60.35
30° AoA	76.24	74.78	88.06	71.85	67.67	62.54
35° AoA	75.97	75.03	87.94	72.61	68.92	64.24
40° AoA	75.13	74.70	87.03	72.82	69.66	65.46
45° AoA	73.72	73.81	85.35	72.48	69.86	66.18

Table A.2: Static margin at 120 km for different configurations and CoG positions

Configuration	CoG = -6.1 m	CoG = -5.8 m	CoG = -5.5 m
30deg	0.56%	0.87%	1.17%
40deg	0.80%	1.07%	1.35%
50deg	0.79%	1.04%	1.27%
60deg	0.83%	0.98%	1.31%
60deg_2.5m	1.02%	1.26%	1.54%
70deg	0.44%	0.64%	0.85%

Table A.3: Static margin at 105 km for different configurations and CoG positions

Configuration	CoG = -6.1 m	CoG = -5.8 m	CoG = -5.5 m
30deg	–	–	–
40deg	–	–	–
50deg	0.79%	1.05%	1.31%
60deg	1.04%	1.27%	1.50%
60deg_2.5m	1.31%	1.62%	1.86%
70deg	1.14%	1.35%	1.56%

Table A.4: Static margin at 95 km for different configurations and CoG positions

Configuration	CoG = -6.1 m	CoG = -5.8 m	CoG = -5.5 m
30deg	–	–	–
40deg	–	–	–
50deg	–	–	–
60deg	1.34%	1.40%	1.55%
60deg_2.5m	1.76%	1.96%	2.32%
70deg	1.32%	1.49%	1.65%

A.1 Effect of the opening angle at Kn = 0.56

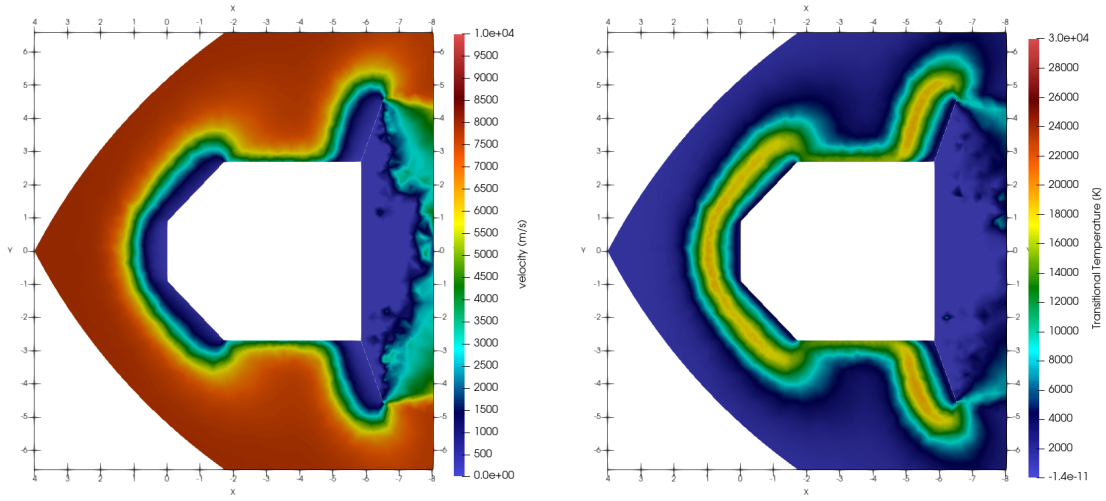

Figure A.1: Flow field characteristics for the configuration with 70° opening angle: velocity field (left) and total temperature (right).

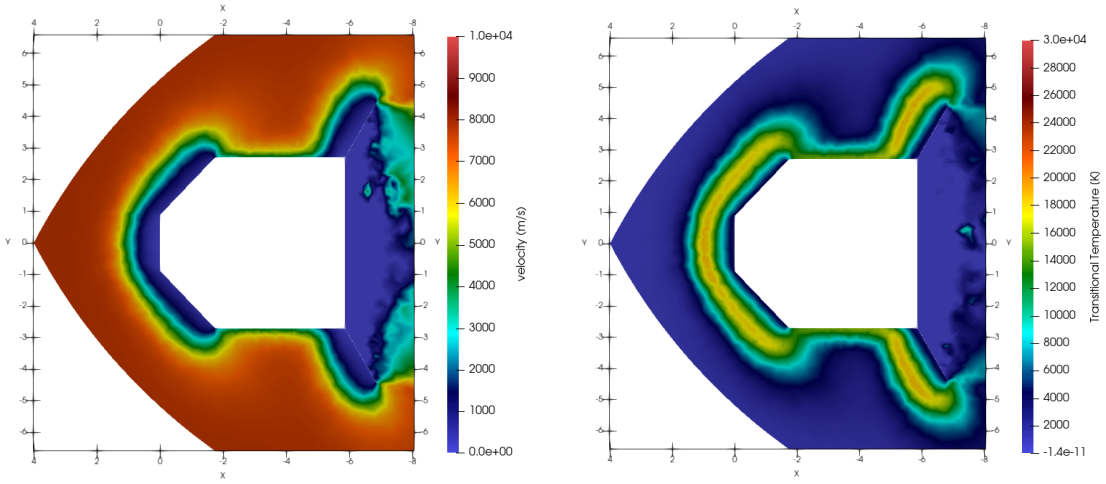

Figure A.2: Flow field characteristics for the configuration with 60° opening angle: velocity field (left) and total temperature (right).

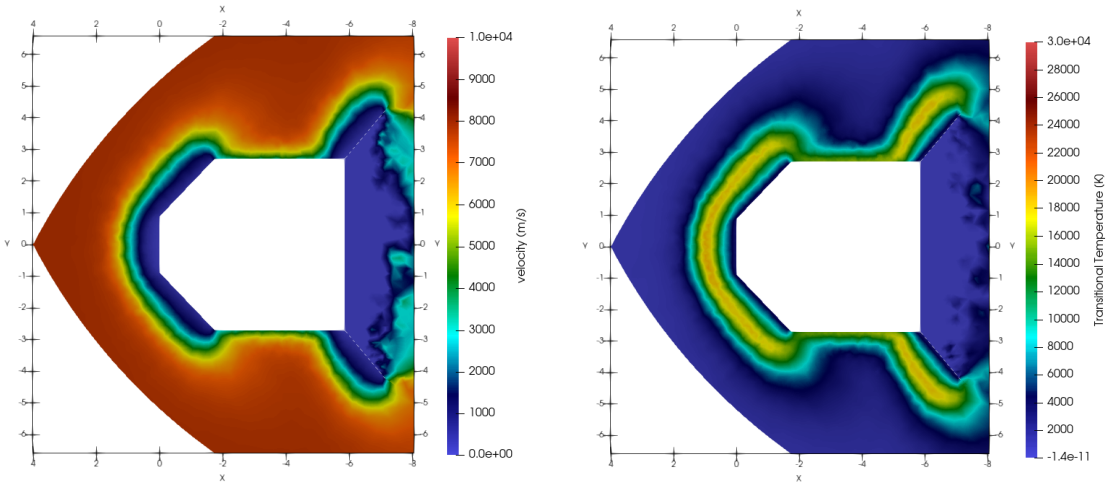

Figure A.3: Flow field characteristics for the configuration with 50° opening angle: velocity field (left) and total temperature (right).

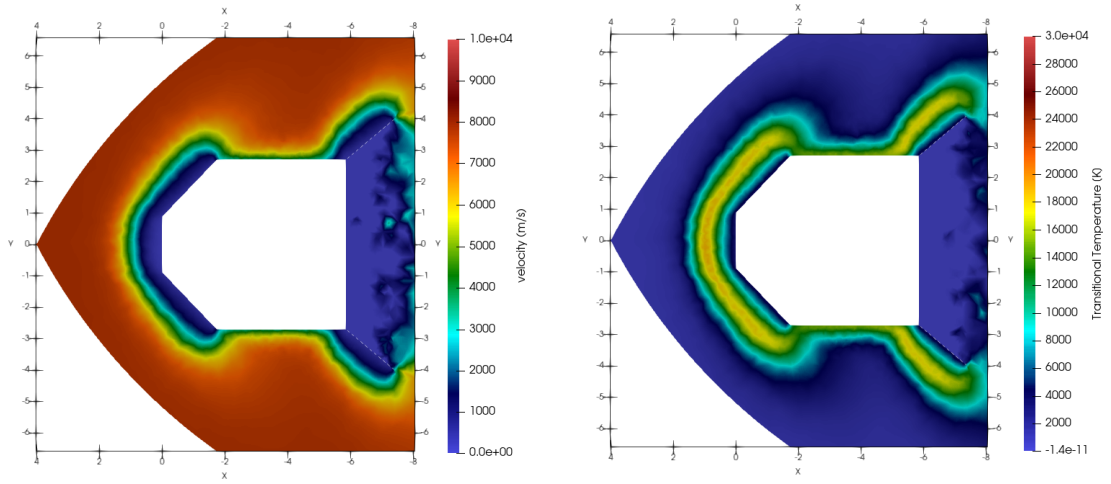

Figure A.4: Flow field characteristics for the configuration with 40° opening angle: velocity field (left) and total temperature (right).

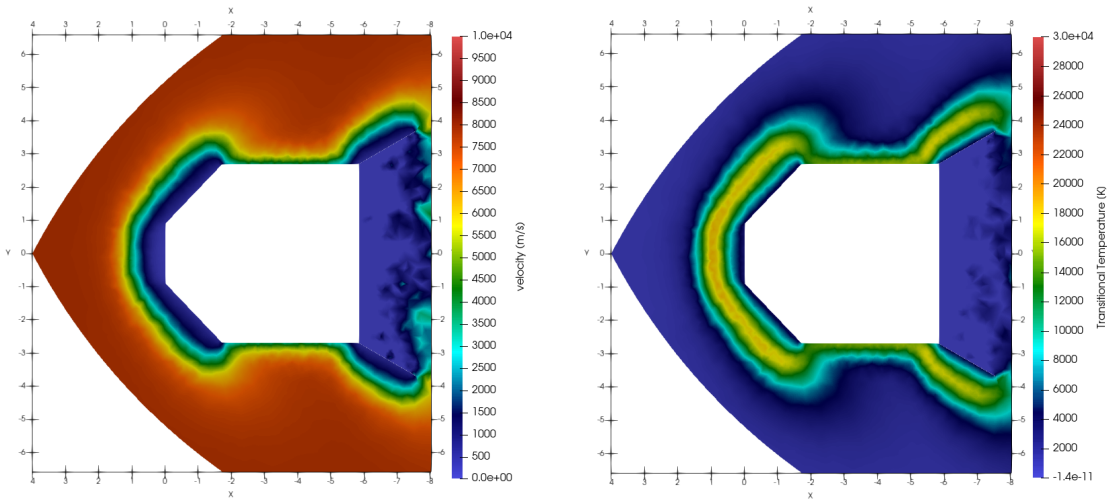

Figure A.5: Flow field characteristics for the configuration with 30° opening angle: velocity field (left) and total temperature (right).

A.2 Effect of the AoA at Kn = 0.56 for the 50° opening angle

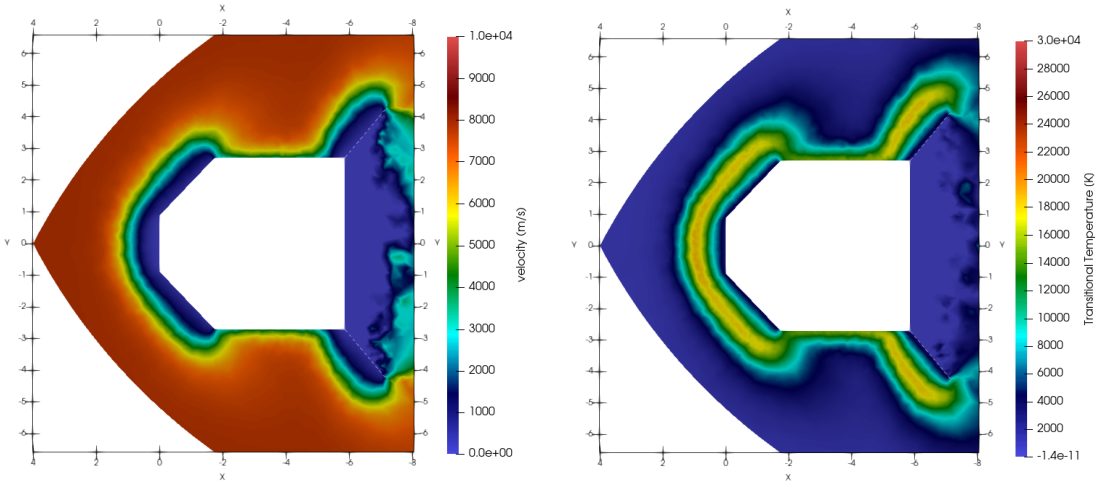

Figure A.6: Flow field for the 50° configuration at AoA 0°: velocity (left) and total temperature (right).

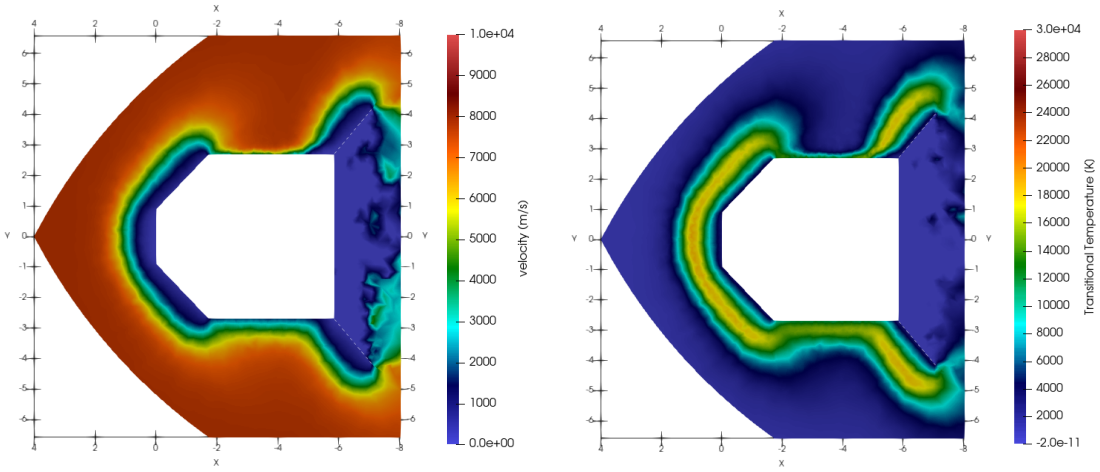

Figure A.7: Flow field for the 50° configuration at AoA 5°: velocity (left) and total temperature (right).

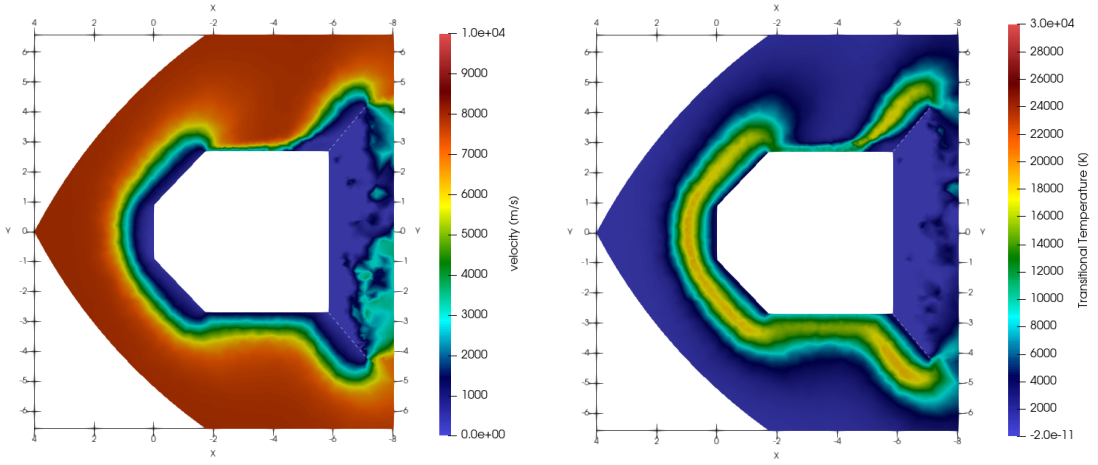

Figure A.8: Flow field for the 50° configuration at AoA 10°: velocity (left) and total temperature (right).

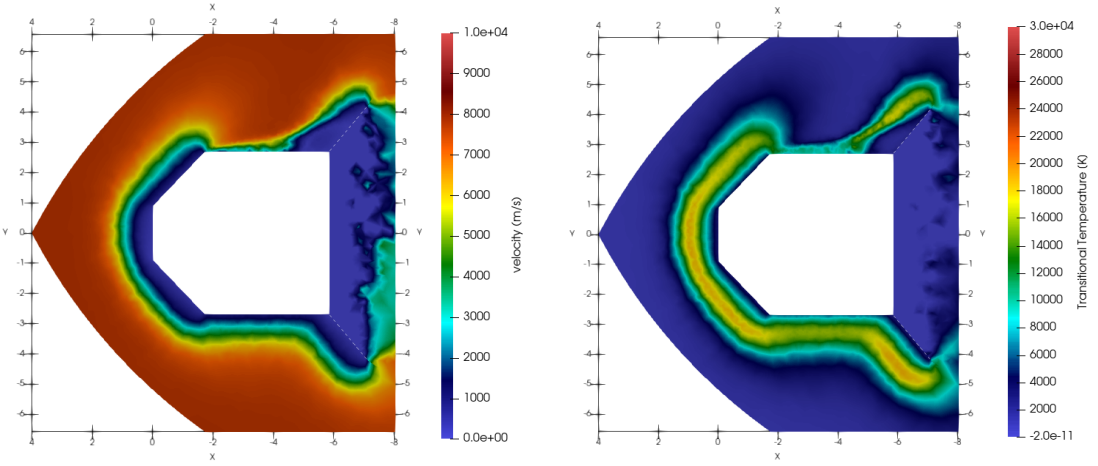

Figure A.9: Flow field for the 50° configuration at AoA 15°: velocity (left) and total temperature (right).

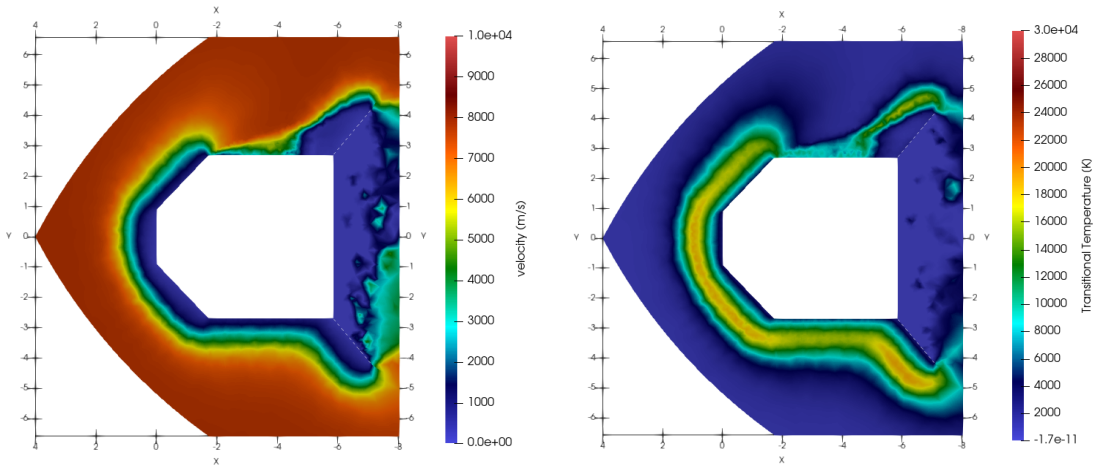

Figure A.10: Flow field for the 50° configuration at AoA 22.5°: velocity (left) and total temperature (right).

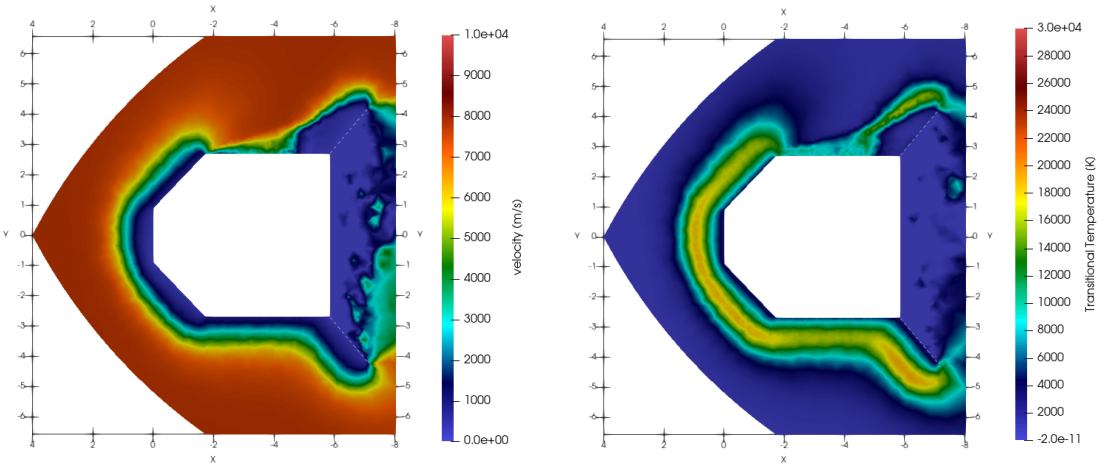

Figure A.11: Flow field for the 50° configuration at AoA 25°: velocity (left) and total temperature (right).

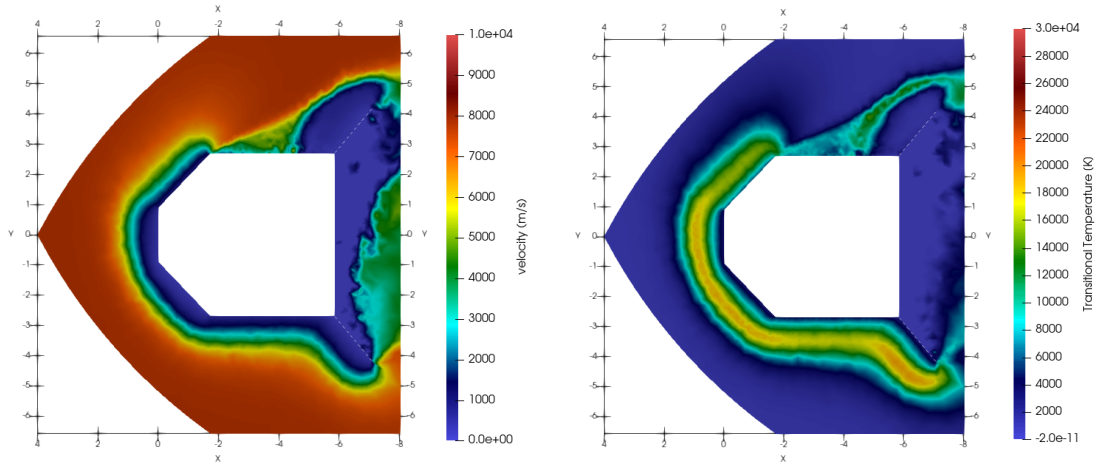

Figure A.12: Flow field for the 50° configuration at AoA 30°: velocity (left) and total temperature (right).

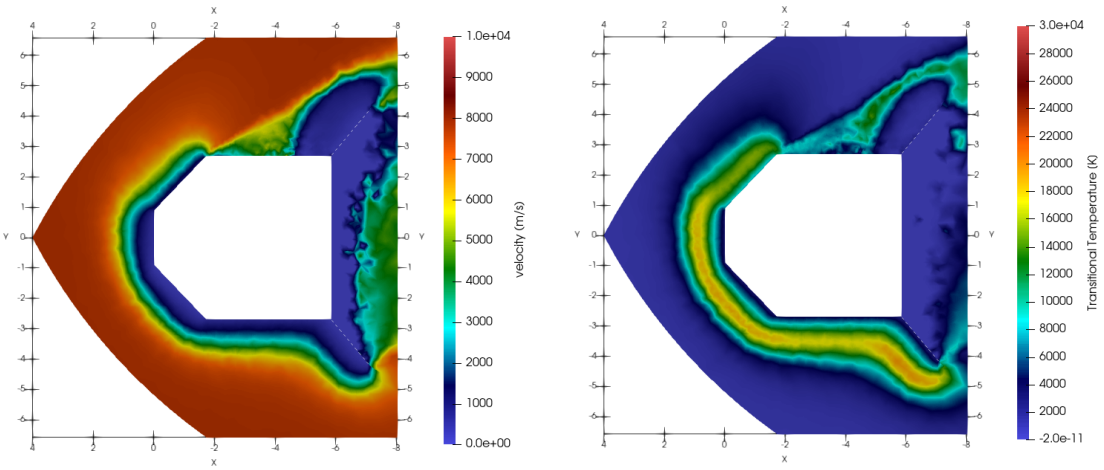

Figure A.13: Flow field for the 50° configuration at AoA 35°: velocity (left) and total temperature (right).

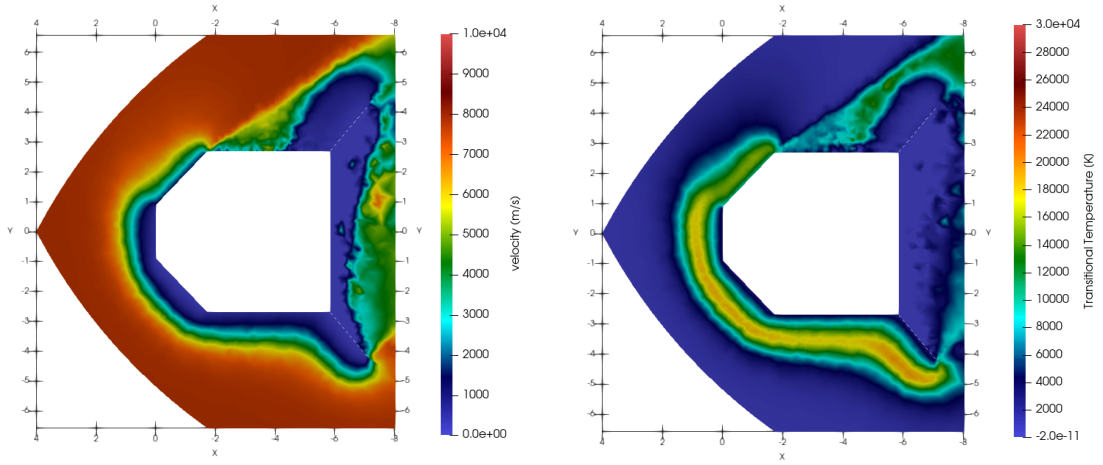

Figure A.14: Flow field for the 50° configuration at AoA 40°: velocity (left) and total temperature (right).

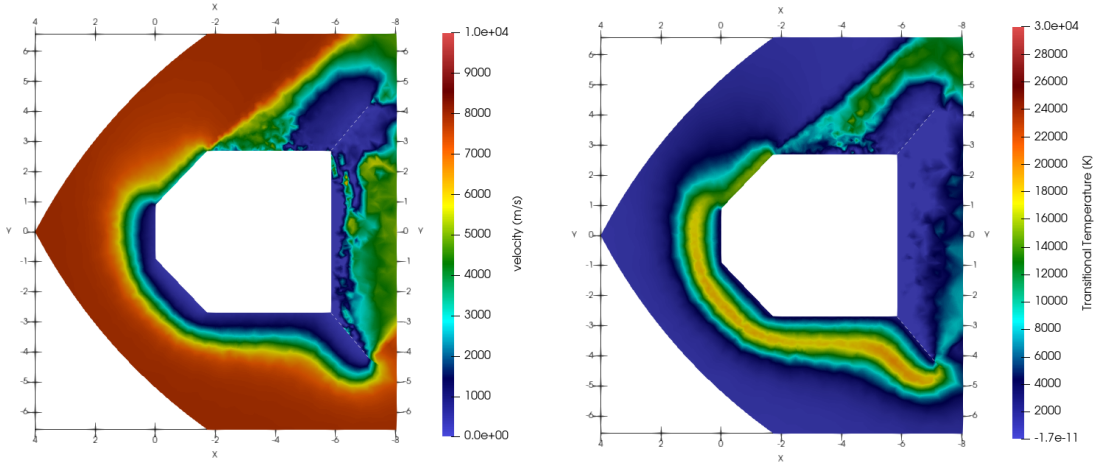

Figure A.15: Flow field for the 50° configuration at AoA 45°: velocity (left) and total temperature (right).

A.3 Effect of the AoA at Kn = 0.06 for the 70° opening angle

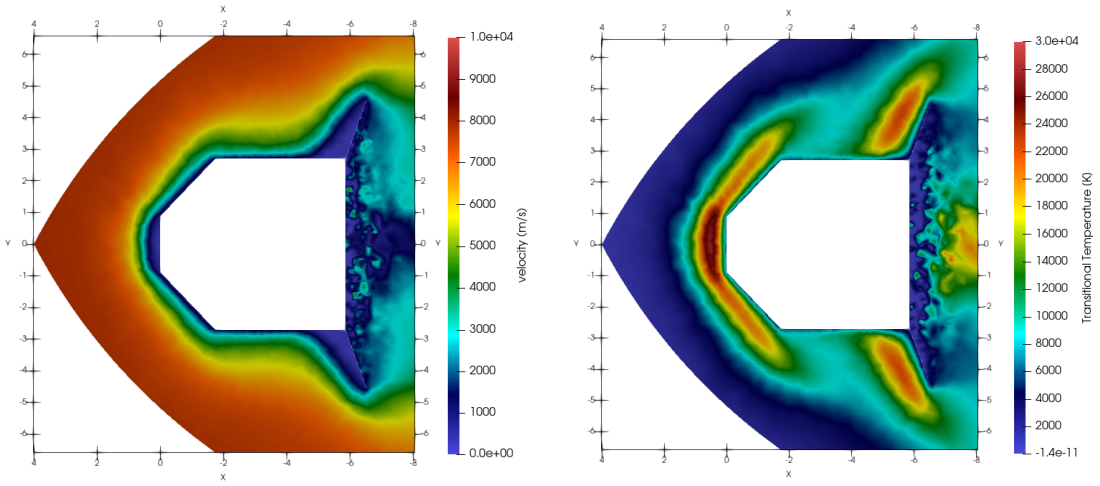

Figure A.16: Flow field for the 70° configuration at 105 km and AoA 0°: velocity (left) and total temperature (right).

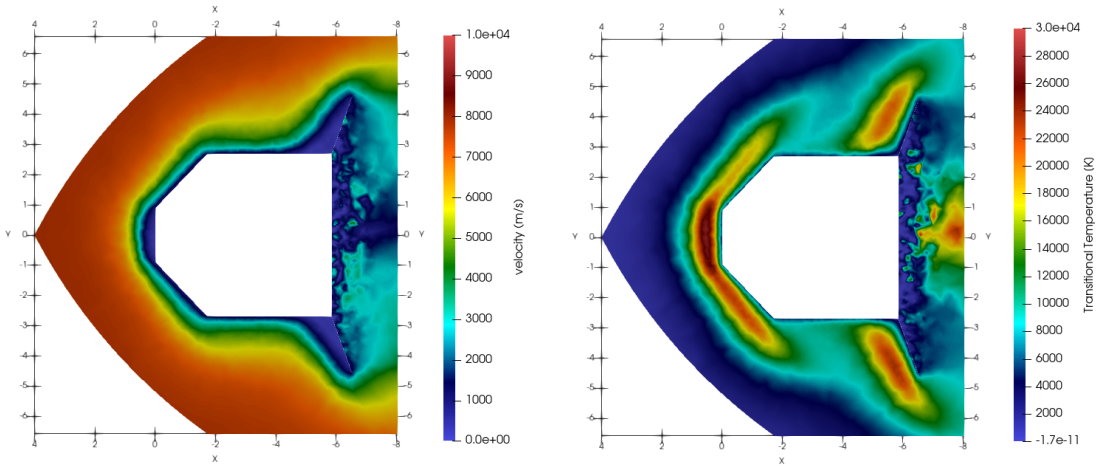

Figure A.17: Flow field for the 70° configuration at AoA 5°: velocity (left) and total temperature (right).

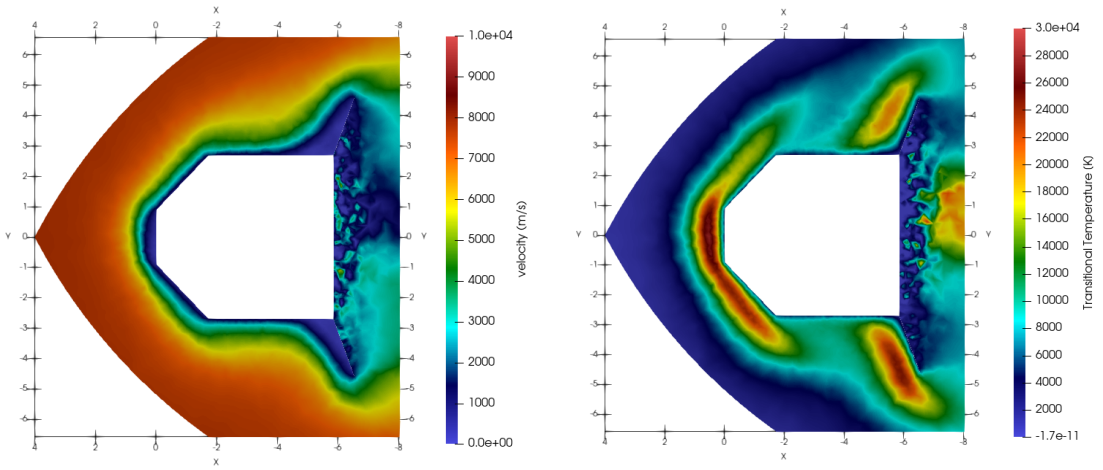

Figure A.18: Flow field for the 70° configuration at AoA 10°: velocity (left) and total temperature (right).

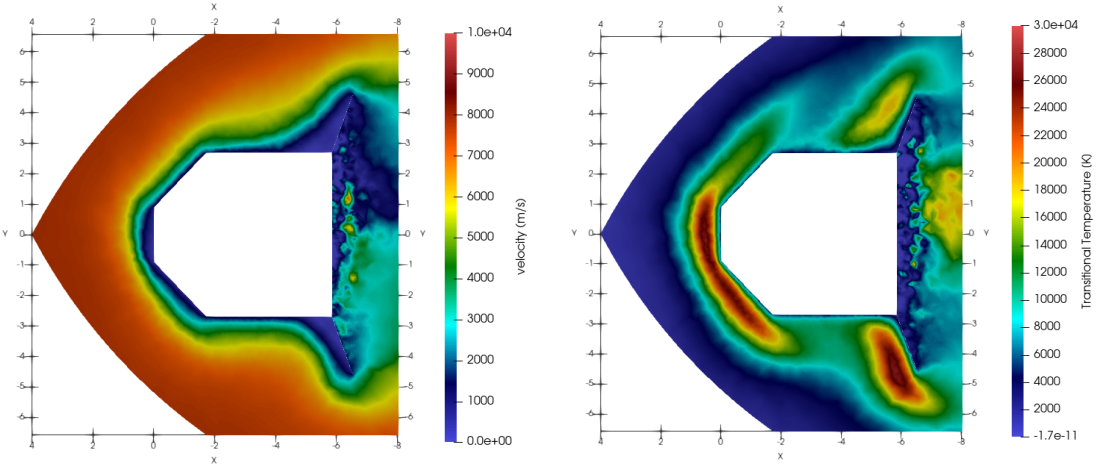

Figure A.19: Flow field for the 70° configuration at AoA 15°: velocity (left) and total temperature (right).

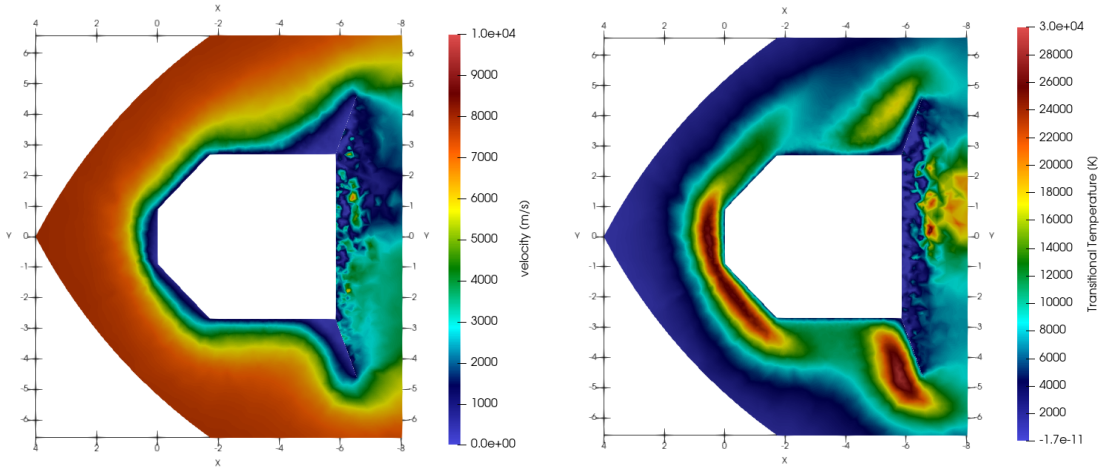

Figure A.20: Flow field for the 70° configuration at AoA 17.5°: velocity (left) and total temperature (right).

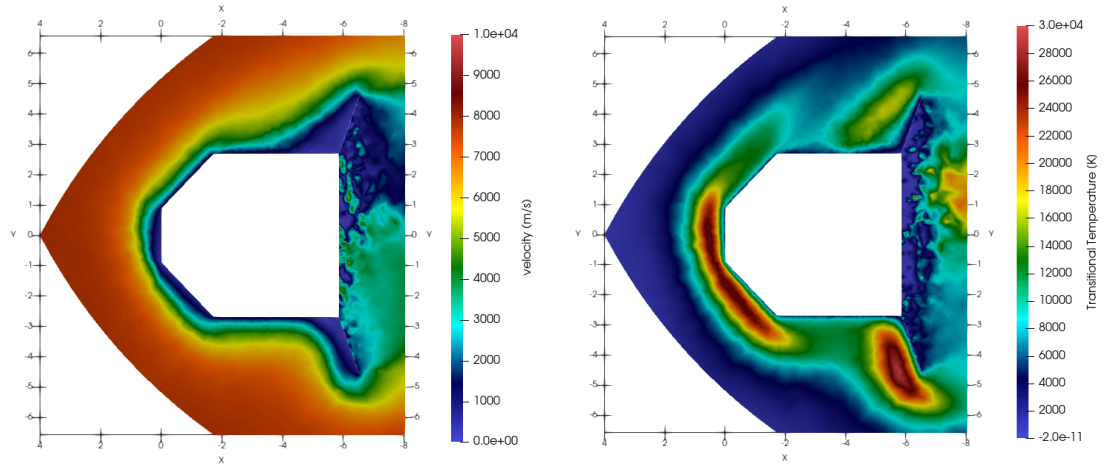

Figure A.21: Flow field for the 70° configuration at AoA 20°: velocity (left) and total temperature (right).

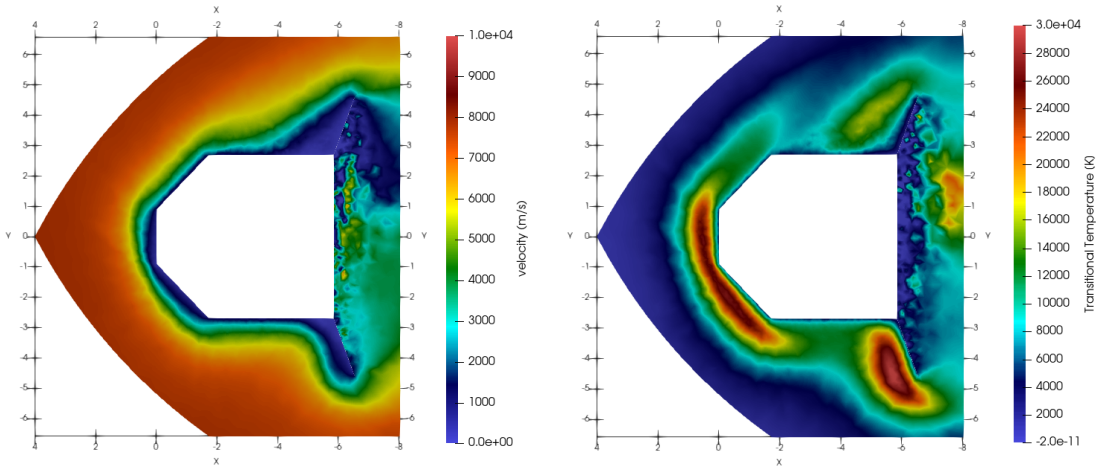

Figure A.22: Flow field for the 70° configuration at AoA 22.5°: velocity (left) and total temperature (right).

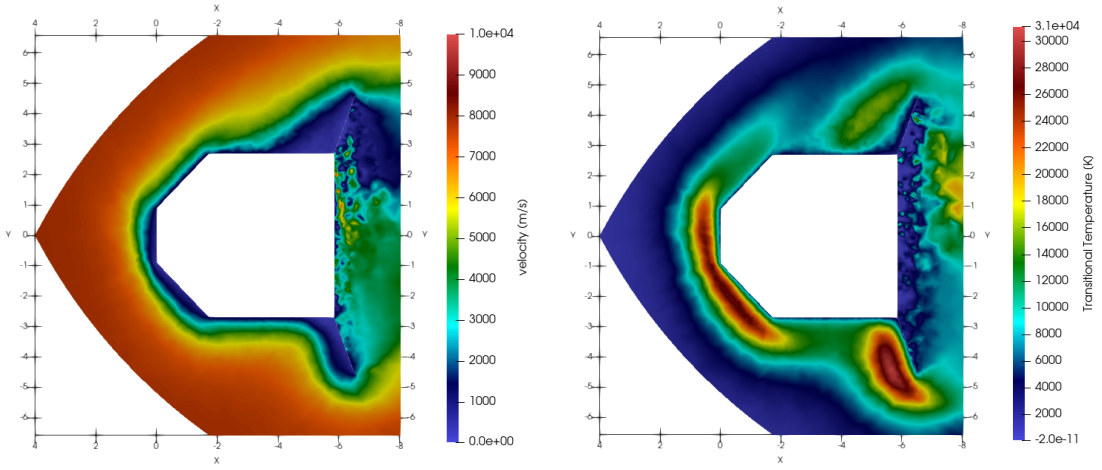

Figure A.23: Flow field for the 70° configuration at AoA 25°: velocity (left) and total temperature (right).

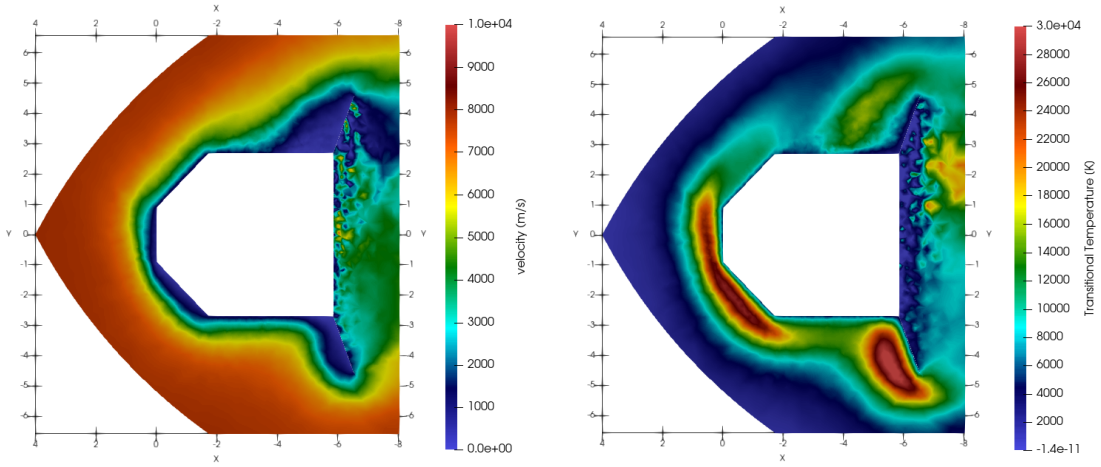

Figure A.24: Flow field for the 70° configuration at AoA 30°: velocity (left) and total temperature (right).

A.4 Effect of CoG

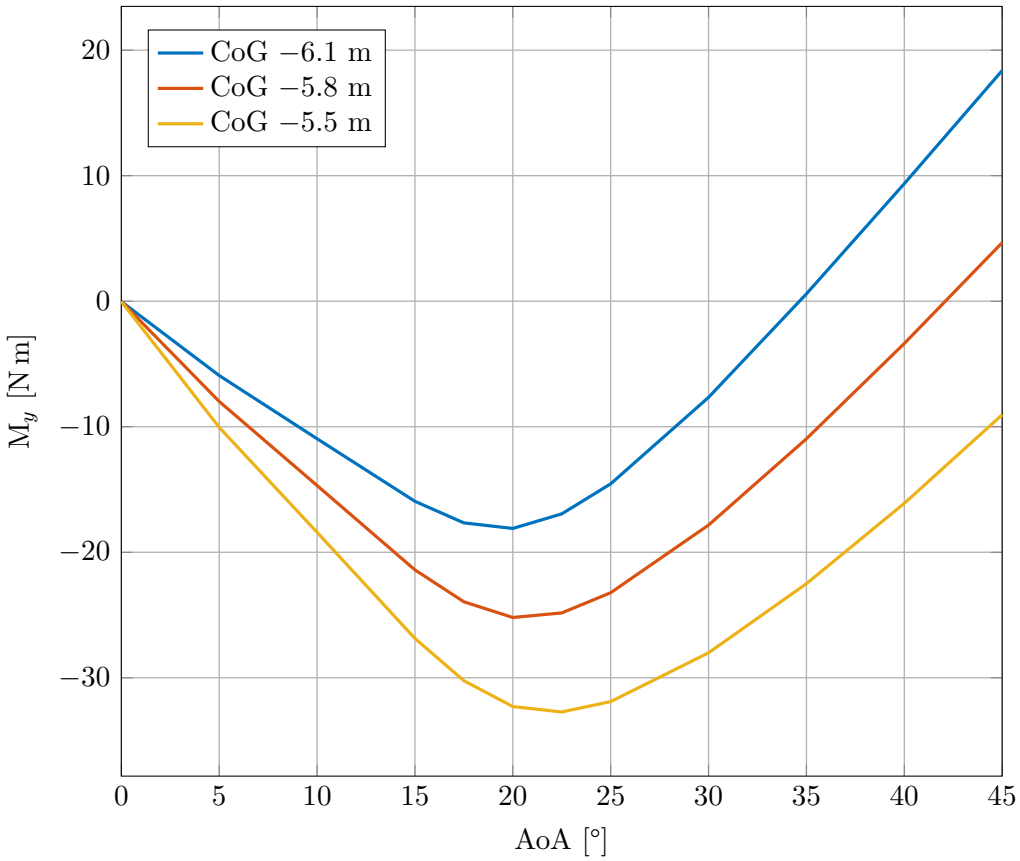

Figure A.25: Pitching moment M_y as a function of angle of attack α for the 60° configuration at an altitude of 120 km, for three longitudinal centre-of-gravity positions.

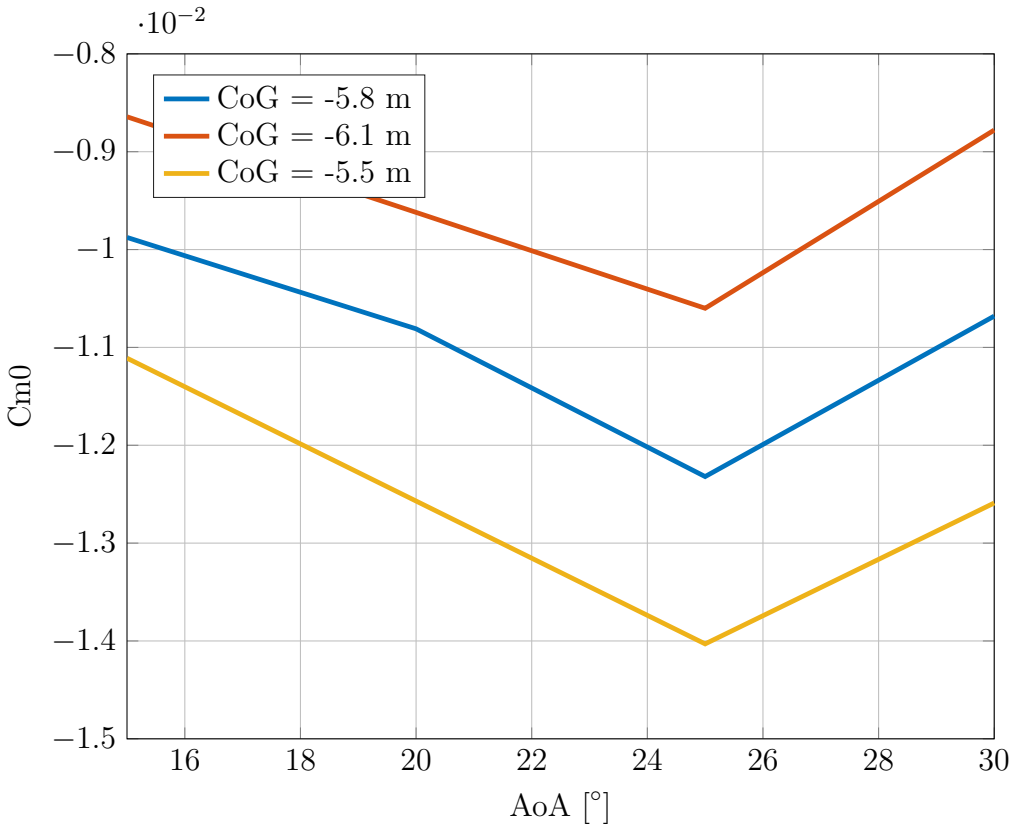

Figure A.26: Trend of the moment coefficient C_{m0} as a function of angle of attack for different center of gravity positions.